University of California
Santa Barbara

Improving Transport in Complex Oxide Heterostructures: High Density 2DELs and High Mobility Stannates

A dissertation submitted in partial satisfaction
of the requirements for the degree

Doctor of Philosophy
in
Materials

by

Santosh Raghavan

Committee in charge:

Professor Susanne Stemmer, Chair
Professor S. James Allen
Professor James S. Speck
Professor Chris Palmstrøm

September 2017

The Dissertation of Santosh Raghavan is approved.

Professor S. James Allen

Professor James S. Speck

Professor Chris Palmstrøm

Professor Susanne Stemmer, Committee Chair

June 2017

Improving Transport in Complex Oxide Heterostructures: High Density 2DELs and High Mobility Stannates

by

Santosh Raghavan

If you understand what you're doing, you're not learning anything

– Chinese fortune cookie

Acknowledgements

It is impossible to imagine that projects like this would be possible without the help of a large group of people. Foremost, I would like to thank my advisor, Susanne Stemmer, for her expert scientific guidance and unyielding support during my PhD. Apart from giving me the opportunity to work in her group, over the years, she has taught me how to be a good scientist and believed in me through the successes and failures of research, for which I'll be always grateful.

I'm very blessed to have the pleasure of working with my colleagues (past and present) and thankful for their support and friendship over the years. I relied heavily on past group members during my initial years in grad school – Pouya Moetakef, Tyler Cain, Adam Kajdos, Jack Zhang, Clayton Jackson, Adam Hauser, Jinwoo Hwang, Varistha Chobpattana, and Ryota Shimizu. In the later stages of my PhD, I depended upon newer members – Timo Schumann, Evgeny Mikheev, Christopher Freeze, Omor Shoron, Honggyu Kim, Patrick Marshall, Brandon Isaac, Manik Goyal, Kaveh Ahadi, David Kealhofer, and Salva Rezaie. I would like to especially thank Dr. Timo Schumann for his expert guidance and support during the stannate projects, and also for voluntarily proof-reading my thesis. None of my projects would have been possible without the untiring support and guidance of John English and Kurt Olsson in the MBE lab. I owe them a lot for teaching me everything about MBE and I'm forever grateful for their support. I'm very thankful to Jack Zhang and Honggyu Kim for TEM imaging of my samples, Gina Adam for help with stepper lithography in the cleanroom, and Kaveh Ahadi for help with ellipsometry measurements. I also have to thank the "MBE Opening Crew" for providing necessary comic relief during and after rigorous MBE openings with post-opening beers and pizza.

I'm thankful for the advice and support of my committee members during my PhD – Profs. Speck, Palmstrom, and Allen. I'm especially grateful to Prof. S. James Allen for our discussions and collaborations on resonant tunneling in 2DELs and stannates.

I would also like to thank my officemates – Victoria Steffes and Brenden McDearmon – for bearing with my shenanigans over the years. I would like to acknowledge the support from MRL staff, especially Joanne McNie who made it easy to deal with administrative issues, and overall, they made it an absolute pleasure to work in the MRL. I also have to thank the staff in the Materials department for their support in maintaining the facilities and making life easy for us to focus on research.

Finally, I would like to thank my family and friends (many of whom are also mentioned above) for their love and untiring support over the years. I can proudly say that I would not be same person today without them.

-Santosh

Curriculum Vitæ

Santosh Raghavan

Education

2017	**Doctor of Philosophy** in Materials, University of California, Santa Barbara, CA 93106, USA.
2011	**Master of Science** in Materials Science, École Polytechnique Fédérale de Lausanne, CH-1015, Switzerland.
2009	**Bachelor of Technology** in Metallurgical and Materials Engineering, Indian Institute of Technology Madras, Chennai 600036, India.

First Author Publications

2016	**S. Raghavan**, J. Y. Zhang, O. Shoron, and S. Stemmer, *Probing the metal-insulator transition in $BaTiO_3$ using electrostatic doping*, Physical Review Letters, 117, 037602, 2016 [DOI]
2016	T. Schumann, **S. Raghavan (equal contributor)**, K. Ahadi, H. Kim and S. Stemmer, *Structure and optical band gaps of (Ba,Sr)SnO_3 films grown by molecular beam epitaxy*, Journal of Vacuum Science & Technology A, 34, 050601, 2016 [DOI]
2016	**S. Raghavan**, T. Schumann, H. Kim, J. Y. Zhang, and S. Stemmer, *High mobility $BaSnO_3$ grown by oxide molecular beam epitaxy*, Applied Physics Letters Materials 4, 016106, 2016 [DOI]
2015	**S. Raghavan**, J. Y. Zhang, and S. Stemmer, *Two-dimensional electron liquid at the (111) $SmTiO_3/SrTiO_3$ interface*, Applied Physics Letters, 106 (13), 132104, 2015 [DOI]
2013	**S. Raghavan**, S. J. Allen, and S. Stemmer, *Subband structure of two-dimensional electron gases in $SrTiO_3$*, Applied Physics Letters, 103 (21), 212103, 2013 [DOI]
2012	**S. Raghavan**, I. Stolichnov, N. Setter, J. S. Heron, M. Tosun, and A. Kis, *Long-term retention in organic ferroelectric-graphene memories*, Applied Physics Letters, 100 (2), 023507, 2012 [DOI]
2011	**S. Raghavan**, A. Carvalho, F. Le Formal, N. Setter, S. Oberg, P.R. Briddon, *Adsorbate-localized states at water-covered (100) $SrTiO_3$ surfaces*, Applied Physics Letters, 98 (1), 012106, 2011 [DOI]

Co-author Publications

2016	*Direct Observation of Sr Vacancies in $SrTiO_3$ by Quantitative Scanning Transmission Electron Microscopy*, H. Kim, J. Y. Zhang,

S. Raghavan, and S. Stemmer. Physical Review X 6, 041063 (2016). [DOI]

2016 *Pseudogaps and Emergence of Coherence in Two-Dimensional Electron Liquids in $SrTiO_3$*, P. B. Marshall, E. Mikheev, **S. Raghavan**, and S. Stemmer. Physical Review Letters 117, 046402 (2016). [DOI]

2016 *Conduction band edge effective mass of La-doped $BaSnO_3$*, S. J. Allen, **S. Raghavan**, T. Schumann, K-M. Law, and S. Stemmer. Applied Physics Letters 108, 252107 (2016). [DOI]

2016 *Large electron concentration modulation using capacitance enhancement in $SrTiO_3/SmTiO_3$ Fin-field effect transistors*, A. Verma, K. Nomoto, W. S. Hwang, **S. Raghavan**, S. Stemmer, and D. Jena. Applied Physics Letters 108, 183509 (2016). [DOI]

2016 *Carrier density independent scattering rate in $SrTiO_3$-based electron liquids*, E. Mikheev, S. Raghavan, J. Y. Zhang, P. B. Marshall, A. P. Kajdos, L. Balents, and S. Stemmer. Scientific Reports **6**, 20865 (2016). [DOI]

2015 *Large electron concentration modulation using capacitance enhancement in $SrTiO_3/SmTiO_3$ Fin-field effect transistors*, A. Verma, K. Nomoto, W. S. Hwang, **S. Raghavan**, S. Stemmer, and D. Jena. Applied Physics Letters 108, 183509 (2016). [DOI]

2015 *Ferroelectric transition in compressively strained $SrTiO_3$ thin films*, A. Verma, **S. Raghavan**, S. Stemmer, and D. Jena. Applied Physics Letters 107, 192908 (2015). [DOI]

2015 *Dielectric response of metal/$SrTiO_3$/two-dimensional electron liquid heterostructures*, E. Mikheev, **S. Raghavan**, and S. Stemmer. Applied Physics Letters 107, 072905 (2015). [DOI]

2015 *Determination of the Mott-Hubbard gap in $GdTiO_3$*, L. Bjaalie, A. Verma, B. Himmetoglu, A. Janotti, **S. Raghavan**, V. Protasenko, E. H. Steenbergen, D. Jena, S. Stemmer, and C. G. Van de Walle. Physical Review B 92, 085111 (2015). [DOI]

2014 *Au-gated $SrTiO_3$ field-effect transistors with large electron concentration and current modulation*, A. Verma, **S. Raghavan**, S. Stemmer, and D. Jena. Applied Physics Letters 105, 113512 (2014). [DOI]

2014 *Correlation between metal-insulator transitions and structural distortions in high-electron-density $SrTiO_3$ quantum wells*, J. Y. Zhang, C. A. Jackson, R. Chen, **S. Raghavan**, P. Moetakef, L. Balents, and S. Stemmer. Physical Review B 89, 075140 (2014). [DOI]

2013 *Magnetism and local structure in low-dimensional Mott insulating $GdTiO_3$*, J. Y. Zhang, C. A. Jackson, **S. Raghavan**, J. Hwang, and S. Stemmer. Physical Review B 88, 121104 (2013). [DOI]

2013 *Growth window and effect of substrate symmetry in hybrid molecular beam epitaxy of a Mott insulating rare earth titanate*, P. Moetakef, J. Y. Zhang, **S. Raghavan**, A. P. Kadjos, and S. Stemmer. Journal of Vacuum Science & Technology A. 31, 041503 (2013). [DOI]

2013 *Symmetry lowering in extreme-electron-density perovskite quantum wells*, J. Y. Zhang, J. Hwang, **S. Raghavan**, and S. Stemmer. Physical Review Letters 110, 256401 (2013). [DOI]

Invited Talks

2016 *Emergent phenomena in complex oxides for advanced electronics*, HRL Laboratories Inc., Malibu, CA.

2016 *Exploring emergent phenomena in complex oxides for advanced electronics*, Northrop Grumman Aerospace Systems, Redondo Beach, CA.

2013 *Understanding 2DEGs in Complex Oxides*, Chemical Sciences Student Seminar 2013, University of California, Santa Barbara, CA.

2011 *Retention properties of graphene – ferroelectric memory devices*, European Meeting on Ferroelectricity 2011, Bordeaux, France.

Conference Presentations

2016 *High mobility $BaSnO_3$ using oxide molecular beam epitaxy*, Materials Research Society Spring Meeting 2016, Phoenix, AZ.

2015 *Metal to insulator transition in $BaTiO_3$ studied via electrostatic doping*, Materials Research Society Spring Meeting 2015, San Francisco, CA.

2015 *High density 2DELs at (111) $SmTiO_3/SrTiO_3$ interfaces*, American Physical Society March Meeting 2015, San Antonio, TX.

2013 *Subband structure of high-density 2DEGs in $SrTiO_3$*, Oxide MURI 2013 Workshop, Stanford, CA.

2013 *Probing high-density 2DEGs in $SrTiO_3$ via resonant tunneling*, Materials Research Society Fall Meeting 2013, Boston, MA.

Selected Honors

2012 UCSB Graduate Division Dean's Fellowship

2011 EPFL Highest Cumulative GPA Award

Abstract

Improving Transport in Complex Oxide Heterostructures: High Density 2DELs and High Mobility Stannates

by

Santosh Raghavan

Perovskite oxides present a wide range of electronic and magnetic properties that set them apart from traditional semiconductors like Si or III–V compounds. However, such properties are yet to be fully harvested in developing new electronic devices with advanced functionalities. The discovery of high density, two-dimensional electron liquids (2DELs) in oxide thin films has shown promise for the advancement of oxide electronics. Yet, many fundamental properties of these electron liquids remain unclear. Another major impediment in developing functional oxide devices is poor electrical conductivities in most perovskite oxide semiconductors.

To that end, this work utilizes oxide molecular beam epitaxy (MBE) to develop new geometries in titanate heterostructures that improve our fundamental understanding of electrical transport in high density oxide 2DELs. This work also pursues growth of a new class of perovskite thin films, alkali-earth stannates, for increased room temperature electrical conductivities in complex oxides.

In this thesis, I discuss the origin and underlying transport mechanisms in 2DELs at (001) and (111) $SrTiO_3/RTiO_3$ (R: rare earth atom) interfaces. By utilizing new titanate devices, we study the sub-band characteristics of 2DELs in $SrTiO_3$. The high density 2DELs are also utilized to answer long-standing fundamental questions about ferroelec-

tricity and its coexistence with metallicity in $BaTiO_3$. Finally, we present approaches in oxide MBE used to develop high quality films of $BaSnO_3$ with improved electrical transport characteristics, featuring room temperature mobilities exceeding 170 $cm^2/V{\cdot}s$ at carrier densities $> 5{\times}10^{19}$ cm^3. Growth of high quality $SrSnO_3$ and $Ba_xSr_{1-x}SnO_3$ films and their structural and optical properties will also be discussed. It will be shown that a combination of the different techniques developed in this thesis has lead to new avenues of research in advancing the goal of functional oxide electronics.

Contents

List of Figures

List of Tables

Chapter 1

Introduction

Perovskite oxides with ABO_3 chemical composition (where A and B are cations and O is oxygen) form a diverse class of materials with a wide range of structural, electronic and magnetic properties. The unique structure of such compounds allows for incorporation of a wide range of elements in the periodic table, with each combination leading to its own unique characteristics. The relative size of the A and B cations determines the resulting structure of the material, in terms of tilting in oxygen octahedra and/or cation displacements [20]. The range of orbital ordering and overlap as a result of the various elements in the structure have lead to discovery of novel condensed matter phenomena, such as ferroelectricity [21], ferromagnetism [22], superconductivity [23], high dielectric response [21, 24], strong electron correlations and Mott insulators [25, 26], among others as shown in Fig. 1.1.

While many unique properties of perovskite oxides have been discovered, their utilization in electronic devices has been limited due to poor electrical conductivity in most oxides at room temperature. Most perovskite oxides are insulators (like $CaTiO_3$ and $LaMnO_3$) and some are metals (like $SrRuO_3$ and $SrVO_3$), but very few are semiconductors, which can be doped in a controlled fashion.

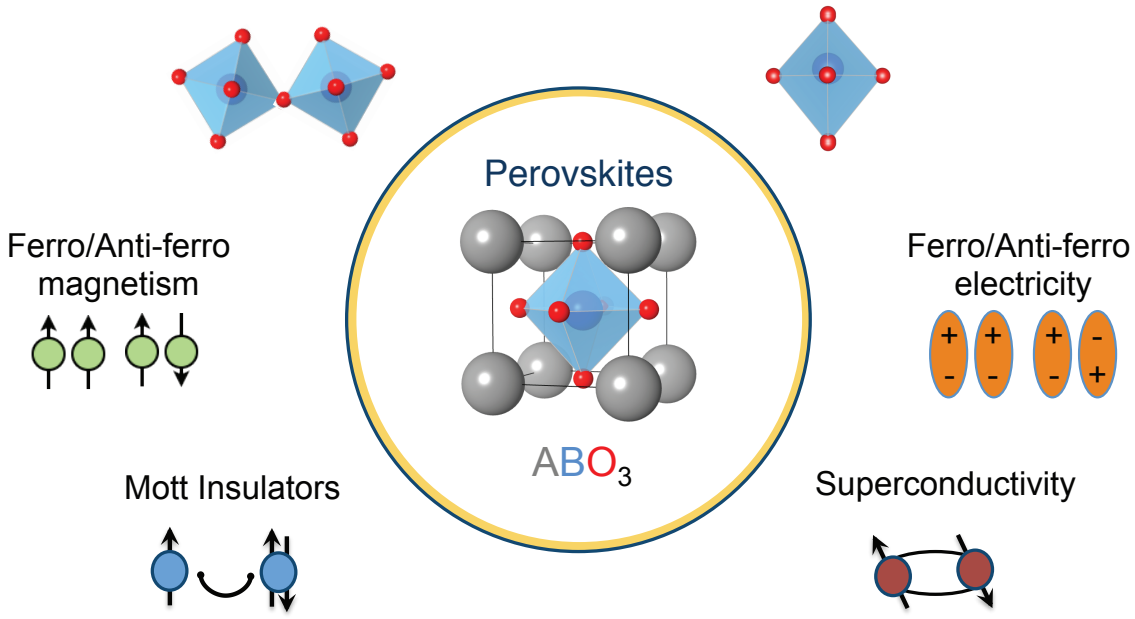

Figure 1.1: Schematic illustrating the structure of a simple cubic perovskite oxide (center), octahedral distortions and cation displacement (top) and some interesting properties that result from variations in the structure (middle, bottom)

.

In this thesis, we will focus on transport properties in two types of semiconducting perovskite oxide thin films: Titanates ($A\mathrm{TiO_3}$) and Stannates ($A\mathrm{SnO_3}$), where A is Sr or Ba. The motivation for fabricating high quality perovskite oxide thin films is two-fold: utilizing advanced fabrication techniques to construct novel geometries of heterostructures that allow for improved understanding of condensed matter properties in these materials, and simultaneously, explore the development of new functional oxide electronic devices that can harvest their unique properties for advanced practical applications.

A brief introduction to the different material systems, fabrication techniques, and transport properties studied in this thesis follows.

1.1 Perovskite Titanates: $ATiO_3$ and $RTiO_3$

1.1.1 $SrTiO_3$

$SrTiO_3$ is a cubic perovskite with a lattice parameter of 3.905 Å[27]. It is a semiconductor with an indirect band gap of 3.2 eV and a direct band gap of 3.8 eV [28]. The material is a well-known and well-studied prototypical oxide semiconductor in which electrons can be introduced by doping on the Sr-site with trivalent rare-earth ions (like La or Gd) [29], doping on the Ti-site with pentavalent ions (like Nb) [30], or introducing oxygen vacancies [31].

Recently, another technique of electrostatic (or remote) doping has been discovered in $SrTiO_3$ where a two-dimensional electron liquid (2DEL) is introduced in the material by interfacing it with a polar oxide, thereby creating a polar discontinuity at the interface. Examples of such material systems are $LaAlO_3/SrTiO_3$ [32] and $R TiO_3/SrTiO_3$ (R: rare-earth atom) [33] that exhibit high sheet carrier densities ($> 10^{14}$ cm^{-2}).

$SrTiO_3$ is considered a quantum ferroelectric material (with a theoretically predicted Curie temperature $T_C = 0$ K) with an enhanced field-tunable dielectric constant. The room temperature relative permittivity is ~ 300 and can be tuned between a large range (25 to 10^4) – using temperature, electric field, epitaxial strain, or chemical substitution – with wide implications on the transport properties in $SrTiO_3$.

In this thesis, we provide additional insight into the polar discontinuity mechanism and related transport in Chapters 2 and 3.

1.1.2 $BaTiO_3$

$BaTiO_3$ is a well-known ferroelectric perovskite with a tetragonal crystal structure at room temperature. Similar to $SrTiO_3$, it has a $\sim$ 3.2 eV indirect band gap [34]. Above the Curie temperature of 120 ^oC, $BaTiO_3$ is a cubic perovskite, but contains random local displacement of Ti cations towards one of the 8 <111> faces of the surrounding oxygen octahedra [35]. This Ti displacement with respect to the oxygen octahedra in the local structure creates a dipole moment – that is reversible – which is the origin of ferroelectricity in the material [36].

In this thesis, we will study the effect of doping on ferroelectricity and transport behavior in $BaTiO_3$ in Chapter 4.

1.1.3 $RTiO_3$

Rare earth (R) titanate perovskites present a wide range of electronic and magnetic properties. $GdTiO_3$ is a ferrimagnetic material, whereas $SmTiO_3$ is an anti-ferromagnet. Both $GdTiO_3$ and $SmTiO_3$ have a orthorhombic crystal structure (Pbnm space group) with tilts in the oxygen octahedra accompanied by A-site cation displacement.

In this thesis, we primarily use $GdTiO_3$ and $SmTiO_3$ for creating a polar discontinuity at the interface with non-polar $SrTiO_3$.

1.2 Perovskite Stannates: $BaSnO_3$ and $SrSnO_3$

Perovskite stannates of interest for high room temperature mobilities are namely $A$$SnO_3$ (A: Sr, Ba). $BaSnO_3$ is a cubic perovskite structure with a lattice constant of

4.116 Å [2] and $SrSnO_3$ has an orthorhombic crystal structure (Pbnm space group, lattice constants a = 5.7079 Å, b = 5.7035 Å, c = 8.0645 Å) with a pseudo-cubic lattice constant of 4.023 Å[1], as shown in Fig. 1.2.

1.2.1 Origin of High Mobility

The electronic bandstructure of perovskite stannate $BaSnO_3$ was first calculated by D.J. Singh et al.[2] for understanding the lack of superconductivity in the material. The authors estimated the band-gap to be > 2 eV and the electronic nature of the conduction band to consist of Sn 5s orbitals. More than a decade later, perovskite stannates were re-analyzed by Mizoguchi et al.[1] for transparent conductor applications and $BaSnO_3$ was highlighted as a promising candidate with highly dispersive conduction band. Density functional theory (DFT) calculations performed by various groups [37, 38, 39] confirm that the lowest conduction band states are made from Sn s-orbitals. The delocalised nature of s-orbitals lead to a much lower effective mass (m^*: 0.20 m_e for $BaSnO_3$, 0.23 m_e for $SrSnO_3$) and high conductivity [37, 38, 39]. This is similar to other transparent conducting oxides like Sn doped In_2O_3 (ITO), ZnO, and SnO_2.

Doping $BaSnO_3$ on the Ba-site with La and on the Sn-site with Sb has been demonstrated by Kim et al.[13] and Luo et al.[40]. Ab-initio calculations predict donor states to be higher up in the conduction band for La, Y, etc. with respect to stannate conduction band minimums. However, only La doping on the Ba-site has so far resulted in single crystals and thin films with high electrical mobility. All experimental attempts to dope stannates with Sn-site substitution have resulted in very low electron mobilities and the reason for this discrepancy is not clear.

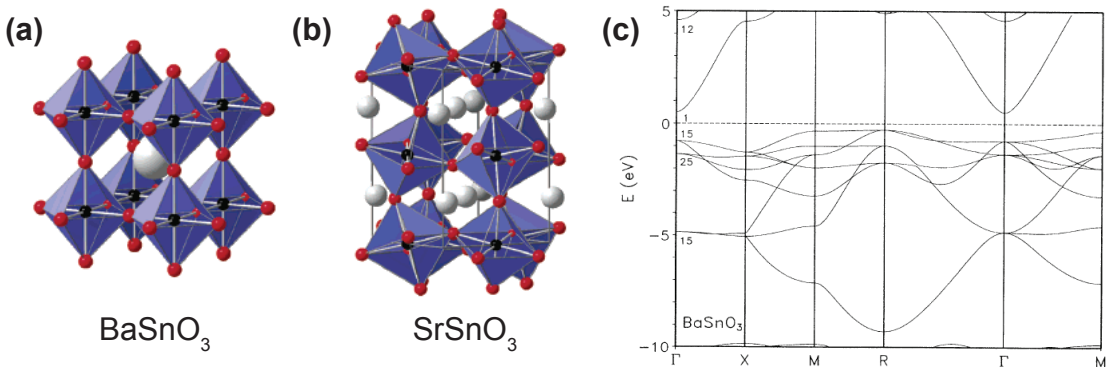

Figure 1.2: (a) Cubic perovskite crystal structure of $BaSnO_3$ and (b) orthorhombic distorted perovskite structure of $SrSnO_3$ (c) Calculated bandstructure for $BaSnO_3$ with a single dispersive conduction band (Reproduced with permission from [1] and [2])

1.2.2 Single Crystals

Theoretical predictions of dispersive conduction bands in $BaSnO_3$ were followed by experimental confirmation when single crystals of La-doped $BaSnO_3$ were shown to posess room temperature mobilities ~320 $cm^2/V{\cdot}s$ at 3D carrier densities between $3{\times}10^{19}$ - $3{\times}10^{20}$ cm^{-3} as shown in Fig.1.3. It is important to note that this remains the highest reported mobility for any semiconductor at such high carrier density. Even the most common wide band-gap semiconductor GaN has room temperature mobilities <100 $cm^2/V{\cdot}s$ at similar carrier densities [41]. The ability to combine high mobilities in devices with high charge densities in this wide-band gap material shows a lot of potential for high performance power electronics.

Initial results on single crystals showed the mobility μ as a function of 3D carrier density n_{3D} to follow a n^{-1} dependance indicating ionised impurity scattering from the dopant atoms as the dominant mobility limiting mechanism [13]. This would suggest that further lowering the carrier density in these single crystals might lead to even higher

room temperature mobilities. But, further work by Kim et al.[3] indicated that room temperature mobilities in their single crystals were more or less independent of n_{3D} in that regime as shown in Fig. 1.3, suggesting a different scattering mechanism (like electron-phonon limited) which might make further mobility enhancement a difficult challenge [3]. The temperature dependance of mobility in the single crystals indicates metallic behavior down to 2 K, indicating degenerate doping and $\mu \approx 600$ cm^2/V·s at low temperatures.

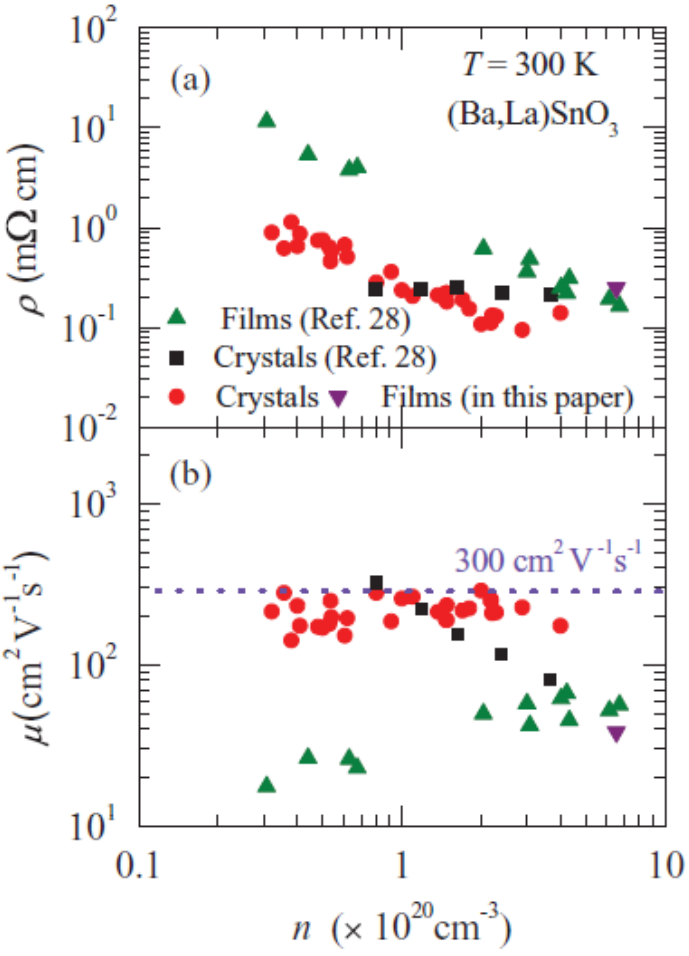

Figure 1.3: Resistivity and mobility values of La-doped $BaSnO_3$ single crystals and pulsed laser deposition grown thin films as a function of carrier density (Reprinted with permission from [3]).

1.2.3 Thin films

Single crystals demonstrated the immense potential of perovskite stannates for oxide electronic applications, including transparent conductors and power electronics. However, realization of electronic devices requires high quality thin films. So far, $BaSnO_3$ thin films have lagged behind in mobility performance. Most reported studies on thin films demonstrate mobilities $\sim$ 80 $cm^2/V{\cdot}s$ for measured 3D carrier densities of $4{\times}10^{20}$ cm^{-3}. The primary reason for the discrepancy between thin films and single crystals is attributed to the lack of lattice matched substrates for the growth of $BaSnO_3$. Fig. 1.4 shows the crystal structure and lattice constants of various commercially available substrates compared to perovskite stannates. No lattice matched substrate exists with lattice parameters in the vicinity of $BaSnO_3$. Most of the reported $BaSnO_3$ thin films have been grown on $SrTiO_3$, $LaAlO_3$ or MgO substrates with lattice mismatches of –5.4%, –7.72% and +2.28% respectively. Such a large lattice mismatch limits the growth of coherently strained films and results in growth of relaxed layers with a high density of dislocations at the film/substrate interface as reported in some studies [42]. Mobility in thin films have been shown to follow a $n^{1/2}$ dependence on the 3D carrier density, indicating scattering from dislocations and grain boundaries, similar to Ge and GaN thin films [43].

Almost all reports focus on highly doped films and single crystals, indicating considerable trapping of carriers in the material and that actual nominal dopant concentration is significantly higher than the measured carrier density. Whether the reason for lack of conduction at lower doping concentrations in the material is intrinsic due to unintentional carrier compensation, or extrinsic due to extended defects and off-stoichiometry, remains to be answered.

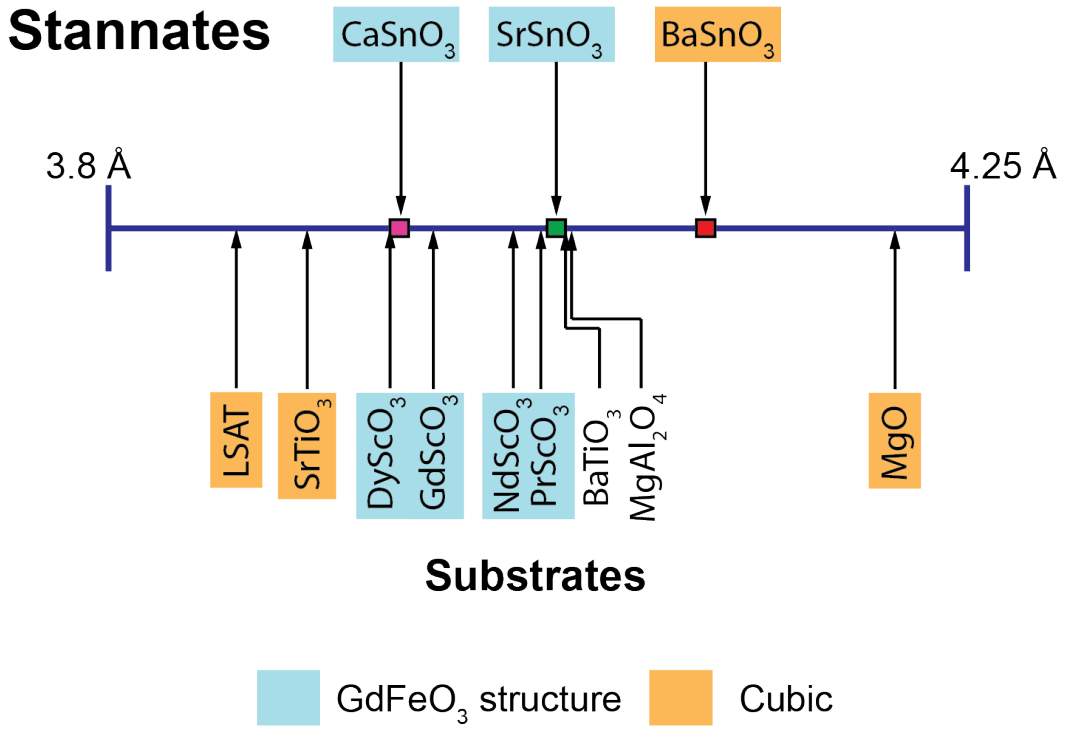

Figure 1.4: Room temperature lattice constants of perovskite stannates of interest and various commercially available substrates for thin film growth (drawn to-scale)

Some reports also show room temperature mobilities as high as 60 $cm^2/V{\cdot}s$ in La-doped $SrSnO_3$ thin films for a measured carrier concentration of $2{\times}10^{18}$ cm^{-3}, although the nominal doping density of the film is as high as $5{\times}10^{20}$ cm^{-3} [44]. Hence, La-doped $SrSnO_3$ also has shown potential for high conductivity, but remains less studied than $BaSnO_3$. It has been predicted that oxygen vacancies have a high energy of formation in perovskite stannates, thus limiting the effect of unintentional doping from oxygen vacancies [45]. The effect of thermal annealing of stannate films in air, oxygen and inert atmospheres suggest a lower oxygen diffusion rate in stannates compared to titanates, cuprates and manganates, thus promising a higher oxygen stability for stannates and potential for high temperature applications [13].

1.3 Oxide Molecular Beam Epitaxy

Electronic and magnetic properties are highly sensitive to defects in the film. In order to obtain high quality thin films and reduce the amount of structural defects, a low energetic deposition technique is necessary. Molecular beam epitaxy (MBE) is such a technique that has consistently produced highest mobility semiconductors [46, 47] and functional oxide films [48]. The technique consists of a ultra high vacuum (UHV) chamber containing a heated substrate and sublimation of high-purity elementary source materials from effusion cells. Very large mean free paths (>1-10 Km) due to the UHV environment allows delivery of molecular beams of elements onto the heated substrate. The substrate can be heated either by direct absorption of radiation from the heater (suitable for small band-gap materials) or indirectly, like indium bonding the substrate on a small band gap wafer like Si. Most oxide substrates (like the ones used in this thesis) are wide band gap materials that are fairly transparent to infrared radiation from the heater. In this work, the substrates are coated with refractory metals (like Ta) on the back to enable non-contact radiative heating of the substrate. Issues related to control of substrate heating in highly oxidizing environments is detailed in Appendix A. The substrate temperature is also measured using an optical pyrometer and compared with a thermocouple near the heater. Morphology and growth kinetics of the film on the substrate are measured *insitu* using reflective high-energy electron diffraction (RHEED).

This work utilizes a Veeco Gen. 930 molecular beam epitaxy system. A schematic of the instrument layout is given in Fig. 1.5. Under certain conditions, the MBE technique allows for an unmatched control of film stoichiometry, by enabling a range of elemental fluxes and temperature parameters within which the film stoichiometry is self-regulating. This regime is referred to as an MBE "growth window" and requires high volatility of

constituent elements and high enough substrate temperatures for an adsorption controlled growth regime. MBE growth windows can be large for III-V semiconductors, like GaAs due to high volatility of As [49]. Growth windows have also been shown for ternary compounds like $PbTiO_3$ (with a volatile Pb constituent), $Bi_4Ti_3O_{12}$ [50, 51], (Rb,Ba)BiO_3 [52], among others. However, control of film stoichiometry for compounds containing constitutents with poor volatility can be challenging since it does not allow for growth windows. Optimization of film stoichiometry is centered around a single point in flux ratio and growth temperature [53] and difficult to achieve with solid source effusion cells. Even minute changes in flux ratios leads to large fluctuations in film stoichiometry, leading to a high concentration of defects. This concept will be discussed further in Chapter 5 in the context of growth of $BaSnO_3$ thin films.

1.3.1 Hybrid MBE Growth of Perovskite Oxides

Low volatility of refractory metals like titanium prevents easy evaporation of the metal from a regular effusion cell for growth of perovskite oxides. Recently, this challenge has been addressed by using a metal-organic precursor called titanium tetra-isopropoxide (TTIP). It has a chemical formula $Ti(OCH(CH_3)_2)$ with each Ti^{+4} cation bonded to 4 oxygen atoms. At elevated temperatures above 260 ^{o}C, TTIP decomposes into TiO_2 and volatile by-products. Above 700 ^{o}C, TTIP decomposes to deposit TiO_2 in an adsorption controlled environment and opening up a growth window for $SrTiO_3$ [54] and rare-earth titanates [55]. In this thesis, Chapter 4 illustrates extension of this technique to $BaTiO_3$.

Spurred by the success of high quality $SrTiO_3$ growth using TTIP, this hybrid technique has been later extended to $SrZrO_3$ [56] and $SrVO_3$ [57]. Some preliminary results on extending the hybrid technique to perovskite stannates will be discussed in Chapter 5.

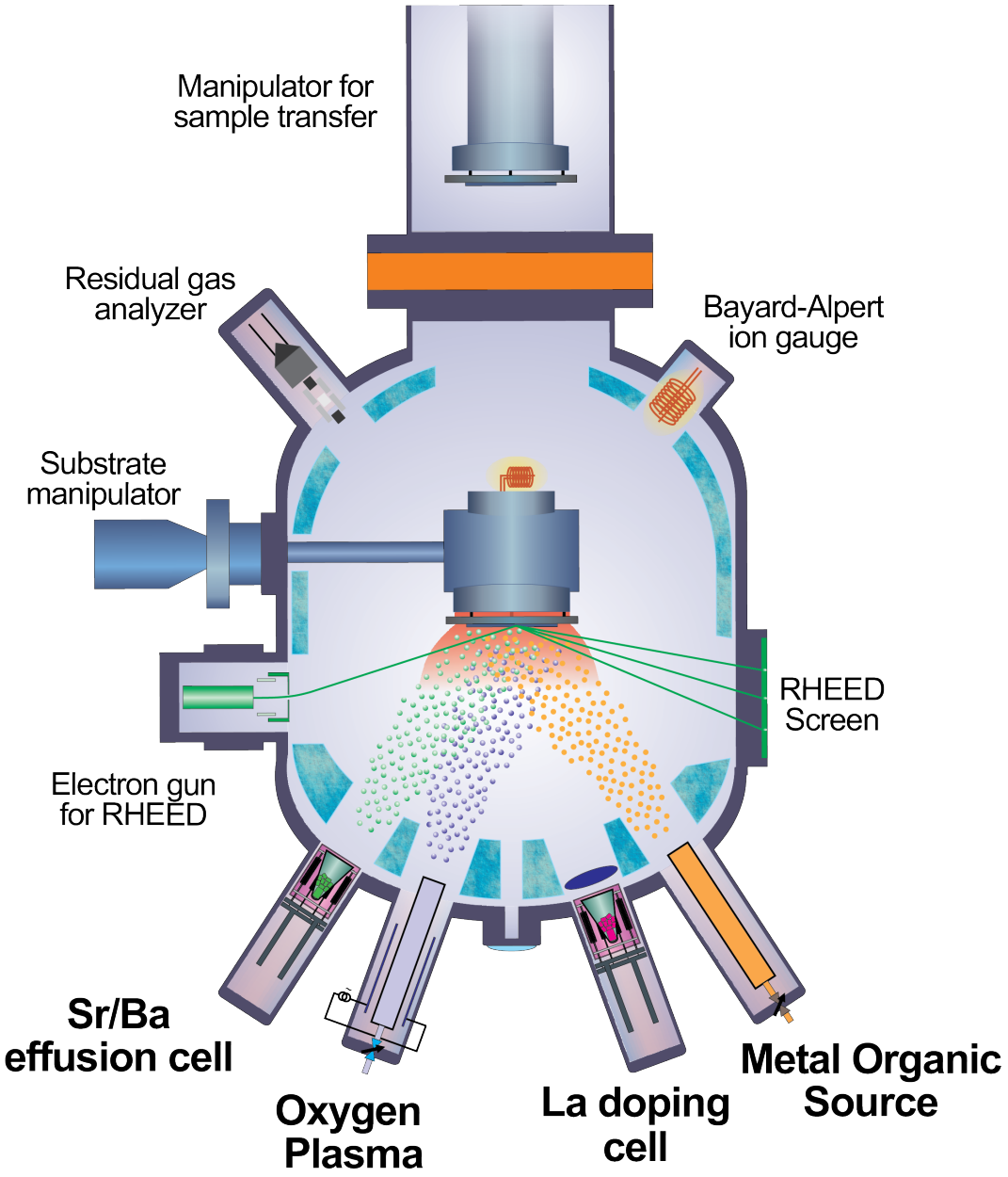

Figure 1.5: Schematic showing film growth using the hybrid molecular beam epitaxy technique for perovskite titanates

1.4 Mobility Limiting Mechanisms in Oxides

Mobility in a semiconductor is a measure of speed at which carriers can be transported in the material under the application of an electric field. There are two types of

electrical mobility that are usually discussed : Drift mobility μ_d and Hall mobility μ_H.

In vacuum, electrons can be accelerated to very high velocities without scattering. In a solid, electrons suffer from scattering off the lattice, defects, impurities, phonons, etc., and the velocities are finite, called the drift velocity. The drift mobility is defined as how quickly an electron moves under an electric field E with a drift velocity ν_d and can be measured in a field effect transistor. It is described easily as:

$$\mu_d = \frac{\nu_d}{E} \tag{1.1}$$

Ohm's law is used to calculate μ_d by measuring current density J in the solid as a function of electric field E, that yields the conductivity σ and is related to charge carrier density n and carrier charge q as:

$$J = \sigma E = nq\nu_d \tag{1.2}$$

If the average time between consecutive scattering events is τ, the mobility can be expressed as function of τ, q, and a carrier effective mass m^*:

$$\mu_d = \frac{q\tau}{m^*} \tag{1.3}$$

Hall mobility μ_H is measured using the Hall effect and is usually slightly different from the drift mobility since carriers with different energies experience different Lorentz force. The Hall mobility is related to the drift mobility through the Hall factor r_H, which is usually on order of 1–2 [58]:

$$\mu_H = r_H \mu_d \tag{1.4}$$

All the mobilities discussed in the results shown in this thesis are Hall mobilities unless otherwise specified. Hall mobilities are measured either using a Hall bar geometry [59] or Van der Pauw geometry [60]. A brief introduction to various mobility limiting scattering mechanisms relevant to perovskite oxides is now discussed.

1.4.1 Electron–Phonon Interactions

One of the primary scattering mechanisms in perovskite structures is due to vibrations of the ions in the lattice (i.e. phonons) interacting with the charge carriers. Further, as the charge carrier moves, its Coulomb force interacts with anions and cations in the lattice, displacing them with respect to one another. There are 15 phonon modes in a cubic perovskite, which can be classified into three types: 3 acoustic modes, 4 longitudinal optical (LO) modes and 4 doubly degenerate transverse optical (TO) modes [61]. The ionic nature of bonds in the perovskite lattice forces strong long-range Coulomb interactions, causing splitting into separate LO and TO phonon modes. This concept is of important consequence and will be discussed in further detail in Chapter 4 of this thesis. Interactions between charge carriers and various phonon modes can be treated using Boltzmann transport theory [29, 62]. Formalisms for various electron–phonon interactions discussed in this thesis are mentioned below.

Acoustic Phonon Scattering

Acoustic phonon limited electron mobility is given by [63]:

$$\mu_{ac} = \frac{2e\hbar\rho\nu_s^2}{3\pi n_{3\mathrm{D}} m_e^* a_C^2} \ln(1 + e^{E_F/k_B T}) \tag{1.5}$$

where ρ is mass density, ν_s is sound velocity in medium, a_C is acoustic deformation potential, E_F is Fermi energy, e is electron charge, $n_{3\mathrm{D}}$ is electron density, m_e^* is effective

mass.

Longitudinal Optical Phonon Scattering

The polaron model for polar crystals [64] is used to describe LO phonon limited mobility for $SrTiO_3$ [29]:

$$\mu_{LO} = \frac{1}{2K_{ep}\omega}\frac{e}{m_P}\left(\frac{m_e^*}{m_P}\right)^2 f(K_{ep})\left(exp\left(\frac{\hbar\omega}{k_BT}\right)-1\right) \tag{1.6}$$

with the polaron quasiparticle mass

$$m_P = m_e^*\left(1+\frac{K_{ep}}{6}\right) \tag{1.7}$$

and the dimensionless electron-phonon coupling constant

$$K_{ep} = \frac{e^2}{\hbar}\sqrt{\frac{m_e^*}{2\hbar\omega}}\left(\frac{1}{\epsilon_\infty}-\frac{1}{\epsilon}\right) \tag{1.8}$$

$f(K_{ep})$ is a dimensionless function, weakly dependent on K_{ep}, and is ≈ 1. ω is the phonon frequency, ϵ_∞ is the high frequency dielectric constant and ϵ is the static dielectric constant. The above expression assumes a scattering rate τ_{LO} independent of the wave-vector k and is a good assumption for $SrTiO_3$ with a weak dispersion of the conduction band and a large density of states near Γ point. For materials like $BaSnO_3$, with much stronger dispersion and high filling of the conduction band away from Γ point due to large carrier densities, τ_{LO} is dependent on k. A complete discussion of such a LO phonon scattering formalism is given in [58].

Transverse Optical Phonon Scattering

Scattering from TO phonon modes can be modeled as [63]:

$$\mu_{TO} = \frac{\sqrt{2}\pi\hbar^3\rho\nu_s^2(e^{\hbar\omega_{TO}/k_BT}-1)}{(m_e^*)^{5/2}\omega_{TO}d_0^2\sqrt{E+\hbar\omega_{TO}}} \tag{1.9}$$

where ω_{TO} is frequency of TO phonon mode, d_0 is optical phonon deformation potential, E is electron energy. While some reports have suggested importance of TO phonon scattering in $SrTiO_3$ at intermediate temperatures (20–80 K) [65], more evidence points to a different mechanism at play in $SrTiO_3$ in this regime, leading to a T^2 dependence [66].

1.4.2 Electron–Electron Scattering

Resistivity measured in the form of $\rho = AT^2$ has been usually attributed to electron–electron scattering in condensed matter systems. The origin of electron–electron scattering is from Fermi liquid theory which has been historically used to describe resistivity behavior in metals at low temperatures where the thermal energy fluctuations are much smaller than the Fermi energy ($k_BT << E_F$) [67, 68, 69]. Using Pauli's exclusion principle and Fermi Dirac statistics, a quasiparticle approximation of electron–electron scattering leads to:

$$\mu_{ee}^{-1} \propto T^2 \tag{1.10}$$

Recent work has shown similar behavior for transport in $SrTiO_3$ [70, 71], rare-earth nickelates [72], and cuprates [73] at elevated temperatures. This has lead to debate about the merits and applicability of Fermi liquid theory and electron–electron scattering to observations of T^2 dependence in resistivity at elevated temperatures, especially for $SrTiO_3$ [74, 75]. It has been pointed out that assumptions needed to satisfy the T^2

dependence due to electron–electron scattering (by Coulomb and/or acoustic-phonon mediated mechanism) holds well for metals (like Al, Cu or Na) at low temperatures, but not necessarily for semiconductors like $SrTiO_3$ at elevated temperatures. Although, even the best case scenario with no inherent assumptions shows that $SrTiO_3$ comes closer to satisfying T^2 behavior at high carrier densities [75], which is the case for high density 2DELs discussed in this thesis. Further theoretical work is necessary to explain the T^2 dependence in $SrTiO_3$ and is outside the scope of this thesis.

1.4.3 Disorder Induced Scattering

Electrons in the crystal can scatter from extended defects like misfit and threading dislocations [43], neutral and ionized impurities (like dopant atoms) [29, 76], interface roughness for tightly confined 2DELs, or disorder from off-stoichiometry in the lattice [62]. These defects have a temperature dependence for non-degenerate semiconductors. For degenerate semiconductors, they generally do not have a strong temperature dependence and are a constant scattering source at all temperatures. However, other scattering mechanisms usually are stronger at high temperatures and scattering from disorder is dominant only at low temperatures. They can be considered to produce a constant scattering rate τ_0 resulting in a constant value for disorder induced mobility μ_0 that will used for fitting mobility discussed in this thesis.

1.5 Outline

This thesis is organized into five main chapters. The first three chapters (2, 3, and 4) cover research on new geometries in perovskite titanate heterostructures, and next two chapters (5 and 6) detail research on growth and characterization of high mobility perovskite stannate thin films.

In Chapter 2, we introduce the concept of polar discontinuity in polar/non-polar perovskite titanate heterostructures. The origin and critical thickness for 2DEL formation at (001) interfaces is studied. The polar discontinuity concept is then extended to (111) interfaces. After a brief overview of growth of perovskite titanates along (111) orientation, the structural and transport properties of (111) 2DELs are studied, and the difference in electron transport between (001) and (111) interfaces is analyzed using the $SrTiO_3$ Fermi surface.

Chapter 3 details an in-depth study of the sub-band structure of 2DEL at (001) interfaces. The concept of resonant tunneling between two adjacent 2DELs is introduced for our perovskite titanate heterostructures. After a brief overview of resonant tunnel diode fabrication process, the electrical data from tunnel diodes is analyzed. The results are compared with theoretical predictions for sub-bands in $SrTiO_3$.

In Chapter 4, polar discontinuity is extended to $BaTiO_3$ to introduce a high charge density of electrons into ferroelectric $BaTiO_3$ without any disorder from dopants. The electrostatic doping of electrons is used to study the transport properties in $BaTiO_3$ as function of layer thickness. Electrical transport and comparative local structure results are used to answer long-standing fundamental questions about co-existence of ferroelectricity and metallicity in $BaTiO_3$.

The topic of perovskite stannates is introduced in Chapter 5, detailing various approaches in oxide MBE to obtain growth of stannate thin films. Structural quality of films grown using different approaches are highlighted and effect of growth conditions on film stoichiometry is analyzed.

Chapter 6 discusses electrical transport properties of perovskite stannate thin films. The effect of substrates, temperature, film stoichiometry on film mobility are analyzed. A brief description of the effective mass of carriers in $BaSnO_3$ is also included. Ellipsometry results on stannate thin films to measure the optical band gaps and its consequences on transport properties is explained.

The final Chapter 7 summarizes the results shown in this thesis, and future research directions that arise from the results are considered.

1.6 Permissions and Attributions

1. The contents of Chapter 2 have previously appeared in Applied Physics Letters, **106**, 132104 (2015) [5]. It is licensed under Creative Commons Attribution (CC BY 4.0) by the AIP Publishing LLC, and reproduced here.

   - `http://aip.scitation.org/doi/abs/10.1063/1.4916963`

2. The contents of Chapter 3 have previously appeared in Applied Physics Letters, **103**, 212103 (2013) [6]. It is licensed under Creative Commons Attribution (CC BY 4.0) by the AIP Publishing LLC, and reproduced here.

   - `http://aip.scitation.org/doi/abs/10.1063/1.4831976`

3. The contents of Chapter 4 have previously appeared in Physical Review Letters, **117**, 037602 (2016) [8]. It is Copyrighted by the American Physical Society and reproduced here with permission.

   - `https://journals.aps.org/prl/abstract/10.1103/PhysRevLett.117.037602`

4. The contents of Chapters 5 and 6 have previously appeared in APL Materials, **4**, 016106 (2016) [11] and Journal of Vacuum Science & Technology A, **34**, 050601 (2016) [12]. It is licensed under Creative Commons Attribution (CC BY 4.0) by the AIP Publishing LLC, and reproduced here.

   - `http://aip.scitation.org/doi/abs/10.1063/1.4939657`
   - `http://avs.scitation.org/doi/abs/10.1116/1.4959004`

   Several figures have been adapted with permission from [1, 3, 4]. They are Copyrighted by the American Physical Society, American Chemical Society, American Association for the Advancement of Science.

Chapter 2

Two Dimensional Electron Liquids at $SmTiO_3/SrTiO_3$ Interfaces

2.1 Polar Discontinuity along (001) Heterostructures

The formation of a two dimensional electron gas in a semiconductor is the key to success of modern field-effect transistor technology [59]. Consequently, the discovery of two dimensional electron liquids (2DELs) in perovskite oxides at the (001) interface of $LaAlO_3/SrTiO_3$ [77] has raised hopes for functional oxide electronics and opened up avenues for similar research in other oxide-based material systems. The (001) interface of $R\mathrm{TiO}_3/\mathrm{SrTiO}_3$, where R is a trivalent rare-earth ion like Gd or Sm, is one such system which has been studied extensively due to interesting phenomena like strong electron correlations [33, 66, 78, 79].

The (001) oriented interface of $SrTiO_3$ consists of alternating layers of charge neutral $Sr^{+2}O^{-2}$ and $Ti^{+4}O_2^{-2}$ planes. In contrast, $R\mathrm{TiO}_3$ has alternating charged $R^{+3}O^{-2}$ (+1) and $Ti^{+3}O_2^{-2}$ (–1) layers. When $SrTiO_3$ and $R\mathrm{TiO}_3$ are brought together along the (001) interface, as shown in Fig. 2.1, there is a discontinuity in the polarization at the polar/non-polar interface. Such a discontinuity would lead to a divergent electronic

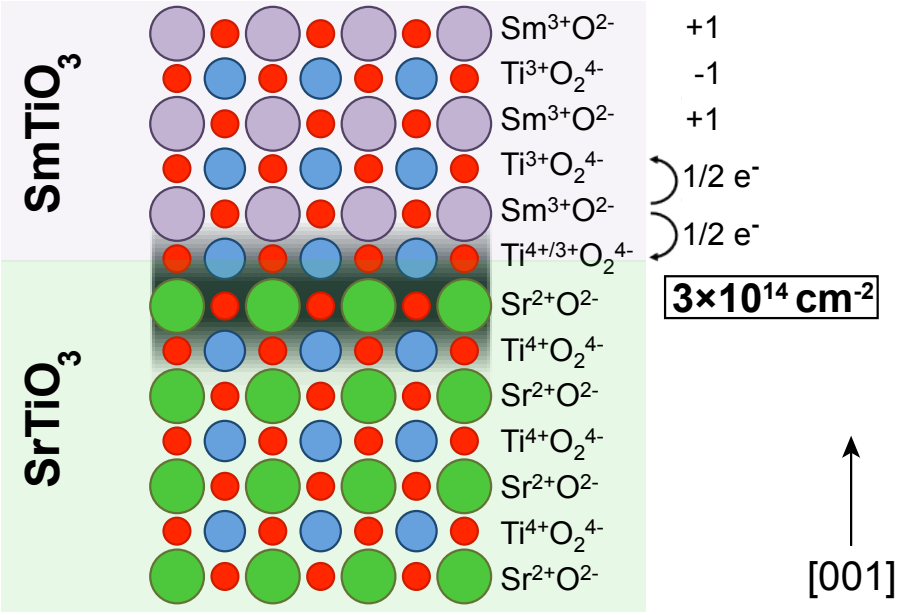

Figure 2.1: Schematic illustration of the polar discontinuity at the (001) interface of $SmTiO_3$ and $SrTiO_3$, leading to an electronic reconstruction at the interface and formation of a tightly confined two-dimensional electron liquid (shaded in black)

.

potential that is unsustainable in the polar material. This instability can be avoided by compensating, free electron charge. Each RO layer in the polar RTiO$_3$ can be visualized as contributing 1/2 of an electron per surface unit cell to the TiO_2 layers above and below. At the interface with $SrTiO_3$, the interfacial TiO_2 layer receives 1/2 electron from RO layer above but does not get any charge from charge neutral SrO layer below. This results in a mixed valence nature of the interfacial TiO_2 layer with an excess 1/2 electron per surface unit cell, and an equivalent free, mobile sheet electron density of $\approx 3.5\times10^{14}$ cm^{-2} at each such hetero-interface.

In the following study, we determine the nature of charge accumulation at the RTiO$_3$/$SrTiO_3$ system as a function of increasing RTiO$_3$ (in this case, $SmTiO_3$) thickness.

2.2 Results: (001) 2DELs

Fig. 2.2(a) shows the schematic of the heterostructures grown for this study. The thickness of the $SrTiO_3$ layer is kept constant at 60 nm, and the $SmTiO_3$ thickness is varied from 1 unit cell to 4 unit cells (u.c.). The layers were grown on (001) $(LaAlO_3)_{0.3}(Sr_2AlTaO_6)_{0.7}$ (LSAT) substrates using hybrid molecular beam epitaxy technique described in Chapter 1 and [54, 55]. $SrTiO_3$ and $SmTiO_3$ were grown at a substrate temperature of 900 °C within the MBE growth window and RHEED oscillations were used to monitor and calibrate the thickness of $SrTiO_3$ and $SmTiO_3$ layers. X-ray diffraction (XRD) was used to confirm the structural quality of the heterostructures and 50 nm Ti/400 nm Au Ohmic contacts were deposited in Van-der-Pauw geometry for Hall and resistivity measurements.

Fig. 2.2 shows transport measurements on $SmTiO_3/SrTiO_3$ heterostructures with ultra-thin $SmTiO_3$ top layers. The sheet resistance of the heterostructure increases when $SmTiO_3$ layer thickness is decreased from 4 to 1 unit cells. The 4 u.c. sample shows metallic behavior at all temperatures, except for a small upturn at low temperatures that has been attributed to weak localization [78]. The sample with 3 u.c. $SmTiO_3$ shows similar behavior, albeit with increased sheet resistance. Further decrease in $SmTiO_3$ thickness to 1 or 2 unit cells causes sheet resistance at 300 K to approach the quantum resistance, h/e^2, as defined by the Mott-Ioffee-Regel (MIR) limit ($\sim$25 kΩ/square) [80], and they undergo metal-to-insulator transition at temperatures below 150 K.

The sheet carrier density shows a systematic decrease from the theoretically expected value of 3×10^{14} cm^{-2} for thick $SmTiO_3$ layers. The temperature dependence of sheet carrier density shows a much more complex behavior, especially for 1 u.c. and 2 u.c.

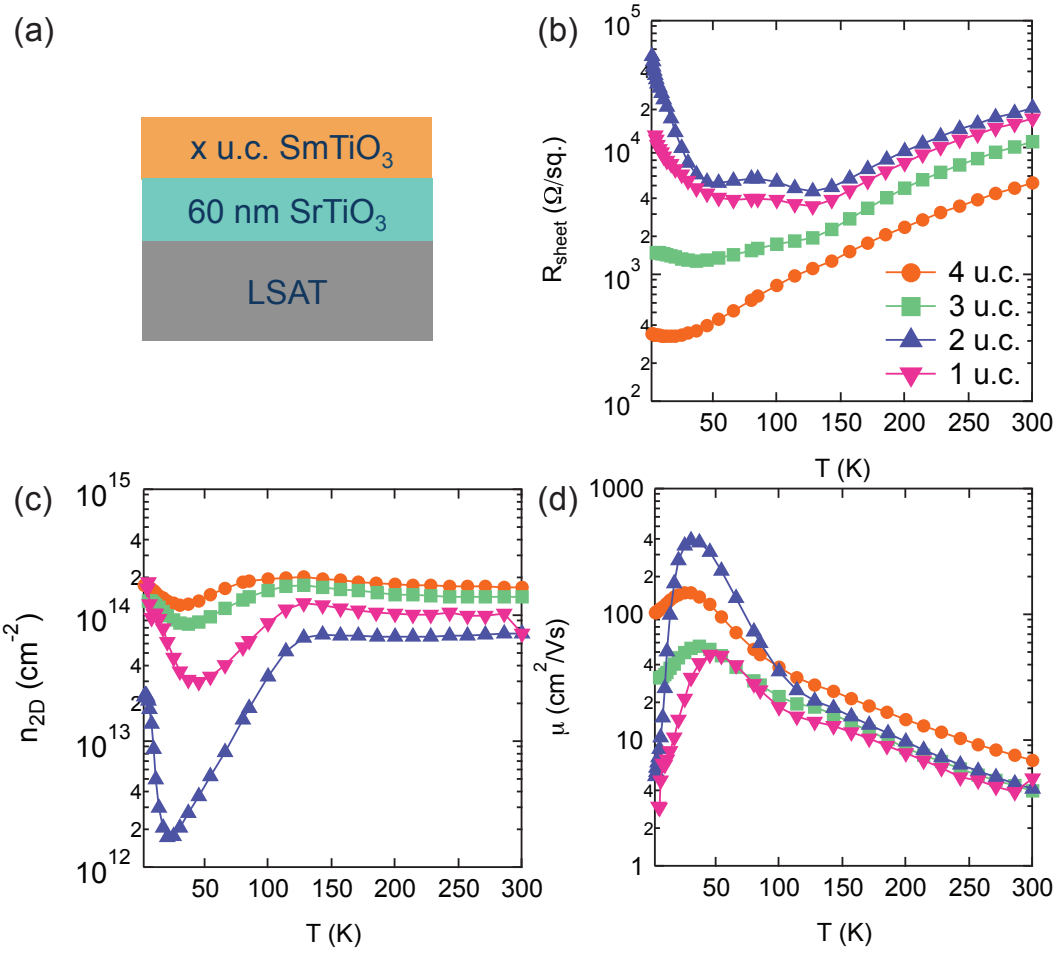

Figure 2.2: (a) Schematic of the heterostructure. (b) Temperature dependence of sheet resistance, (c) sheet carrier density, and (d) mobility for $SmTiO_3/SrTiO_3$ (001) interfaces with ultra-thin $SmTiO_3$ layer thickness.

$SmTiO_3$ layers, with a large drop in apparent sheet carrier density at the onset of the metal-to-insulator transition, followed by a sharp recovery. The reason for this behavior is not clearly understood and requires further studies. However, even for 1 u.c. of $SmTiO_3$ on $SrTiO_3$, a large sheet carrier density of 8×10^{13} cm^{-2} is obtained. With increasing $SmTiO_3$ layer thickness, the sheet carrier density gradually increases to the theoretically expected value of 1/2 an electron per surface unit cell as shown in Fig. 2.3. This behavior is in striking contrast with $LaAlO_3/SrTiO_3$ heterostructures, where a critical thickness of

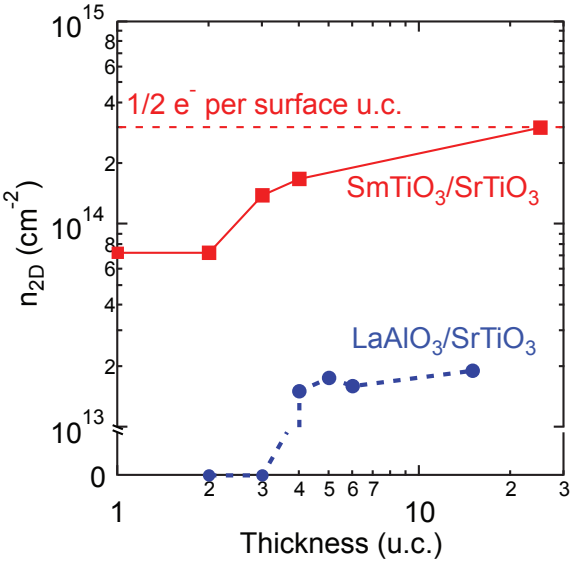

Figure 2.3: Sheet carrier density as a function of $SmTiO_3$ (in red) or $LaAlO_3$ (blue) layer thickness for respective interfaces with $SrTiO_3$, showing critical thickness for 2DEG formation in $LaAlO_3/SrTiO_3$ [4], which is absent in $SmTiO_3$/ $SrTiO_3$.

minimum 4 u.c. $LaAlO_3$ is required to obtain the space charge layer. Possible explanations for reduced sheet carrier density (and critical thickness) at such interfaces include presence of surface states on the polar $LaAlO_3$ interface that traps charge from the 2DEG in case of ultra thin films [81]. A difference in the nature (or possibly lower density) of surface states on polar $SmTiO_3$ would explain the reduced interface charge density and lack of critical thickness for $SmTiO_3/SrTiO_3$ interfaces. However, the carrier densities obtained at $LaAlO_3/SrTiO_3$ are also lower, even for thick $LaAlO_3$ layers, making a direct comparison difficult.

2.3 Polar Discontinuity along (111) Heterostructures

Recently, theoretical calculations of 2DELs in $SrTiO_3$ along (111) interfaces have predicted possibility of a wide range of new phenomena due to the distinct topology of

transition metal bilayers that form a buckled honeycomb lattice, similar to graphene. Some of the predicted phenomena in quantum wells along (111) interfaces include topological insulators [82, 83, 84], Dirac points on the Fermi surface [83, 85, 86], and nematic magnetic phases [86]. Tailoring of magnetic ordering in (001) $R\mathrm{TiO_3}/\mathrm{SrTiO_3}$ 2DELs can be extended to (111) 2DELs, opening up new means to access unexplored magnetic phases.

To obtain 2DELs at (111) interfaces, we need to understand the nature of polar discontinuity along the (111) interfaces of $R\mathrm{TiO_3}$ and $\mathrm{SrTiO_3}$. (111) surfaces in both $R\mathrm{TiO_3}$ and $\mathrm{SrTiO_3}$ are polar and highly charged, as depicted in Fig. 2.4. $\mathrm{SrTiO_3}$ contains stacks of Ti^{+4} and $(\mathrm{SrO_3})^{-4}$ planes along [111], whereas $R\mathrm{TiO_3}$ contains stacks of Ti^{+3} and $(R\mathrm{O_3})^{-3}$. The polar discontinuity at the interface is similar to the (001) case, resulting in 1/2 an electron of excess charge in the interfacial Ti layer and an equivalent charge density of $\approx 2\times10^{14}$ cm^{-2} at each such hetero-interface. The (111) 2DEL density is less than 3.5×10^{14} cm^{-2} of (001) $R\mathrm{TiO_3}/\mathrm{SrTiO_3}$ 2DELs due to a larger surface unit cell interface area along (111).

At (001) interfaces, density functional calculations (DFT) show tight confinement of a large portion of the 2DEL to the interface [87, 88]. Such a confinement favors d_{xy} derived bands – with high mass in out-of-plane direction – to form the lowest occupied subband(s), while a significant charge density is also accommodated in the $\mathrm{d}_{xz,yz}$ subbands due to their higher density of states [89]. In contrast, the t_{2g} orbitals are expected to be equivalent and degenerate along (111) interfaces, with six-fold symmetry in the (111) plane. Recent results from angle resolved photoemission spectroscopy (ARPES) confirm this hypothesis for 2DELs formed at (111) $\mathrm{SrTiO_3}$ surfaces with anisotropic in-plane band masses [90, 91]. In this experiment, we study (111) $R\mathrm{TiO_3}/\mathrm{SrTiO_3}$ interfaces

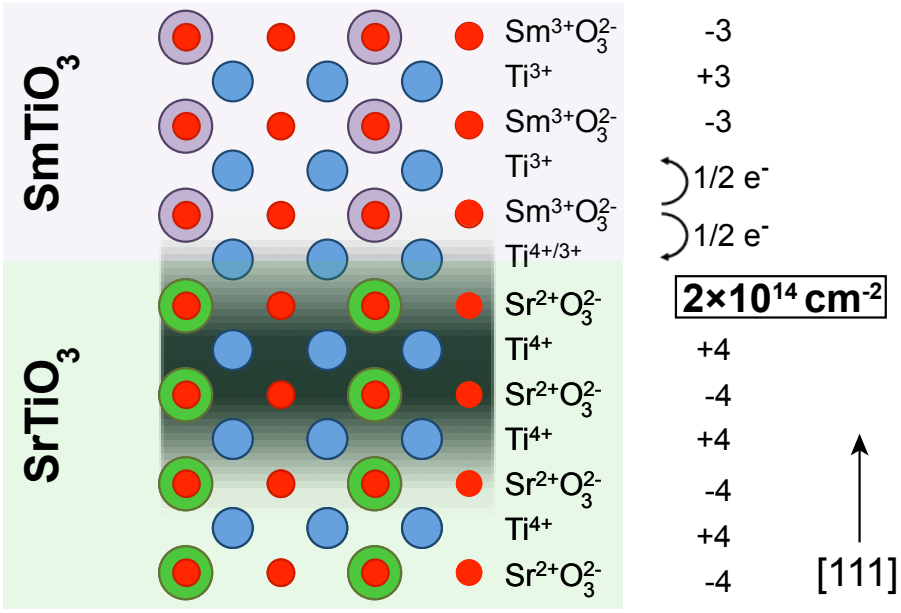

Figure 2.4: Schematic illustrating polar discontinuity at the (111) interface of $SmTiO_3$ and $SrTiO_3$, leading to an electronic reconstruction at the interface and formation of a two-dimensional electron liquid (shaded in black).

to investigate existence of 2DELs due to polar discontinuity and its properties (carrier density, mobility and anisotropy). The results are also compared with 2DELs at (001) interfaces.

2.4 Results: Growth and Structure of (111) Interfaces

$SmTiO_3/SrTiO_3$ interfaces (with $SmTiO_3$ as the top layer) were grown on (111) surfaces of $(LaAlO_3)_{0.3}(Sr_2AlTaO_6)_{0.7}$ (LSAT) substrates using hybrid molecular beam epitaxy technique described in Chapter 1 and [54, 55]. $SrTiO_3$ and $SmTiO_3$ were grown at 900 °C within the MBE growth window obtained for (001) interfaces. RHEED was used

to monitor the growth of $SrTiO_3$ and $SmTiO_3$ layers. No oscillations in intensity were observed for either layers, in contrast to the (001) case. RHEED patterns for $SrTiO_3$ on LSAT (111) always started out spotty for the initial layers growing on the substrate indicating three dimensional growth. This is expected due to the nature of highly charged (111) interfaces, which might prefer to either reconstruct or relax to form 3D islands with low energy facets. However, RHEED was observed to become streaky beyond growth of 4 nm of $SrTiO_3$ indicating a smooth interface with $SmTiO_3$ as shown in Fig. 2.5(c). The $SrTiO_3$ thickness was determined using Laue thickness fringes from XRD and confirmed using cross-section transmission electron microscopy. $SmTiO_3$ layer thickness was kept constant at 2 nm. Thicker $SmTiO_3$ layers (> 2 nm) showed rough surfaces and spotty RHEED patterns, indicating nucleation of defects. Although this problem has been observed for (001) $LaTiO_3$ surfaces [92], it was not observed for (001) $SmTiO_3$.

Fig. 2.5 shows structural characterization results of a 2 nm $SmTiO_3$ / 10 nm $SrTiO_3$ / LSAT (111) sample. On-axis XRD of the heterostructure in Fig. 2.5(a) shows Laue thickness fringes around the 222 reflection of $SrTiO_3$ indicating good structural quality. Atomic force microscopy shows the surface of $SmTiO_3$ layer with unit-cell step height. Smooth surfaces and absence of RHEED intensity oscillations indicate a step-flow growth mode (instead of layer-by-layer) for both $SrTiO_3$ and $SmTiO_3$ layers. Similar surfaces were obtained for $SrTiO_3$ (111) films and should allow for a smooth interface between the two materials. Cross-sectional TEM using high-angle annular dark field scanning transmission electron microscopy (HAADF-STEM) shows a relatively abrupt (111) interface between $SrTiO_3$ and $SmTiO_3$, confirming epitaxial growth without faceting (courtesy of Jack Y. Zhang).

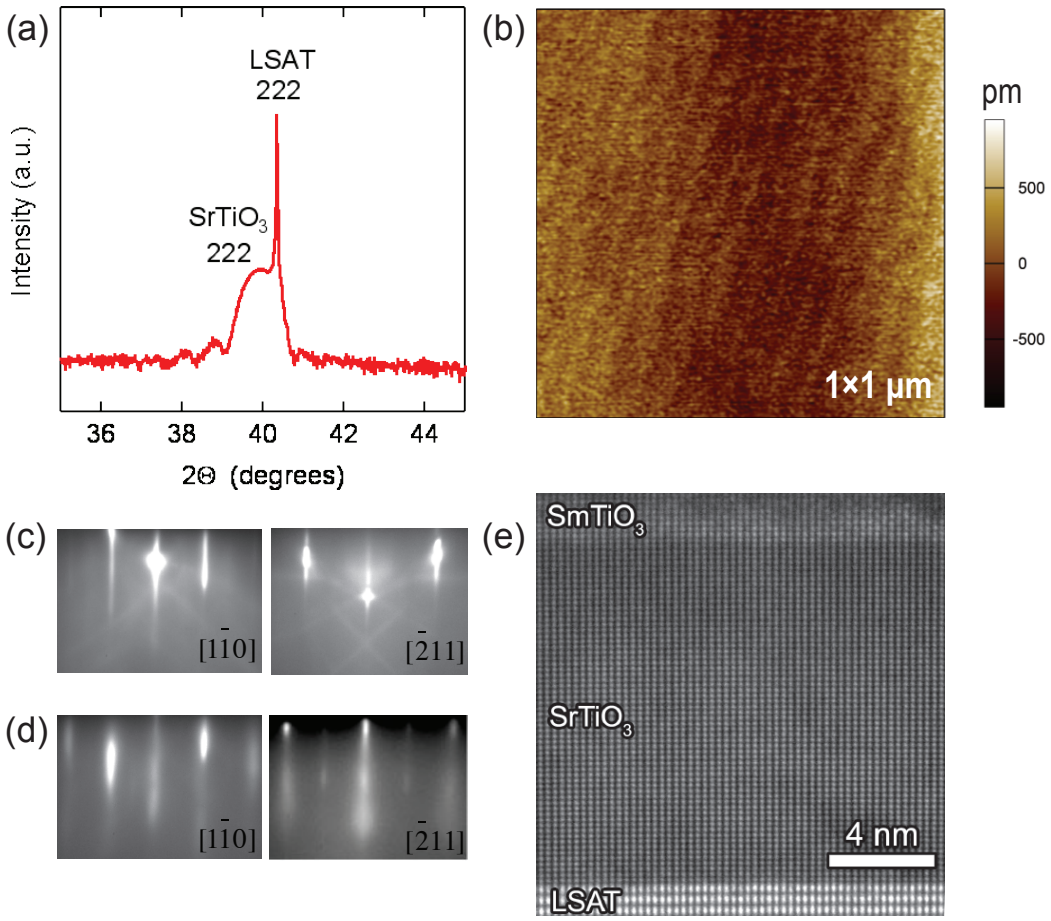

Figure 2.5: (a) On-axis XRD spectrum of a 2 nm $SmTiO_3$ / 10 nm $SrTiO_3$ / LSAT (111) sample. (b) Atomic force micrograph showing the surface morphology of the $SmTiO_3$ (111) layer. RHEED image of the (c) $SrTiO_3$ (111) and (d) $SmTiO_3$ (111) film surface along $[1\bar{1}0]$ and $[\bar{2}11]$ azimuths. (e) HAADF/STEM cross-section image. The image is a sum of a series of fast acquisition images using rigid registration. This figure is adapted with permission from [5].

2.5 Results: Transport Properties of (111) 2DELs

Electrical characterization was performed on samples by depositing 50 nm Ti/400 nm Au contacts in Van der Pauw geometry and Hall measurements were performed in a Physical Property Measurement System (Quantum Design). Linear Hall resistance was found up to ± 9 T at all measured temperatures (300 K to 2 K) and single carrier model

was used to estimate the carrier density ($R_H = 1/qn_{2D}$). Later, Hall bar devices (width and length: 5 mm) were fabricated along $[1\bar{1}0]$ and $[\bar{1}\bar{1}2]$ directions of the samples to determine in-plane anisotropies. The Hall bars were cleaved for electrical insulation and to remove any parasitic influences, and measured simultaneously to minimize experimental error.

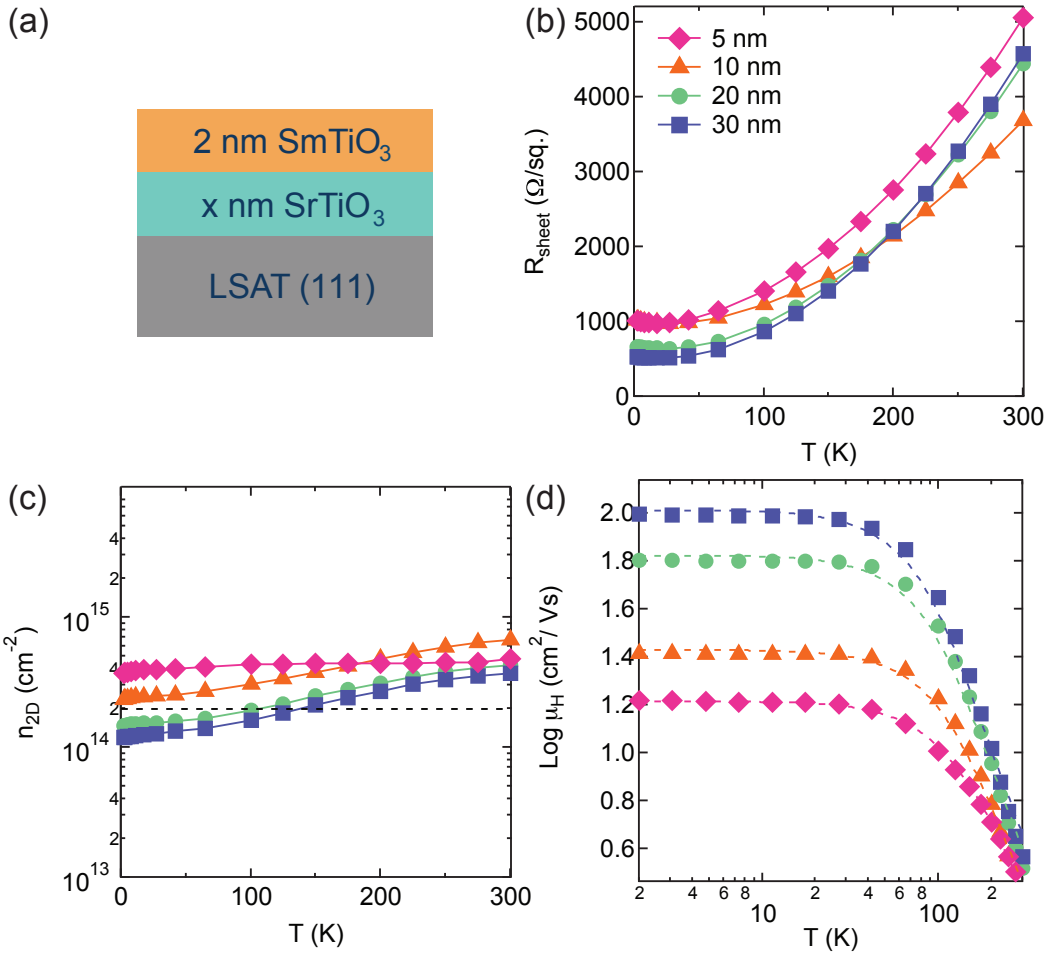

Figure 2.6: (a) Schematic of the heterostructures. (b) Sheet resistance, (c) sheet carrier density, and (d) Hall mobility (μ_H) as a function of temperature for (111) $SmTiO_3/SrTiO_3$ heterostructures with varying $SrTiO_3$ thicknesses. The solid lines in (b) and (c) are a guide to the eye. The black dotted line in (c) indicates the theoretically expected carrier density. The dotted lines in (d) are a fit using equation 2.1. This figure is adapted with permission from [5].

Transport properties were measured on different $SmTiO_3/SrTiO_3$ bilayers with varying $SrTiO_3$ thickness. Fig. 2.6(a) shows sheet resistance as a function of temperature. All samples showed metallic behavior from 300 K to 2 K, and Hall measurements indicated n-type carriers. The sheet carrier density for samples (Fig. 2.6(b)) was found to be nearly independent of $SrTiO_3$ thickness, and within a factor of 3 of the theoretically expected carrier density (2×10^{14} cm^{-2}). Thicker $SrTiO_3$ samples showed sheet carrier densities closer to the expected values. No strong and systematic dependence of carrier density on $SrTiO_3$ thickness was found, indicating lack of significant parasitic conduction from oxygen vacancies, similar to the (001) 2DELs. The reasons for small deviations from the theoretical carrier density are difficult to differentiate. The presence of small amount of disorder at the these interfaces can introduce additional carriers. An apparent temperature dependence of carrier density is seen, and a possible explanation is conduction by carriers with different mobilities (in multiple bands of the anisotropic Fermi surface). In such a case, using a single carrier model for the estimating the carrier density from the Hall coefficient (R_H) may introduce some error, which should be small at 300 K, where the scattering from phonons is strong for all carriers. The 5 nm $SrTiO_3$ is an exception, where carrier density seems independent with temperature, which is probably due to confinement of carriers in the $SrTiO_3$, and interface roughness scattering limits the mobility of all carriers equally at low temperatures.

The electron mobility of the 2DELs as a function of temperature is shown in Fig. 2.6(c). At first glance, the mobility trend seems qualitatively similar to the ones observed for (001) $SmTiO_3/SrTiO_3$ 2DELs [66]. The low-temperature mobility increases with $SrTiO_3$ layer thickness. This is consistent with reduced scattering from the interface(s), as carriers can spread and 2DEL interface is further away from the substrate. Such a dependence indicates that even for relatively thick $SrTiO_3$ layers, there is a significant spread for the 2DEL and a weak confinement of the 2DEL to the $SmTiO_3/SrTiO_3$ (111) interface (as

was also found in ARPES [90, 91]).

The temperature-dependence of mobility in $SrTiO_3$ 2DELs can be described using the following contributions [66]: low-temperature limit of mobility from interface roughness scattering (μ_0), electron-electron scattering limited mobility ($\mu_{ee} = 1/\alpha T^2$), and longitudinal optical (LO) phonon limited mobility (μ_{LO}), as described in Chapter 1. The total mobility according to Matthiesen's rule is:

$$\mu^{-1} = \mu_0^{-1} + \mu_{ee}^{-1} + \mu_{LO}^{-1} \tag{2.1}$$

The dotted lines in Fig. 2.6(c) show fits to the mobility for all samples using equation 2.1. Table 2.1 shows the extracted parameters (α, ω_{LO}) from fits to mobility for different samples. The paramater α is a measure of the strength of electron-electron scattering, and ω_{LO} is the averaged energy of the LO phonons contributing to the LO phonon scattering. Except for the thinnest (5 nm) $SrTiO_3$ sample, all samples needed both electron-electron scattering and LO phonon scattering contributions to obtain good fits over the entire temperature range. This is similar to mobility dependence in bulk $SrTiO_3$ [66, 93], but very different from (001) 2DELs, which are dominated by μ_{ee} term all the way to 300 K. The averaged LO phonon energy ($\hbar\omega_{LO}$) from the fits are ~ 45 meV, lower than values obtained for similar fits in bulk $SrTiO_3$ samples (60-100 meV) [66]. The lower effective phonon frequencies for (111) 2DELs can be explained by a lower screening of ionic potentials, indicating lower effective mass (confinement) and lower density of states at the Fermi surface of (111) 2DELs. The α paramater, indicating the strength of electron-electron scattering, increases with confinement of the 2DEL. This explains why the 5 nm $SrTiO_3$ sample (most confined) needs no contribution from LO phonon scattering to obtain a good fit. This is consistent with an increase in density of states

Table 2.1: Fit parameters for mobility fits to (111) 2DELs in Fig. 2.6(c)

$SrTiO_3$ thickness	α (Vs/cm^2K^2)	$\hbar\omega_{LO}$ (meV)
5 nm	3.43×10^{-6}	-
10 nm	2.61×10^{-6}	47
20 nm	1.69×10^{-6}	44
30 nm	1.42×10^{-6}	44

due to confinement, leading to a complete screening of the LO phonon [66].

There is an anisotropy of the band dispersion in the $SrTiO_3$ (111) interface plane [90, 91] which is expected to be reflected in transport properties. Along the $[\bar{1}\bar{1}2]$ direction, a heavier subband is filled in addition to two lighter ones, whereas $[1\bar{1}0]$ direction has only light subbands occupied [91]. Fig. 2.7 shows Hall bar measurements along the two directions for the 20 nm $SrTiO_3$ sample, showing an asymmetry in the sheet carrier density and mobility. The Hall bar along $[1\bar{1}0]$ shows a lower carrier density (as expected for a lower mass, leading to low density of states) and higher mobility than the $[\bar{1}\bar{1}2]$ direction. At low temperatures, the mobility saturates and is dominated by interface roughness scattering. Less confined carriers with lower mass are further from the interface and experience less scattering, resulting in higher mobility. Furthermore, the low temperature limit of the mobility (μ_0) is also determined by the bandstructure [94].

2.6 Conclusions

In this Chapter, we have discussed the phenomenon of polar discontinuity in (001) and (111) $SmTiO_3/SrTiO_3$ interfaces, and the origin of two-dimensional electron liquids in such heterostructures. In case of (001) 2DELs, we have studied the effect of ultra-thin $SmTiO_3$ layers in $SmTiO_3/SrTiO_3$ heterostructures on the measured sheet carrier density

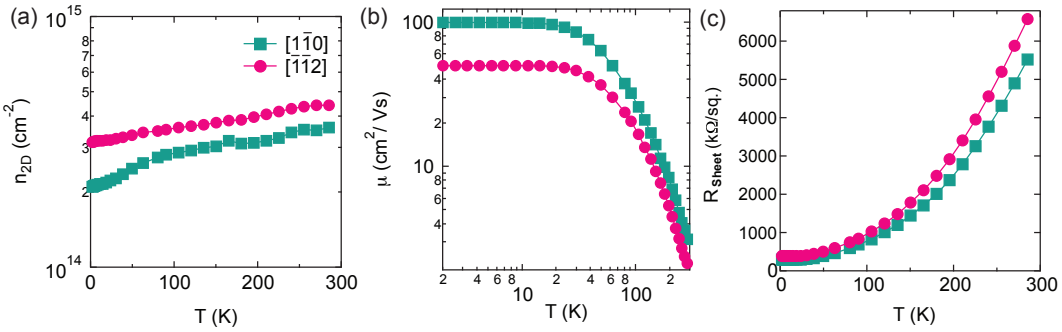

Figure 2.7: (a) Sheet carrier density and (b) Hall mobility, and (c) sheet resistance as a function of temperature measured along [1$\bar{1}$0] and [$\bar{1}\bar{1}$2] directions in the (111) interface plane of 20 nm $SrTiO_3$ sample shown in Fig.2.6. The lines are a guide to the eye. This figure is adapted with permission from [5].

of the 2DELs. We analyzed the transport properties of such 2DELs and compared the results with $LaAlO_3/SrTiO_3$ interfaces. It is shown that, unlike the $LaAlO_3/SrTiO_3$, no critical thickness exists for formation of 2DELs in $SmTiO_3/SrTiO_3$ interfaces. However, there is a systematic reduction in the carrier density of the 2DELs for ultra-thin $SmTiO_3$ layers. Such a reduction can be used to control (and reduce) the sheet carrier density in such 2DELs to values that can be depleted using traditional gating (and allow pinch-off) in oxide field-effect transistors, as shown successfully in [95] and [71].

In addition, we have also shown that (111) $SmTiO_3/SrTiO_3$ interfaces also exhibit an interfacial mobile space charge, with sheet carrier densities close to what is expected from polar discontinuity at the interface. Transport studies provide strong evidence that the (111) 2DELs are significantly less confined to the $SmTiO_3/SrTiO_3$ interface than that at (001) 2DELs, which is consistent with bandstructure observations in literature. It is shown that confining the 2DELs between the $SmTiO_3$ barriers and the substrate enhances electron-electron interactions and suppresses LO phonon scattering contributions. The anisotropy in the $SrTiO_3$ (111) Fermi surface is apparent in the measured

Hall mobility and carrier density, indicating that the interfaces studied here of sufficient quality to exhibit intrinsic properties of the 2DELs. In the future, such 2DELs should be highly suitable to explore the theoretical predictions at (111) interfaces, and requires development of confined, ultra-thin $SrTiO_3$ in $RTiO_3/SrTiO_3/RTiO_3$ quantum wells with smooth interfaces.

Chapter 3

Subband Structure of $SrTiO_3$ Using Resonant Tunneling

3.1 Subband Structure Of $SrTiO_3$

The two-dimensional electron liquids at $LaAlO_3/SrTiO_3$ or $R TiO_3/SrTiO_3$ (R: trivalent rare earth element like Gd or Sm) contain high densities of mobile charge that reside in the $SrTiO_3$ layer [32, 33]. It is essential to have a quantitative description of the subband structure of this 2DEL in $SrTiO_3$, to understand its properties. The conduction band of $SrTiO_3$ is derived from Ti 3d t_{2g} states. In bulk cubic $SrTiO_3$, the degeneracy of the six-fold t_{2g} states is lifted by spin–orbit coupling and tetragonal distortion occurring near 110 K. As a result, the t_{2g} orbitals are split into d_{xy}, d_{xz} and d_{yz} states, as shown in Fig. 3.1. At low electron doping, only the lowest energy subband would be occupied. However, the high density of carriers from the 2DEL cause filling of multiple subbands. Many recent theoretical works support this picture [96, 97, 98, 87, 99, 88, 100, 101, 102, 103, 104, 105]. Most of the studies consider the 2DEL carrier density of 3×10^{14} cm^{-2}, which is the theoretically expected value from polar discontinuity at $LaAlO_3/SrTiO_3$ and $R TiO_3/SrTiO_3$ interfaces.

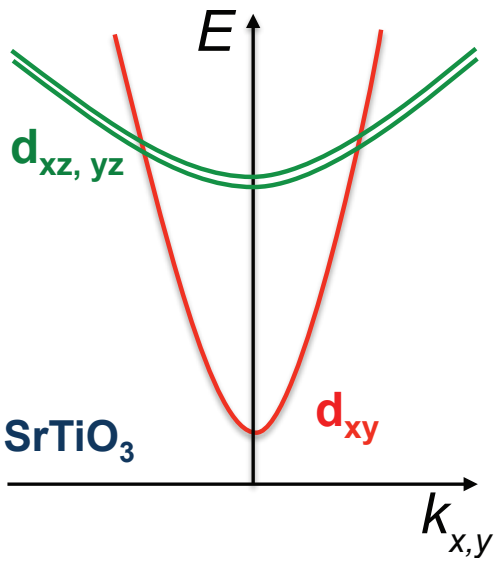

Figure 3.1: Schematic showing crystal field splitting in $SrTiO_3$ as a result of tetragonal distortion.

While results between theoretical models differ quantitatively, the qualitative picture is consistent irrespective of the framework: the confining electric field at the (001) interface gives rise to a low-lying d_{xy} subband with a low in-plane mass that accomodates a large fraction of the 2DEL density. In addition, closely spaced higher energy subbands of d_{xy} and $d_{xz,yz}$ derived states are also predicted to be occupied. The d_{xy} subband is closely confined to the interface due to its high out-of-plane mass, whereas $d_{xz,yz}$ states have low out-of-plane mass and are less confined. The relative role of different subbands in mechanisms like electrical transport, superconductivity, magnetism, and spin-orbit coupling effects is subject of active investigation [106, 107, 100, 108, 109, 110].

In experiments, the subband structure of $SrTiO_3$-based space charge layers have been studied either using ARPES [90, 111] for surface 2DELs, or Shubnikov-de Haas oscillations for buried 2DELs [112, 113, 114, 115]. They confirm the picture that carriers from different subbands contribute to electrical conduction. However, only a small fraction

of the carriers have been shown to cause Shubnikov-de Haas oscillations. Furthermore, the nature of oscillations tends to be complex, and further theoretical understanding is necessary for a good comparison with experiments.

In this Chapter, we present a more direct method of probing the 2DEL subbands using out-of-plane transport. We utilize resonant tunneling between two parallel 2DELs separated by a tunnel barrier to yield resonant features in dI/dV and d^2I/dV^2 as a function of applied voltage V, where I is the tunneling current. Resonant tunneling occurs when the subbands in the two 2DELs line up in energy as shown in Fig. 3.2. The energy minima of the subbands can be obtained directly, as resonant tunneling requires conservation of (in-plane) momentum of electrons parallel to the barrier:

$$E_1 - \frac{\hbar^2}{2m^*}(k_{||}^2 + k_z^2) = E_2 + \frac{\hbar^2}{2m^*}(k_{||}^2 + (k_z')^2) \tag{3.1}$$

where E_1 and E_2 are the energies of participating subbands, m^* is the effective subband mass, $k_{||}$ is the in-plane momentum vector, k_z and k_z' are out-of-plane momentum vectors respectively.

Such studies have been performed in GaAs/AlGaAs systems [116], but have never before been experimentally demonstrated in perovskite oxides. It is also noted that, currently, $R\mathrm{TiO_3}/\mathrm{SrTiO_3}$ interface is the only perovskite oxide system that allows for formation of two parallel and adjacent 2DELs that is required for this experiment. Here, we utilize $\mathrm{SrTiO_3}/\mathrm{GdTiO_3}/\mathrm{SrTiO_3}$ heterostructures, with a high density 2DEL with close to theoretically expected charge density of 3×10^{14} cm^{-2} at each $\mathrm{SrTiO_3}/\mathrm{GdTiO_3}$ interface [33]. $\mathrm{GdTiO_3}$ in the structure also serves as the tunnel barrier as shown in Fig. 3.2. Shubnikov-de Haas oscillations measured in a single $\mathrm{SrTiO_3}/\mathrm{GdTiO_3}$ interface 2DEL

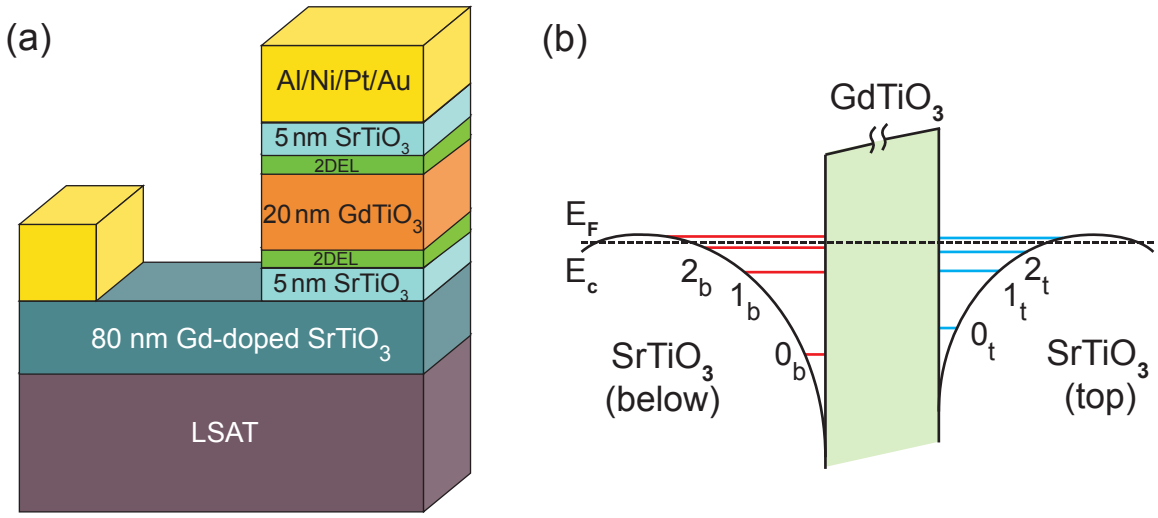

Figure 3.2: (a) Schematic of the tunnel device. (b) Schematic energy diagram of the subband configuration at a $SrTiO_3/GdTiO_3/SrTiO_3$ heterostructure at zero applied bias and low temperature. A slight asymmetry in the carrier concentration and resulting subband spacing between the two 2DELs is assumed. The number of subbands and band bending shown is for illustrative purposes and schematic is not meant to be quantitative. E_C and E_F (dashed line) indicate the conduction band edge and Fermi level, respectively. The numbers (0,1,2) refer to the subband indices, and the subscripts to top and bottom 2DELs, respectively. (Adapted with permission from [6])

were interpreted as either arising from a single, spin–split subband or two subbands [113]. Only 20%-30% of the total measured Hall carrier density was shown to give rise to oscillations. In this experiment, we show experimental evidence of resonant tunneling in $SrTiO_3/GdTiO_3/SrTiO_3$ heterostructures. We obtain the subband spacings in $SrTiO_3$ and compare the results with theoretical predictions for such high density 2DELs.

3.2 Experimental Design and Fabrication

$SrTiO_3/GdTiO_3/SrTiO_3$ heterostructures were grown on (001) $(LaAlO_3)_{0.3}(Sr_2AlTaO_6)_{0.7}$ (LSAT) substrates using hybrid molecular beam epitaxy technique described in

Chapter 1 and [54, 55]. A 80 nm thick Gd doped $SrTiO_3$ buffer layer serves as a contact to the bottom 2DEL. The carrier density in the Gd doped layer is around 1×10^{19} cm^{-3}, which is an order of magnitude lower than the effective 3D charge density in the 2DEL in the 5 nm wide undoped $SrTiO_3$ layer. The $GdTiO_3$ barrier thickness was around 20 nm. The resonant tunnel device shown in Fig. 3.2 was fabricated using established cleanroom fabrication techniques. Optical contact lithography was used to define resonant tunnel diodes with dimensions: 10×10 μm. 40 nm Al/ 20 nm Ni/ 50 nm Pt/ 300 nm Au contacts were evaporated using e-beam for Ohmic contacts. The Ohmic contact to the top 2DEL was deposited on the top-most $SrTiO_3$ layer, and then used as a hard mask for an inductively coupled plasma (ICP) assisted dry etch with BCl_3 gas to form square vertical diodes. The etch exposed the Gd doped $SrTiO_3$ layer for depositing the bottom Ohmic contact. The entire device was then covered with 400 nm e-beam evaporated SiO_2 layer (not shown in the schematic), followed by an CF_4 gas assisted ICP dry etch to expose the Ohmic contacts covered in SiO_2. 300 nm thick Au pads were deposited on top of the Ohmic contacts to create larger contacts over the SiO_2 barrier layer to facilitate wire bonding. Keithley 2400 Broad Purpose Source Meter was used to measure I-V curves using voltage-controlled measurements, with bias applied to the top Ohmic contact. I-V curves were collected at different voltage sweep rates, across different devices to ensure that the data is consistent. Temperature dependent measurements were performed in a Physical Property Measurement System (Quantum Design PPMS Dynacool).

3.3 Results: Difference between Two 2DELs

It has been routinely observed in III–V and III–N heterostructures that there exists an inherent asymmetry between interfaces and the resulting two-dimensional electron gases when material X is grown on top of material Y, vs. Y grown on top of X [117, 118].

A similar asymmetry is observed between the 2DELs found at $SrTiO_3/GdTiO_3$ and $GdTiO_3/SrTiO_3$ interfaces, respectively. In particular, the 2DEL at the $SrTiO_3/GdTiO_3$ interface (henceforth referred to as top 2DEL) shows slightly lower carrier concentration ($\sim 2\times10^{14}$ cm^{-2}). This is in comparison to 2DEL at the $GdTiO_3/SrTiO_3$ interface (bottom 2DEL) that shows the full expected carrier concentration. Fig. 3.3 shows results from Hall measurements used to independently determine the carrier concentrations at the two interfaces. Two of the many samples characterized are shown here, one with $GdTiO_3$ grown on top of $SrTiO_3$, and another with $SrTiO_3$ grown on top of $GdTiO_3$. LSAT (001) substrates were used in both cases, and results were found to be relatively independent of the layer thicknesses in each case. The top 2DEL carrier density is seen to be more temperature dependent. A careful analysis of the different interfaces using high angle annular dark field scanning transmission electron microscopy (HAADF-STEM), indicated a slighty higher interface roughness for the top 2DEL interface, which can lead to increased carrier trapping at lower temperatures [119]. The asymmetry is also reflected in the Hall mobility, with top 2DEL measuring $\sim$ 80 cm^2/V·s at 2 K, whereas bottom 2DEL measured $\sim$ 320 cm^2/V·s.

3.4 Results: Tunneling between Two 2DELs

Fig. 3.4 shows dI/dV and d^2I/dV^2 characteristics obtained from I-V measurements at different temperatures. There exists an exponentially increasing background current in the tunnel spectra due to non-resonant tunneling of electrons which is caused by processes that either do not conserve in-plane momentum or involve phonon-assisted tunneling. The features of subband resonant tunneling are superimposed atop the background current, and are indicated by arrows in Fig. 3.4. The presence of resonant tunneling features indicates that $GdTiO_3$ acts as a tunnel barrier with reasonable quality, such

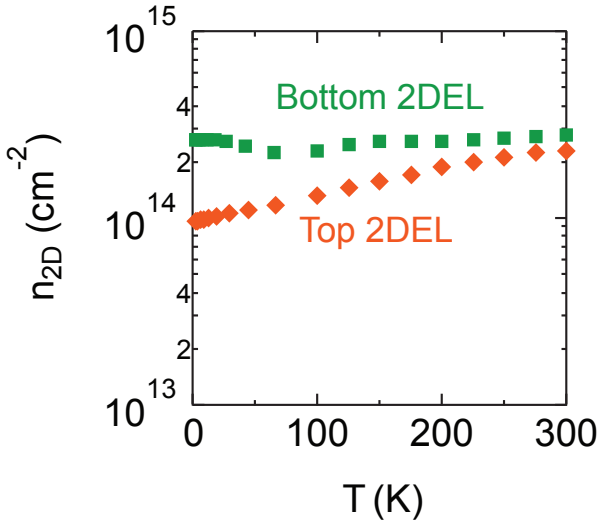

Figure 3.3: Temperature dependence of sheet carrier density n_{2D} of the 2DELs from a 5 nm $GdTiO_3$/80 nm $SrTiO_3$/LSAT substrate (labeled as 'bottom 2DEL'), and a 98 nm $SrTiO_3$/ 10 nm $GdTiO_3$/LSAT substrate (labeled 'top 2DEL'). (Adapted with permission from [6])

that any loss of momentum conservation due to defects in the barrier is insufficient to broaden or weaken the features enough to be indistinguishable from the background.

The slight asymmetry between the two 2DELs has been taken into account for the zero bias picture in Fig. 3.2, with the top 2DEL showing a reduced carrier density compared to the bottom 2DEL. The asymmetry prevents the lowest lying d_{xy} subbands on either side (denoted as 0_t and 0_b) from lining up in energy when no bias is applied. A positive bias applied to the top 2DEL would cause the subbands in the top 2DEL to be lowered in energy with respect to the bottom 2DEL. This causes the 0_t and 0_b bands to align, allowing for resonant tunneling between the states. This gives rise to the first feature at a positive bias of 89 meV that is clearly seen in the d^2I/dV^2 characteristics in Fig. 3.4(b). Hence, the separation in energy between 0_t and 0_b levels of the two 2DELs was found to be 89 meV.

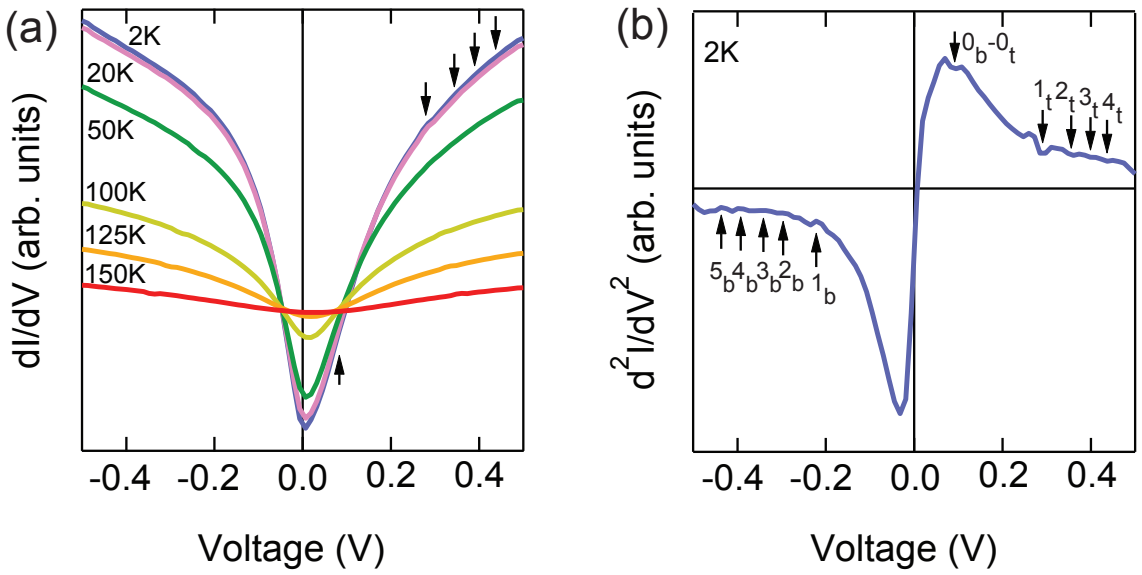

Figure 3.4: (a) dI/dV characteristics of the device at different temperatures and (b) d^2I/dV^2 characteristics of the device at 2K. The I-V data collected had 80 data points in between 0.5V and +0.5V. (Adapted with permission from [6])

.

With increasing positive bias, additional features are observed and correspond to resonant tunneling from the lowest subband of the bottom 2DEG (0_b) into various subbands of the top 2DEL (1_t, 2_t, 3_t, and so on). Under negative bias, similar features are seen, but corresponding to resonant tunneling into subbands of the bottom 2DEL. The voltages for features in dI/dV and d^2I/dV^2 are used to measure the subband separation in bottom and top 2DELs respectively. The resonance position was taken as the voltage of the minimum (dip) in the d^2I/dV^2 data taken at 2 K and is summarized in Table 3.1. The results show a relatively large separation in energy between the lowest-lying subband and the second lowest subband of 210 and 310 meV, for the top and bottom 2DEL, respectively. The subband spacing has been predicted to be very sensitive to the carrier density in $SrTiO_3$ 2DELs [96, 87]. The smaller spacing for the top 2DEL observed in our experiments is consistent with its lower carrier density, and consequently, its re-

Table 3.1: Experimental subband spacings in the top and bottom 2DEL, respectively, derived from the dip positions in the d^2I/dV^2 characteristics at 2 K. The dip positions were obtained from a set of I-V curves that had twice as many data points as those shown in Fig. 3.3(b), to maximize the accuracy with which the dip positions could be obtained. Given the number of data points, the accuracy is no better than 6.25 meV. (Adapted from [6])

Subbands (top 2DEL)	**Subband spacing (meV)**	**Subbands (bottom 2DEL)**	**Subband spacing (meV)**
0_t–1_t	200	0_b–1_b	310
1_t–2_t	65	1_b–2_b	75
2_t–3_t	44	2_b–3_b	38
3_t–4_t	38	3_b–4_b	58
-	-	4_b–5_b	44

duced confinement. Theoretical calculations predict carrier concentrations in the range of 10^{14} cm^{-2} for the lowest two subbands with d_{xy} character. The predicted spacing values between the two lowest subbands range between 160 meV to 270 meV for a carrier density of 3×10^{14} cm^{-2} (i.e. the density of the bottom 2DEL). Table 3.2 shows the different subband spacings of high density 2DELs in $SrTiO_3$ predicted in the literature [96, 98, 99, 88, 101, 87]. The larger subband spacing found in the experiment may be due to the compressive epitaxial strain (in-plane) imposed on the $SrTiO_3$ by the mismatch with LSAT substrate, further lowering the energy of the d_{xy} subbands. It can also be that the out-of-plane confinement mass in the 2DELs is larger than is commonly assumed in theory. Considering the two possibilities, the experiment and theoretical predictions are in good agreement.

Higher energy subbands are seen as a series of closely spaced features in the d^2I/dV^2 data. Four additional subbands for bottom 2DEL and three subbands for top 2DEL are observed. Although the close spacing of the subbands makes them difficult to distinguish, the separation energies are much smaller for higher lying states ($\sim$ few tens

Table 3.2: Predicted theoretical subband spacings reported in literature for high-density $SrTiO_3$ 2DELs. Only spacings between d_{xy} derived subbands are shown. The numbers in top row of the Table refer to the subband indices. (Adapted from [6])

Reference	**0–1 (meV)**	**1–2 (meV)**	**2–3 (meV)**	**3-4 (meV)**
[88]	213	37	11	5
[87]	174	14	27	-
[99] (two 2DELs)	219	57	29	43
[99] (one 2DEL)	214	64	64	100
[101]	271	26	39	45
[96]	160	80	64	56

of meV) as shown in Table 3.1. These findings are in close agreement with theoretical models also predicting closely spaced higher energy levels, as shown in Table 3.2. The predicted energy spacings for higher-lying d_{xy} subbands are on the order of 10–80 meV, similar to the observed values in experiment. Theoretical models also predict higher-lying subbands with $d_{xz,yz}$ character. However, in 2D resonant tunneling, the energy and in-plane momentum is conserved [116]. This allows for resonant tunneling only between d_{xy} states on either side of the barrier, as the first d_{xy} subband aligns with other subbands with increasing bias. Hence, we conclude that at least four of the higher lying subbands have sufficient d_{xy} character to participate in 2D–to–2D resonant tunneling.

Another theoretical study of tunnel junctions considers $SrTiO_3$ as the tunnel barrier, with a La-δ-doped layer in the middle of the barrier, and $SrRuO_3$ as the conducting electrodes [120]. This study predicts resonant tunneling via states with $d_{xz,yz}$ character. In contrast, we present a different structure based on 2D–to–2D tunneling, showing that d_{xy}–to–d_{xy} tunneling has sufficient transmission probability to give rise to resonant tunneling features. The observed subband spacings also indicate that it will be difficult to observe Shubnikov-de Haas oscillations from any subband other than the lowest-lying, d_{xy} derived subband, due to the closely spaced higher energy levels. This finding is also

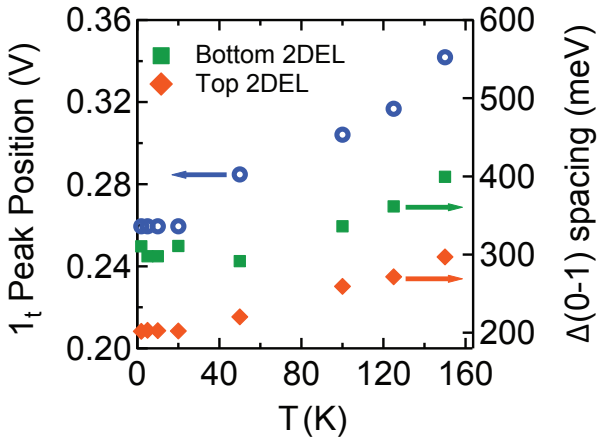

Figure 3.5: Temperature dependence of the 1_t feature (left axis) and of the 0-1 subband spacing (right axis) of the bottom and top 2DELs, respectively. (Adapted with permission from [6])

consistent with the observation of Shubnikov-de Haas oscillations from a single, spin-split subband [113].

Fig. 3.5 shows the temperature dependence of the 1_t peak position and the 0–1 subband spacings. The peak position and the subband spacings are seen to increase with increasing temperature. Similar effects have been observed in tunneling studies related to Si and III–V subbands, and have been attributed to thermal activation of higher-lying, less spatially confined subbands, that result in changing the potential profile and cause increased subband spacings. Between 2 K and 150 K, the subband spacings for top 2DEL and bottom 2DEL increase by 47% and 28%, respectively.

Finally, it is important to consider inelastic processes like phonon emission and absorption as the origin for such features in dI/dV and d^2I/dV^2 curves. The highest phonon frequency in oxide structures is $\sim$ 0.1 eV – substantially smaller than the positions of 1_t and 1_b. The position of 0_b–0_t feature can be assigned to an inelastic process, purely

on an energetic basis. However, if that were the case, such a feature should appear with a companion at negative bias, which it does not. This indicates that inelastic processes cannot explain the prominent features (1_t, 0_b–0_t, 1_b). Furthermore, the temperature dependence shown in Fig. 3.5 is also incompatible with an inelastic phonon process, as phonon frequencies would not increase by 28%-48% between 2 K and 150 K.

3.5 Summary and Outlook

We have shown that resonant tunneling can be utilized to probe the subband spacings of 2DELs in $SrTiO_3$. This experiment has demonstrated its importance especially for 2DELs where the mobility is too low and the subband spacing too small to resolve a significant fraction of subbands via other techniques like quantum oscillations. The studies have also provided evidence of an inherent asymmetry of the 2DELs on either side of the barrier in complex oxides. The effect of carrier concentration and resulting confinement on the subband spacings has been demonstrated and confirmed the predictions of various theoretical models.

In the future, similar resonant tunneling studies might prove useful to study the effects of epitaxial strain and modulation of carrier density on the subband structure, and further advance the understanding of 2DELs in complex oxide heterostructures.

Chapter 4

Metal-Insulator Transition in $BaTiO_3$ Using Electrostatic Doping

4.1 Ferroelectricity and Metallicity in $BaTiO_3$

$BaTiO_3$ is a prototypical ferroelectric material, which produces a spontaneous and reversible polarization charge at its surface [21]. The spontaneous polarization originates from a local displacement of the Ti atom in the center towards the face center of the oxygen octahedra along one of the 8 possible <111> directions. Above the Curie temperature (T_C) of 120 °C, $BaTiO_3$ is in a cubic $Pm\bar{3}m$ phase and the Ti displacements are random, resulting in no net polarization across the sample. Below T_C, $BaTiO_3$ undergoes a phase transformation to tetragonal $P4mm$ phase and an ordering of Ti displacements resulting in a *net* polarization along the <001> direction, as shown schematically in Fig. 4.1 [35].

The local displacement of Ti in the $BaTiO_3$ crystal has also been associated with the large dopant concentration necessary for inducing an insulator to metal transition in the material [121]. Free carrier concentrations of up to at least 10^{20} cm^{-3} are required for display of nominally metallic behavior in single crystals and ceramics of $BaTiO_3$

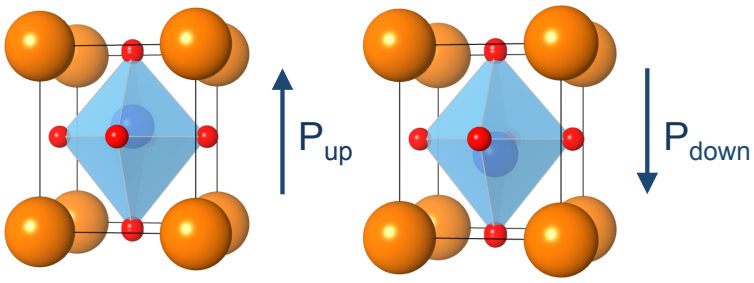

Figure 4.1: Illustration showing overall net displacement of the Ti atom with respect to the oxygen octahedra resulting in a spontaneous and reversible ferroelectric polarization in tetragonal $BaTiO_3$ along the [001] direction.

[122, 123, 121, 124]. In contrast, $SrTiO_3$ – which lacks the Ti displacement – requires only 10^{15} cm^{-3} carriers for undergoing insulator-to-metal transition [125].

The coexistence of metallicity and ferroelectricity in the same material has been a matter of fundamental interest and debate since the 1960s [126, 127, 128, 129, 130]. In ferroelectric materials like $BaTiO_3$, the Ti displacement is related to the TO phonon mode [131, 132]. In addition, the small displacements/distortions in such highly ionic compounds with strong Coulomb interactions leads to a large LO-TO splitting. Thus, ferroelectrics, in general, are understood to rely heavily on both – the unstable TO phonon mode *and* a large splitting in energy between the TO and LO phonon modes [61]. However, introduction of free carriers in the material would screen the long-range Coulomb interactions, resulting in loss of LO-TO splitting [133], and destabilizing ferroelectricity [134]. Therefore, it is important to understand what happens to carriers when they are introduced into a ferroelectric like $BaTiO_3$. Some recent studies claim coexistence of ferroelectricity and metallicity in $BaTiO_3$ [123], while others suggest they do so in separated regions [135]. This, combined with the above observation that a very high doping density is necessary for insulator-to-metal transition in ferroelectric single

crystals and ceramics [122, 121, 124], seems consistent with the picture that metallicity and ferroelectricity cannot easily coexist. To understand how free carriers and ferroelectric polarization interact with each other, most previous studies introduce carriers using chemical substitutional doping or by creating oxygen vacancies, thereby inducing large amounts of disorder. That would explain efforts to invoke disorder for promoting the insulating state [121, 124]. Furthermore, large concentrations of dopants also introduce significant lattice distortions which can also destabilize ferroelectricity.

To distinguish between the effects of chemical doping and structural distortions on ferroelectricity, and also to obtain an improved understanding of the nature of doped ferroelectrics, a method to introduce carriers without chemical doping (and associated structural effects) is necessary.

4.2 Electrostatic Doping of $BaTiO_3$

In Chapters 2 and 3, we have seen that a polar discontinuity at the interface between insulators RTiO$_3$ (R: trivalent rare earth element, like Sm or Gd) and SrTiO$_3$ electrostatically introduces a large sheet carrier density of $\sim 3\times10^{14}$ cm^{-2} into SrTiO$_3$ [33, 136]. This has been used to study the metal-to-insulator transition in that material [78, 119, 106, 137, 138, 139]. It has been shown that a substantial portion of carriers in these 2DELs are confined to the interface, in addition to other weakly confined carriers that spread away from the interface into SrTiO$_3$ [97, 98, 96, 87]. The conduction band alignment between RTiO$_3$ and SrTiO$_3$ [34] causes band bending in SrTiO$_3$ and prevents carriers from spreading into the RTiO$_3$. In this study, we replace the SmTiO$_3$/SrTiO$_3$ interface with SmTiO$_3$/BaTiO$_3$ interface and systematically increase the BaTiO$_3$ layer thickness, as shown in Fig. 4.2(a). The polar discontinuity at the SmTiO$_3$/BaTiO$_3$ in-

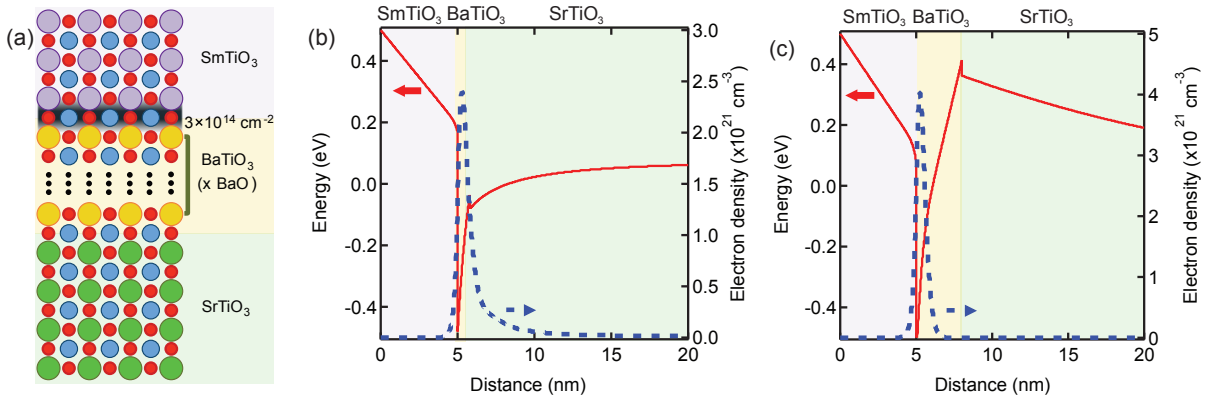

Figure 4.2: (a) Schematic of the heterostructure. The thickness of the $BaTiO_3$ layer is specified in terms of the number of BaO layers. The gray-shaded area indicates the 2DEL, which spreads into the $BaTiO_3/SrTiO_3$ layers. (b-c) Calculated conduction band profiles and 2DEL charge distributions for the $SmTiO_3/BaTiO_3/SrTiO_3$ heterostructures, with (b) two u.c. (3 BaO layers) of a paraelectric $BaTiO_3$ layer and (c) seven u.c. (8 BaO layers) of a ferroelectric $BaTiO_3$ layer. The calculations were performed with a one-dimensional Poisson-Schrdinger solver [7] using the parameters described in the text (Adapted with permission from [8]).

terface allows for introduction of carriers into $SmTiO_3/BaTiO_3/SrTiO_3$ heterostructure by purely electrostatic means, without any associated disorder.

To obtain a better understanding of the experiment, self-consistent Poisson-Schrödinger solver calculations were performed to confirm that, for paraelectric $BaTiO_3$, the resulting conduction band profile and charge distribution matches the case without any $BaTiO_3$ due to similar fixed polar charges, material properties and band offsets, as seen in Fig. 4.2(b). The thickness of $SmTiO_3$ and $SrTiO_3$ layers were 5 nm and 20 nm respectively. Band gaps and band alignments were taken from experimental data and first-principle calculations respectively [140, 34, 141]. A fixed interface charge of 3×10^{14} cm^{-2} (modeled as a 0.2 nm layer of fully ionized dopants) was used to describe the terminating SmO plane at the $SmTiO_3/BaTiO_3$ interface, along with an electron effective mass of 1 m_e (where m_e is the free electron mass) and a 6-fold degeneracy of the conduction band for $BaTiO_3$ and $SrTiO_3$. The relative dielectric constants (ϵ_r) of $SmTiO_3$, $BaTiO_3$, and

$SrTiO_3$ were 30, 60 and 300 respectively [142]. To model ferroelectricity in $BaTiO_3$, two 0.2 nm thick immobile sheet charges of opposite sign are introduced on either side of the ferroelectric layer, with charge density equal to the ferroelectric polarization. The polarity and the fixed polarization charge density were estimated to be 1×10^{14} cm^{-2} using capacitance-voltage (C-V) measurements on 10 nm $BaTiO_3$/60 nm La:$SrTiO_3$ heterostructures grown on $SrTiO_3$ substrates, described in detail in the subsequent sections.

4.3 Hybrid MBE Growth and Characterization of Ferroelectric $BaTiO_3$

The hybrid MBE technique developed for $SrTiO_3$ [54] was successfully extended to $BaTiO_3$. Ba was supplied using a standard effusion cell and Ti was supplied using TTIP metal organic precursor, as detailed in Chapter 1. The $BaTiO_3$ films were initially calibrated on $SrTiO_3$ substrates at 900 °C substrate temperature. The TTIP/Ba flux ratio was varied while keeping other parameters constant to optimize film stoichiometry. *In-situ* RHEED was used to monitor the growth kinetics of the film as well as post-growth surface quality. Fig. 4.3(a) shows the RHEED intensity profile as a function of time exhibiting oscillations in intensity that indicate a layer-by-layer growth mode for $BaTiO_3$. Previous studies have demonstrated that surface reconstructions on $SrTiO_3$ can be used to identify film stoichiometry and intrinsic material quality [9]. It has been shown that c(4×4) reconstruction along <110> azimuths indicate perfect stoichiometry for $SrTiO_3$ films. For $BaTiO_3$, stoichiometric films show similar c(4×4) reconstructions along both <110> and <100> azimuths, as seen in Fig. 4.3(b). Fig. 4.3(c) shows on-axis XRD scans of a 15 nm $BaTiO_3$ film grown using hybrid MBE technique on a $SrTiO_3$ substrate, with Laue thickness fringes for the $BaTiO_3$ film indicating high structural

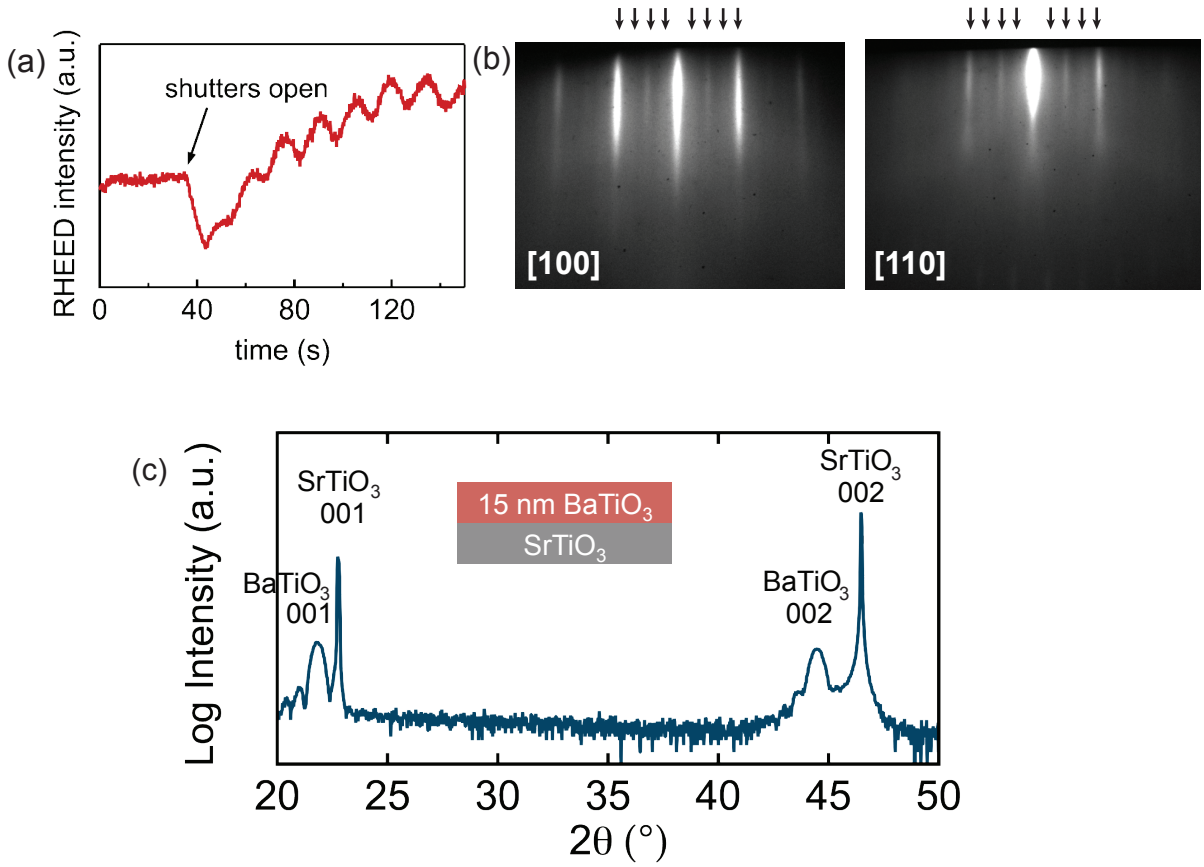

Figure 4.3: (a) RHEED intensity oscillations indicating layer-by-layer growth mode for $BaTiO_3$ on a $SrTiO_3$ substrate. (b) After growth RHEED patterns of $BaTiO_3$ surface along [100] and [110] azimuths. Arrows on top indicate the 4×4 surface reconstruction along both directions associated with perfect stoichiometry [9]. (c) On-axis XRD scan of a 15 nm $BaTiO_3$ film grown on a $SrTiO_3$ substrate.

quality and smooth interfaces.

A 5 nm $BaTiO_3$ thin film was grown on top of a 5 nm $SrTiO_3$/ 5 nm $SmTiO_3$/(001) LSAT heterostructure for studying the ferroelectric properties of the $BaTiO_3$ layer. Piezo-force microscopy (PFM) data for the sample is shown in Fig. 4.4. The 2DEL at the $SrTiO_3$/$SmTiO_3$ interface is used as the bottom electrode for the PFM measurement. Fig. 4.4(a-b) shows hysteresis in the phase and amplitude of the PFM signal, indicating ferroelectric switching. The asymmetry in the hysteresis is due to difference in the elec-

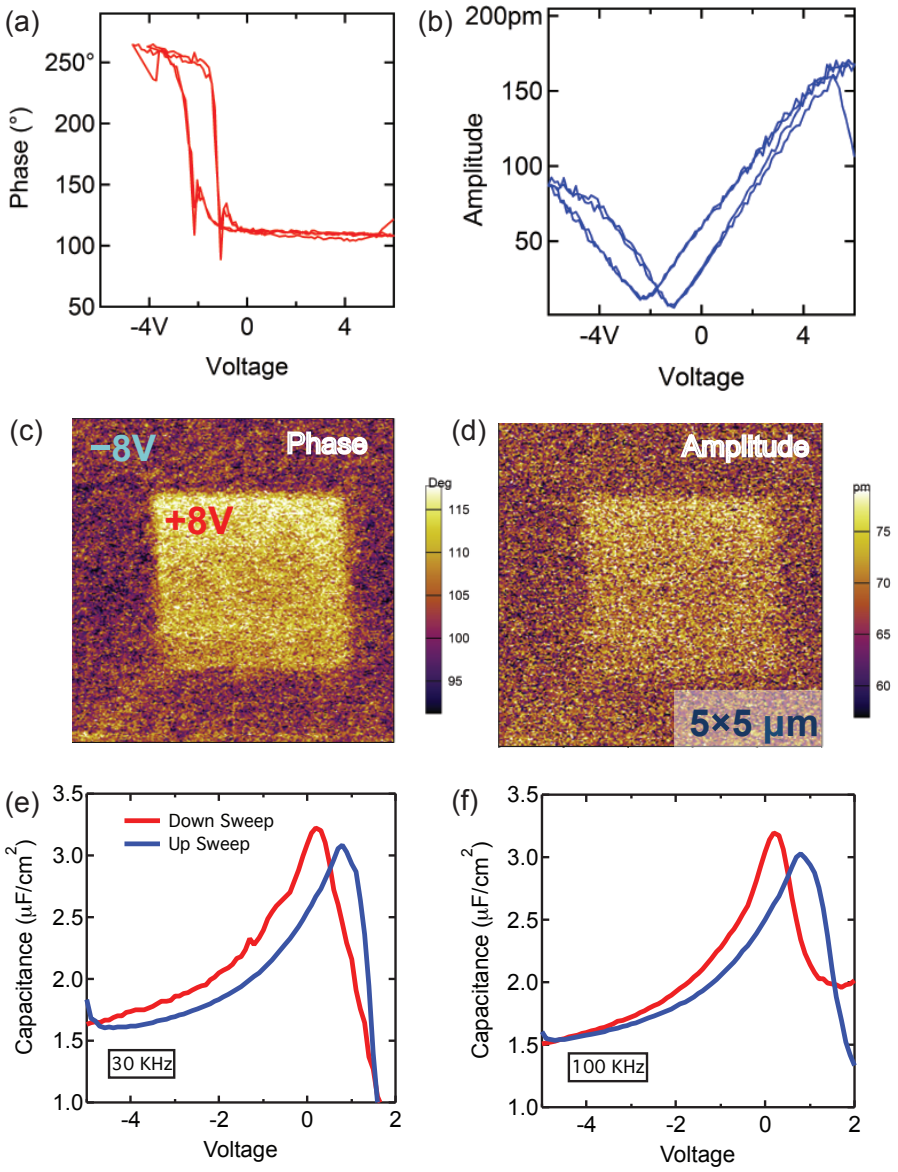

Figure 4.4: (a-b) Phase and amplitude signals from PFM scans on a 5 nm $BaTiO_3$ layer grown on 5 nm $SrTiO_3$/5 nm $SmTiO_3$. (c-d) Phase and amplitude signals showing retention characteristics of the two different polarization directions of the ferroelectric $BaTiO_3$. (e-f) Capacitance as a function of voltage for a 10 nm $BaTiO_3$ film on top of highly doped metallic $SrTiO_3$ (Adapted with permission from [8]).

trodes on either side of the ferroelectric. Fig. 4.4(c-d) shows the ferroelectric polarization retention. A negative bias (–8 V) was applied to the PFM tip to uniformly pole a 5×5 μm area, followed by uniformly scanning a smaller 3×3 area with a positive tip bias (+8 V).

The larger area is then again scanned for phase and amplitude in the two regions showing uniform differences for the two polarizations directions of the ferroelectric $BaTiO_3$.

To further confirm the ferroelectric properties of the $BaTiO_3$ films grown using hybrid MBE, C–V measurements were performed on 10 nm $BaTiO_3$ films on highly doped metallic $SrTiO_3$ layers. A two-probe configuration using Agilent 4294A Precision Impedance Analyzer was used to measure the C–V data. Pt Schottky contacts on the $BaTiO_3$ layer and Ti/Au Ohmic contacts on the doped $SrTiO_3$ were used. Fig. 4.4(e-f) shows hysteresis in the capacitance measured at 30 kHz and 100 kHz, indicating switching of the ferroelectric layer. The difference in the area under the C–V curves measured during the forward and reverse sweeps indicates the total charge displaced from the surface which should be equivalent to the ferroelectric polarization charge. The estimated polarization charge of 1×10^{14} cm^{-2} is close to the expected values from literature [143]. The direction of spontaneous ferroelectric polarization was estimated by the loss in sheet carrier density of the underlying La doped $SrTiO_3$ layer after deposition of the $BaTiO_3$ layer. $BaTiO_3$/La:$SrTiO_3$/$SrTiO_3$ (substrate) samples with low La doping in the $SrTiO_3$ layer became insulating after deposition of the $BaTiO_3$ layers, indicating depletion of carriers due to the spontaneous ferroelectric polarization that is pointed out-of-plane along the growth direction. The polarization direction and charge density measured in this experiment was used to model the direction of ferroelectric polarization in Fig. 4.2(c).

4.4 Results: $SmTiO_3/BaTiO_3/SrTiO_3$ Heterostructures

Following the confirmation of growth of high quality ferroelectric $BaTiO_3$ using hybrid MBE technique, $BaTiO_3$ layers with varying thickness were inserted in between $SmTiO_3$ and $SrTiO_3$ layers on (001) LSAT substrates. The thickness of $SmTiO_3$ and $SrTiO_3$ layers was kept constant at 5 nm and 10 nm respectively, and the $BaTiO_3$ thickness varied from 1/2 to 13 u.c.s. The thickness of $BaTiO_3$ layers are denoted by the number of BaO planes it contains (1 BaO = 1/2 u.c., 2 BaO = 1 u.c., and so on). Fig. 4.5(a) shows the oscillations in RHEED intensities with time indicating layer-by-layer growth mode that allowed precise thickness control. Streaky post-growth RHEED patterns of all the layers shown in Fig. 4.5(b) indicate atomically sharp interfaces between the different layers. *Ex-situ* on-axis XRD scans (Fig. 4.5(c)) of all samples showed only film and substrate reflections, and Laue thickness fringes for different layers indicating high quality epitaxy and smooth interfaces. The 20 nm $SrTiO_3$ layer in the heterostructures gives rise to closely spaced Laue fringes, along with widely spaced fringes from the 5 nm $SmTiO_3$ layer in all samples. For larger $BaTiO_3$ thicknesses, the peaks from $BaTiO_3$ interfere, and the resulting XRD pattern becomes more complex. A combination of RHEED oscillations, XRD, and HAADF STEM was used to confirm the thicknesses and structural quality of the heterostructures.

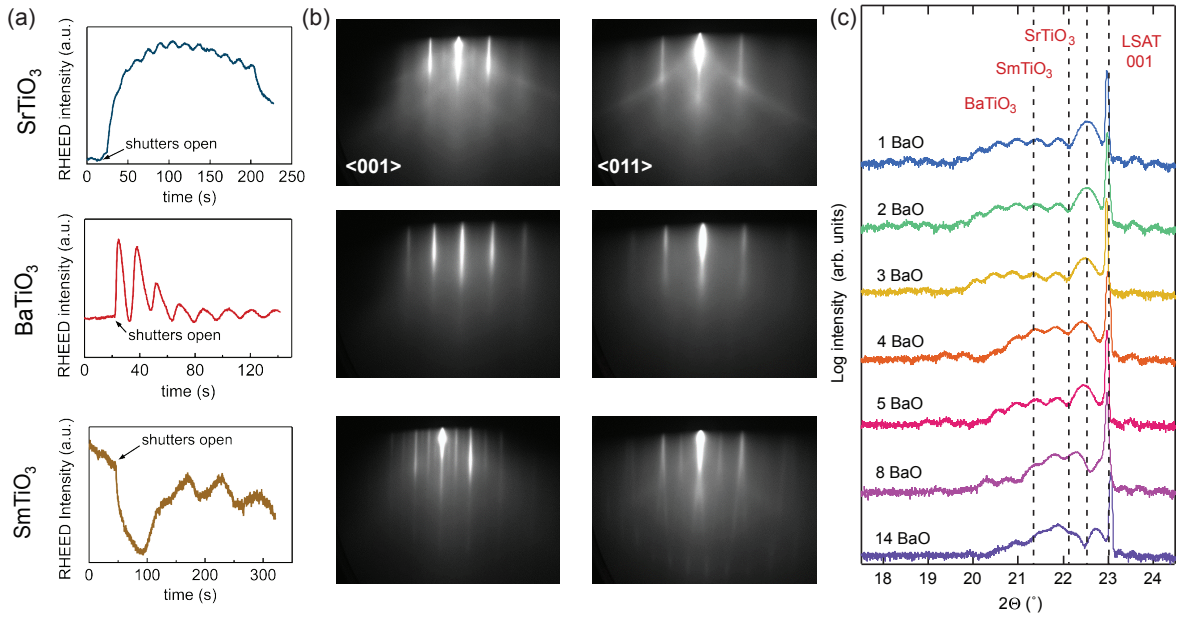

Figure 4.5: (a) RHEED intensities vs. time, and (b) RHEED patterns recorded after growth of the each layer along the 001 and 011 azimuths, respectively. (c) On-axis XRD patterns of the 5 nm $SmTiO_3$/x BaO($BaTiO_3$)/20 nm $SrTiO_3$/LSAT heterostructures. The dashed lines indicate the expected peak positions for individual layers coherently strained to a LSAT substrate (Adapted with permission from [8]).

4.5 Results: Transport in $SmTiO_3/BaTiO_3/SrTiO_3$ Heterostructures

Electrical transport measurements were conducted on the samples using Van der Pauw geometry and methods described in Chapter 1. The Hall voltage was found to be linear as a function of magnetic field up to ±9 T, similar to $R\mathrm{TiO_3}/\mathrm{SrTiO_3}$ interfaces [142, 144]. All samples showed 2D sheet carrier densities (n_{2D}) close to 3×10^{14} cm^{-2} at 300 K, independent of $BaTiO_3$ thickness, as shown in Fig. 4.6(c). This confirms that a 2DEL is formed at the $SmTiO_3/BaTiO_3$ interface from polar discontinuity, with the n_{2D} corresponding to the value that compensates the fixed polar charge at the interface. The n_{2D} is also seen to be almost independent of temperature for all films, except for some

thicker samples which will be discussed later. The sheet resistance of samples (R_{Sheet}) is shown in Fig. 4.6(b). The temperature dependence of R_{Sheet} for samples with $BaTiO_3$ thickness below 3 u.c. (4 BaO) layers indicates metallic behavior (defined as $\delta R_{Sheet}/\delta T > 0$) down to 2 K. Above 3 u.c., the sheet resistance of samples undergoes a dramatic increase, and shows $\delta R_{Sheet}/\delta T < 0$ for temperatures below 125 K.

Fig. 4.6(c) shows Hall mobility (μ_H) for samples as a function of temperature (T). For samples with $BaTiO_3$ thickness below 3 u.c., temperature dependance of μ_H is similar to that of RTiO$_3$/SrTiO$_3$ interfaces [66]. The mobility of 2DELs at RTiO$_3$/SrTiO$_3$ interfaces at low T is dominated by interface roughness scattering (μ_0), and at higher T by electron-electron scattering ($\mu^{-1} \sim T^2$) [66]. The $SmTiO_3/BaTiO_3/SrTiO_3$ interfaces in our experiment show a similar behavior only for $BaTiO_3$ thickness below 3 u.c. (4 BaO layers). This can be seen from fits to mobility in Fig. 4.6(c) as described by $\mu^{-1} = \mu_0^{-1} + \alpha T^2$. The fit values for α parameter (which describes strength of electron-electron scattering) was between 1.2 – 1.9 $\times$ V·s cm^{-2} K^{-2}, similar to that of RTiO$_3$/SrTiO$_3$ interfaces. LO phonon scattering, which limits mobility in $SrTiO_3$ at room temperature, is absent indicating screening of phonons by the large density of carriers. However, mobility for 3 u.c. $BaTiO_3$ (4 BaO layers) sample requires addition of temperature dependent LO phonon limited scattering (formulation described in Chapter 1) to obtain fits of comparable quality. The fit is described by $\mu^{-1} = \mu_0^{-1} + \alpha T^2 + \mu_{LO}^{-1}$, and shown in Fig. 4.6(c). In addition, the 4 BaO layer sample shows reduced μ_0 by a factor of 5. Samples with $BaTiO_3$ thicker than 4 BaO layers shows further drop in mobility to less than 10 cm^2/V·s. For these thicker samples (> 4 BaO layers), the low temperature mobility initially increases with increasing temperature (reminescent of polaron hopping [145]), before decreasing at higher temperatures. No attempts were made to fit the mobility dependance for $BaTiO_3$ samples thicker than 4 BaO layers.

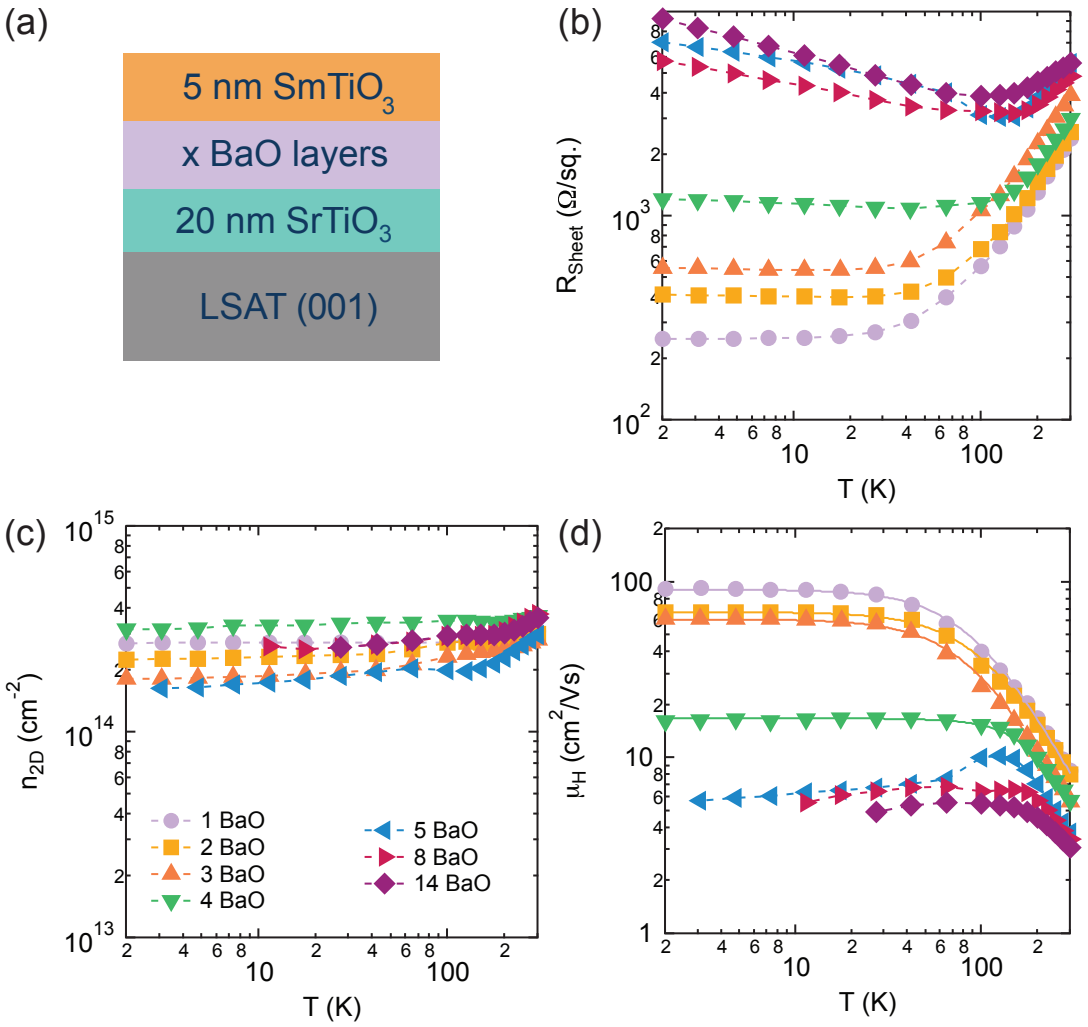

Figure 4.6: (a) Schematic of the structure indicating changing $BaTiO_3$ layer thickness. (b) Sheet resistance R_{Sheet}, (c) sheet carrier density n_{2D}, and (d) Hall mobility μ_H as a function of temperature T, for $SmTiO_3/BaTiO_3/SrTiO_3/(001)$ LSAT samples with different $BaTiO_3$ thicknesses (specified in number of BaO layers). The dashed lines are guides to the eye, and the solid lines in (d) are fits to the data. For the three thinnest $BaTiO_3$ structures, fits of form $\mu^{-1} = \mu_0^{-1} + \alpha T^2$ were used and resulted in (goodness-of-fit) χ-squared values of less than 0.006. Such fits yielded an increased χ^2 value for the four BaO sample (0.01). Including LO-phonon scattering ($\mu^{-1} = \mu_0^{-1} + \alpha T^2 + \mu_{LO}^{-1}$) reduced the χ^2 value to 0.003, and the average energy of the LO phonon obtained from the fit is 50 meV. The drop in the mobility at low temperatures for this sample is due to the low μ_0 (Adapted with permission from [8]).

4.6 Results: TEM of $SmTiO_3/BaTiO_3/SrTiO_3$ Heterostructures

HAADF-STEM was used to understand the relation between the local structure and the measured electrical properties in the $SmTiO_3/BaTiO_3/SrTiO_3$ heterostructures (courtesy of Jack Y. Zhang). Cross-section samples were prepared using focused ion beam thinning and imaged on a FEI Titan S/TEM operated at 300 kV with a 9.6 mrad convergence angle. The images shown in this Chapter consisted of 100 fast-scan images, which were acquired with a 3 μs dwell time and 512×512 pixels, and averaged using subpixel cross-correlation to reduce the effect of drift and scan distortions. Fig. 4.7(a) shows cross-section images of samples with nominally 8 BaO layers (left) and 3 BaO layers (right), respectively. The samples showed thickness variations of ±1 monolayer, associated with steps. However, the average number of BaO layer over the entire TEM sample matches the thickness calibrated using RHEED oscillations. The abrupt interface between $SrTiO_3$ and $BaTiO_3$ with clear atomic number (Z) contrast is visible. The interface between $BaTiO_3$ and $SmTiO_3$ has a smaller Z difference, and is located using *A*-site cation displacements in $SmTiO_3$ that are absent in $BaTiO_3$ [119]. The relative out-of-plane and in-plane lattice parameters of the $SrTiO_3$ and $BaTiO_3$ layers were measured from Fig. 4.7(a), normalized to $SrTiO_3$, and mapped / plotted in Fig. 4.7(b-c). The in-plane values are ~ 1.00 for both samples, consistent with coherently strained films. The out-of-plane lattice parameter for $BaTiO_3$ are all > 1.00. The 8 BaO layer sample shows a relative out-of-plane lattice parameter of ~ 1.057 in the interior (dashed lines in Fig. 4.7(c)), which matches the theoretically expected value for compressively strained, *c*-axis-oriented, tetragonal $BaTiO_3$. The out-of-plane values for the $BaTiO_3$ layers are reduced at the interfaces, and remain completely below the theoretically predicted value in the 3 BaO layer film, indicating reduced tetragonality.

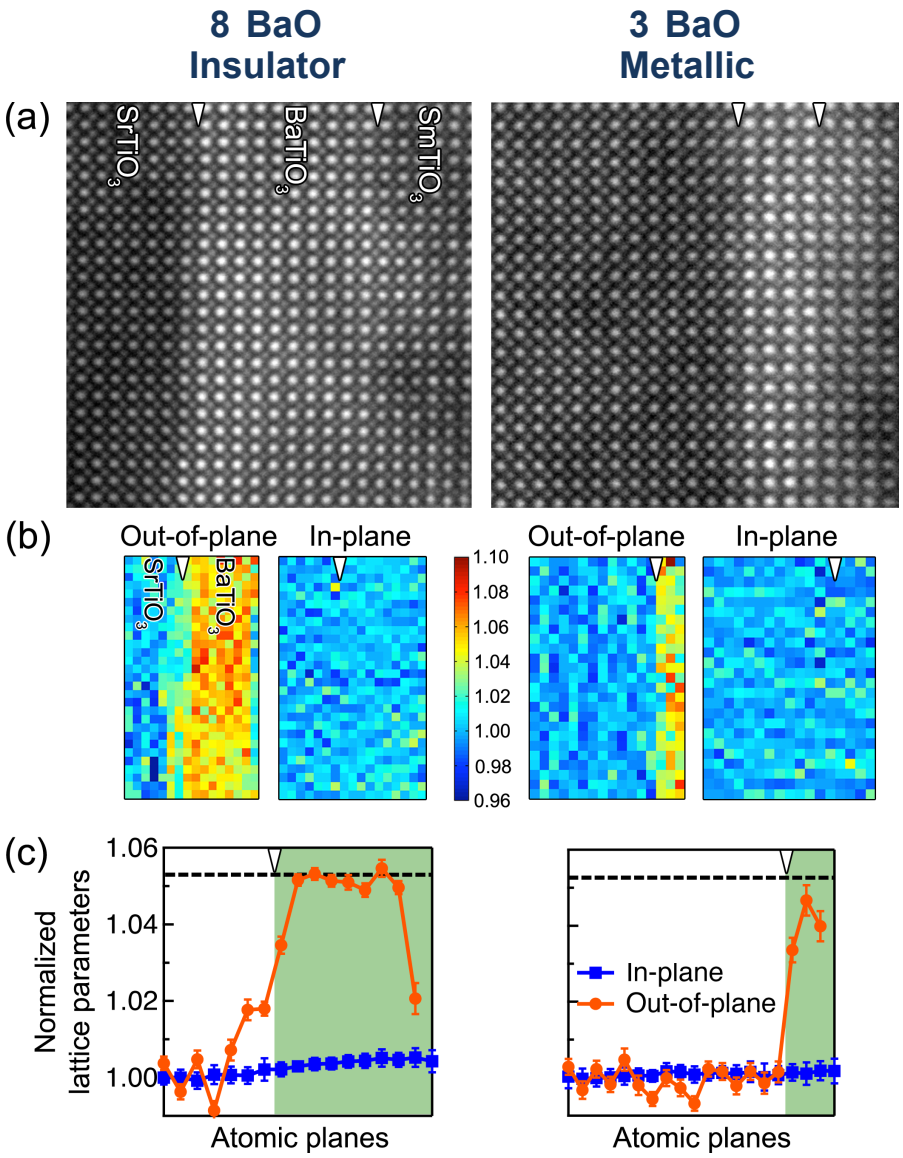

Figure 4.7: (a) HAADF STEM cross sections of eight BaO (left) and three BaO (right) thick layers of $BaTiO_3$. The $SrTiO_3$ and $SmTiO_3$ layers are to the left and right of the $BaTiO_3$, respectively. The arrows mark the approximate interface boundaries. (b) Maps of unit cell lattice parameters along the out-of-plane and in-plane directions, normalized to the lattice parameter of the three layers of $SrTiO_3$ farthest away from the $BaTiO_3$. Only $SrTiO_3$ and $BaTiO_3$ layers are mapped. (c) Averaged (parallel to the interface) in-plane (orange circle) and out-of-plane (blue square) lattice parameters from (b). The dashed lines indicate the theoretically expected value for compressively strained, c-axis oriented, tetragonal $BaTiO_3$ on a LSAT substrate (Reproduced here with permission from [8].)

4.7 Discussion: Metal-to-Insulator Transition

We have seen that all the $BaTiO_3$ layers in the $SmTiO_3/BaTiO_3/SrTiO_3$ heterostructures, independent of the film thickness, were electrostatically doped with 3×10^{14} cm^{-2} of free carriers from polar discontinuity with $SmTiO_3$. Samples show metallic behaviour and high carrier mobility at low temperatures that is consistent with band conduction only for extremely thin $BaTiO_3$ layers with thickness $\leq$ 2 u.c.s (or 3 BaO layers). HAADF-STEM images demonstrate that such thin layers are characterized by reduced tetragonality and mobility measurements indicating the absence of LO phonon scattering at high temperatures, which illustrates that these layers are *paraelectric* (i.e. not ferroelectric). "Dead layers "at the interfaces of ferroelectrics films have been a shown to be common [146, 147]. This is further demonstrated by reduced tetragonality of the interfacial unit cells in the HAADF-STEM images. The similar nature of transport characteristics for thin $BaTiO_3$ samples with that of $R TiO_3/SrTiO_3$ samples [66, 142], indicates that 2DEL at interfaces with *paraelectric* $BaTiO_3$ do not have fundamentally different properties. This combined with the lack of a significant conduction band offset between $BaTiO_3$ and $SrTiO_3$ [34] would signify that carriers from the 2DEL are spread across the $BaTiO_3/SrTiO_3$ interface for metallic samples.

$BaTiO_3$ films thicker than 4 BaO layers show an increased lattice distortion that is consistent with a tetragonal unit cell that is responsible for ferroelectricity. A definitive proof of ferroelectricity is measurement of polarization switching, which is not possible for such conductive layers used in this study. Nevertheless, the results suggest that macroscopic conditions exist that indicate presence of ferroelectricity in the thicker films, like tetragonal distortion and LO-phonon scattering in the 4 BaO sample. Hysteresis loops obtained using PFM and C-V measurements in control samples of $BaTiO_3$ films of compa-

rable thickness and grown by same method (as discussed in previous sections) corroborate presence of ferroelectricity. In addition, the transport properties of heterostructures with thicker $BaTiO_3$ films (> 4 BaO layers) indicate that carriers cease to spread into the $SrTiO_3$ layers, since the transport in this case does not show similar high-mobility and metallic behaviour. This can be explained by the presence of an internal ferroelectric polarization field in thicker $BaTiO_3$ films (> 4 BaO layers), which causes a change in the spatial distribution of the charge carriers in comparison to the *paraelectric* $BaTiO_3$ case (Fig. 4.2(b)). Calculations for ferroelectric $BaTiO_3$ shown in Fig. 4.2(c) indicate that carriers are tightly confined within the $BaTiO_3$ layer near the interface with $SmTiO_3$ when a ferroelectric polarization is present. The decrease in the low-temperature limit of mobility (μ_0) for the 4 BaO layer sample could be explained by this restribution of 2DEL carriers located far inside $SrTiO_3$ to the $SmTiO_3/BaTiO_3$ interface (with increased interface roughness scattering), at the onset of ferroelectricity.

The poor mobilities (1–10 $cm^2/V{\cdot}s$) of carriers in ferroelectric samples with thick $BaTiO_3$ (> 4 BaO layers) are consistent with self-trapping of carriers. Such a transport mechanism is also known as strong-coupling polarons [148]. It can be noted that in thicker films, at low temperatures, the mobility increases initially with increasing temperature. This is clearly not described by the temperature independent disorder-limited scattering term μ_0. In addition, the samples show insulating properties in this regime ($\delta R_{Sheet}/\delta T < 0$), despite the fact that sheet resistances are below the Mott-Ioffe-Regel limit of $\sim 25^4$ $k\Omega/\square$ when strong localization is expected to occur [149]. The low mobilities are similar to those of doped, single crystal $BaTiO_3$ [150]. The poor conduction seems to be a general feature of ferroelectric $BaTiO_3$, and is reminiscent of transport that is typical for polarons, independent of how carriers are introduced (chemical vs electrostatic doping, or the degree and type of disorder). The temperature dependance of transport

characteristics of self-trapped carriers (or polarons) can be complicated [145], and often fail to describe transport in real materials [151].

4.8 Conclusions and Outlook

In summary, we have shown that the appearance of ferroelectricity coincides with the transition of $BaTiO_3$ from a high-mobility, metallic state to an insulating state with low-mobility and high-resistance, at low temperatures. In this experiment, the change between from metallic to insulating state was observed while keeping other parameters constant (like sheet carrier density), reflecting the intrinsic interactions between free (mobile) charge carriers and the ferroelectric polarization across the transition. The ferroelectric film does not allow for free mobile charge carriers, pushing them out of the bulk towards the interface, where they conduct with low mobility. The temperature dependance of mobility in the ferroelectric insulating state is consistent with self-trapping (polaron hopping) mechanism.

The metal-to-insulator transition demonstrated in this study is similar to the Mott-type transition, since it occurs when the long-range Coulomb interactions are insufficiently screened. With respect to the question of coexistence between metallic and ferroelectric state, it appears that the two states can coexist but not in the conventional, metallic conduction within the bulk of the ferroelectric. Finally, this study has illustrated that electrostatic doping from polar discontinuity can be a useful technique to introduce large concentrations of carriers without any associated disorder, and may provide insight in studying other intrinsic aspects of polaron transport for which a quantitative understanding is often missing.

Chapter 5

MBE Growth of Perovskite Stannate Thin Films

5.1 Introduction

New device paradigms like negative capacitance [152] and charge amplification [153] can be enabled using functional perovskite oxides, but their poor charge carrier mobilities have been a major challenge. Most oxides like $SrTiO_3$ have mobilities no better than 1–10 $cm^2/V{\cdot}s$ at room temperature [66]. The charge carrier mobility limits performance metric or figure of merit for almost every electronic device application. As discussed in Chapter 1, the demonstration of mobilities as high as 300 $cm^2/V{\cdot}s$ in single crystals of La doped $BaSnO_3$ [13] has motivated research on growth of high-quality thin films, with low defect densities, for transparent conducting applications and power electronics. Fig. 5.1 shows highest achieved conductivity (as a function of carrier concentration and mobility) for various semiconductors and metals. It can be seen that the conductivity values of the La-doped $BaSnO_3$ single crystals are as high as 10^4 $\Omega^{-1}cm^{-1}$, which is the industry-standard for widely used transparent conductor indium-tin oxide ($In_{2-x}Sn_xO_3$). In comparison, other perovskite oxides are either limited by low mobility (like $SrTiO_3$) or they are metals where the carrier concentration cannot be controlled (like $SrVO_3$). In

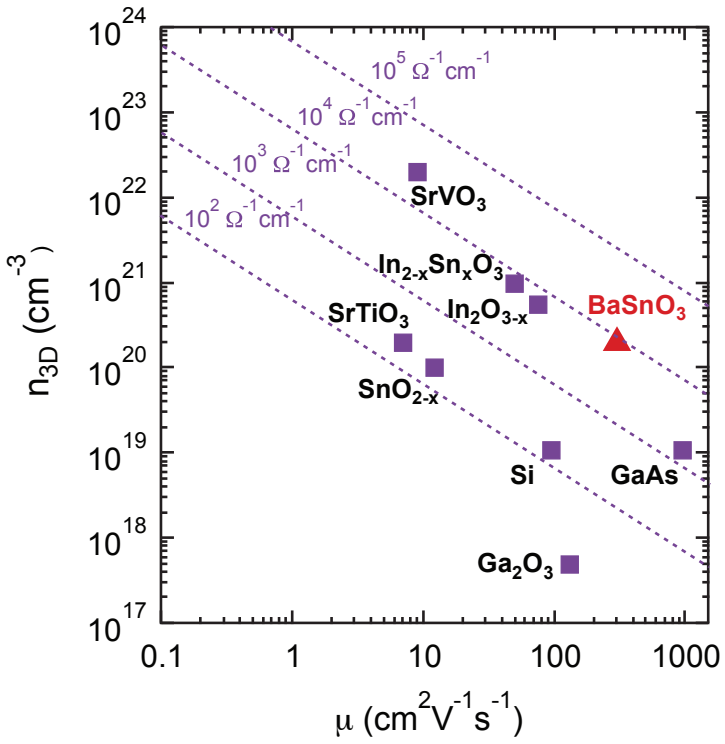

Figure 5.1: Carrier density and electron mobility values for various metals and semiconductors. Constant conductivity contours are shown as straight lines. [Adapted with permission from [10]]

addition, for the first time, $BaSnO_3$ thin films would allow for integration of other functional perovskite oxides (like ferroelectrics or strongly correlated materials) on a lattice- and symmetry-matched, high-mobility semiconductor [154].

Band-gap engineering between $BaSnO_3$ and other functional oxides would allow for its use as a high-mobility channel, if conduction band-offsets promote charge transfer into $BaSnO_3$, as predicted[34]. Similar to $BaSnO_3$, $SrSnO_3$ is also predicted to be a wide band-gap semiconductor with a low effective mass and high carrier mobility. High-mobility films and a range of band gaps are needed for band-engineering high performance electronic devices. The band gap and lattice parameters can be tuned by alloying $SrSnO_3$ and $BaSnO_3$, thus presenting opportunities for growth of lattice-matched films on differ-

ent substrates, strain engineering, and tuning of heterojunction band offsets in this class of materials.

In this Chapter, we present growth and structural data on high quality $BaSnO_3$, $SrSnO_3$, and $Ba_xSr_{1-x}SnO_3$ thin films using oxide molecular beam epitaxy.

5.2 Challenges

Most $BaSnO_3$ thin films in literature have been grown using high-energetic deposition techniques, like sputtering [14] and pulsed laser deposition [13, 155, 3, 15], and mobilities have lagged far behind single crystals. The highest reported mobilities were around 80 $cm^2/V{\cdot}s$ [13]. In this study, we utilize molecular beam epitaxy (MBE) – a low-energetic deposition technique – to obtain high quality $BaSnO_3$ films. However, control of stoichiometry in MBE of perovskite oxides can be challenging [51]. In particular, for Sn-based oxides, the formation of volatile SnO is a known issue. Sn is known to have a low oxidation potential [156]. Sn can be oxidized to form SnO (Sn^{+2}) or SnO_2 (Sn^{+4}). Insufficient oxidation of Sn has demonstrated growth regimes where volatile SnO desorbs from the film, leaving behind Sn metal droplets [157].

Another challenge with growth of high quality $BaSnO_3$ films is the lack of lattice matched substrates, as discussed in Chapter 1. Most commercially available substrates have large mismatch. In this Chapter, we will discuss growths on $SrTiO_3$ and $PrScO_3$ substrates, with lattice mismatch of –5.4% and –2.18% respectively.

5.3 Approach: Plasma Assisted Oxidation of Sn Metal

Conventional oxide MBE uses evaporation of high-purity metals to supply cations, provided that they have sufficient vapor pressure for reasonable growth rates. All metals in $BaSnO_3$ and $SrSnO_3$ have sufficient vapor pressures for MBE. Sn metal is a low melting solid (m.p. 232 °C) and beam equivalent pressures of 4×10^{-8} Torr can be obtained from an effusion cell operating at 1160 °C. This is sufficient to obtain reasonable growth rates. In this approach, we evaporate high-purity Ba, Sr and Sn metals (4N, Sigma Aldrich) using solid source effusion cells and an oxygen plasma source (RF power 300 W) is used to provide activated oxygen. La is co-evaporated from an effusion cell for doping. All substrates were first subjected to a 20 min oxygen plasma anneal at growth temperature before growths, to obtain a clean film/substrate interface. The substrate temperature was monitored using an infrared pyrometer (Ircon modline-3). The oxygen plasma with a BEP of 1×10^{-5} Torr was maintained during the growth, and samples were cooled under the same plasma conditions after growth. Fluxes for Sr, Ba, and Sn were calibrated using a beam flux monitor. Normally, the Sr (Ba) BEP was kept constant and Sn flux was adjusted. Stoichiometric conditions were found by changing relative cation flux ratios, while keeping oxygen plasma conditions constant, in combination with *in-situ* monitoring of RHEED and *ex-situ* high-resolution XRD.

Fig. 5.2(a) shows RHEED patterns of $SrSnO_3$ films grown on a (001) $SrTiO_3$ substrate, at a substrate temperature of 550 °C, using elemental Sr and Sn metal sources and oxygen plasma. XRD of films grown using this approach were used to identify growth regimes that resulted in single-phase perovskite $SrSnO_3$ (Fig. 5.2(b)). However, it was noted that the RHEED pattern from the substrate completely disappeared as soon as the Sr, Sn, and oxygen plasma shutters were opened. The RHEED pattern reappears

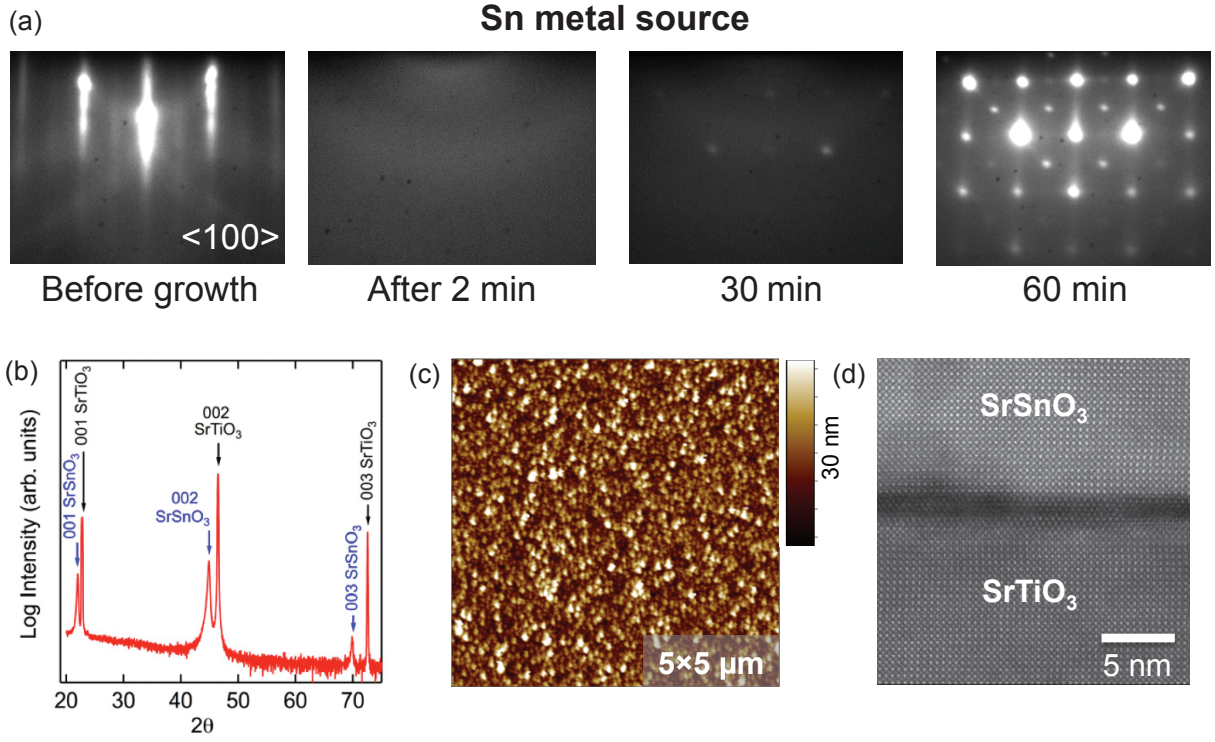

Figure 5.2: (a) RHEED pattern obtained during growth of $SrSnO_3$ on a $SrTiO_3$ substrate at a substrate temperature of 550 °C, using a Sn metal source. (b) On-axis XRD scan showing single phase film, (c) AFM image indicating film surface morphology, and (d) cross-section HAADF-STEM image showing a defective interface for the $SrSnO_3$ film grown on $SrTiO_3$ substrate. [Adapted with permission from [11].]

during growth after $\sim$ 30 min, but remains spotty until the end of growth (after 60 min), indicating three-dimentional growth (also confirmed by AFM as shown in Fig. 5.2(c)). The disapperance of RHEED at the start of the growth is explained by formation of Sn metal droplets on the substrate that are not oxidized. The issue of Sn metal droplets in MBE of SnO_2 films from a Sn metal source has been well documented [158]. These droplets indicate formation of volatile SnO that consumes all activated oxygen in the growth environment, leaving behind metallic Sn on the surface [158]. TEM cross-section images of films grown using this technique (Fig. 5.2(d)) show a defective interface layer which is likely a result of Sn metal droplets. To avoid SnO formation and desorption, either oxygen partial pressure or the concentration of activated oxygen (using higher RF

power or ozone) must be increased. However, such an increase would risk oxidation of filaments and gauges in the MBE system, as well as oxidation of Ta backing metal used to heat up the substrates. Appendix A shows an approach used to avoid this problem by replacing Ta backing metal with Mo, which was found to be more oxygen resistant. In addition, more importantly, the growth of high quality perovskite films requires high substrate temperatures ($\sim$ 800–900 °C) to achieve sufficient ad-atom mobility. Growths performed at higher substrate temperatures (above 550 °C) prevented Sn metal droplet formation, but increased evaporation (and reduced incorporation) of Sn from (into) the film, similar to what has been observed for SnO_2 growths [157, 158]. Above 600 °C, no Sn incorporation was observed in the films using Sn metal source, and only SrO was deposited. This necessitates a different approach to achieve oxidation of Sn. A more detailed discussion of various growth conditions and resulting films using the Sn metal approach is illustrated in Appendix B.

5.4 Approach: Growths using Metal Organic Precursor

We have seen that using metal organic precursors like titanium tetra-isopropoxide (TTIP) and zirconium tert-butoxide (ZTB) for supplying pre-oxidized cations can be a highly successful approach for growth of high quality perovskite titanate and zirconate films. An attempt was made to extend this approach to perovskite stannates. However, unlike other precursors, SnTB is a solid at room temperature. Literature results on this precursor indicated sufficient vapor pressures (in the same range as TTIP and ZTB) for hybrid molecular beam epitaxy [159, 160, 161].

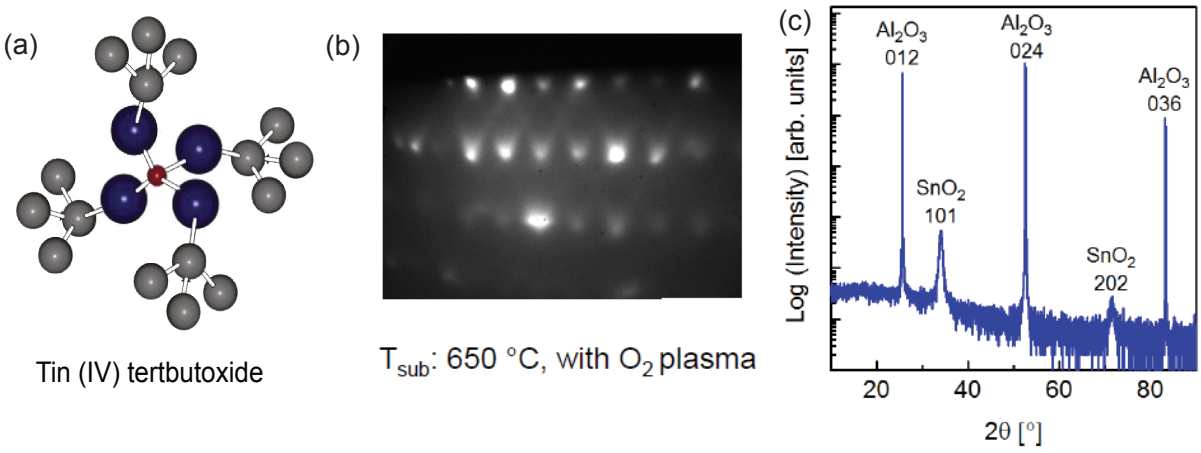

Figure 5.3: (a) Chemical formula unit of tin(IV) tert-butoxide precursor. (b) Post growth RHEED pattern and (c) on-axis XRD scan for a very thin film of SnO_2 grown on a r-plane sapphire substrate after 1 hour of growth.

High purity tin (IV) tert-butoxide (SnTB) (4N, Strem Chemicals, chemical formula shown in Fig. 5.3(a)) was obtained in a cylinder sealed with an overpressure of Argon and connected to heated metal-organic lines that were used to supply MO precursors through a low temperature gas source. The gas source was operated at 120 °C, and the line temperatures were kept between 90–110 °C, values similar to that of TTIP and ZTB. Numerous attempts were made to supply undecomposed SnTB vapor to a heated r-plane sapphire substrate. SnTB was found to be highly unstable and mostly decomposed in the bubbler into SnO_2 and other organic byproducts before being delivered to the gas source/chamber. Very thin layers of SnO_2 were seen to be deposited on heated r-plane sapphire substrates (T_{sub}= 650 °C) using RHEED and XRD, as shown in Fig. 5.3(b-c). Thus, an alternative method for supplying and oxidizing Sn was found to be necessary.

5.5 Approach: Plasma Assisted Oxidation of SnO_x

In order to address the issues related to Sn metal evaporation and unstable SnTB precursors, a modified MBE approach was adopted, namely, supplying pre-oxidized Sn

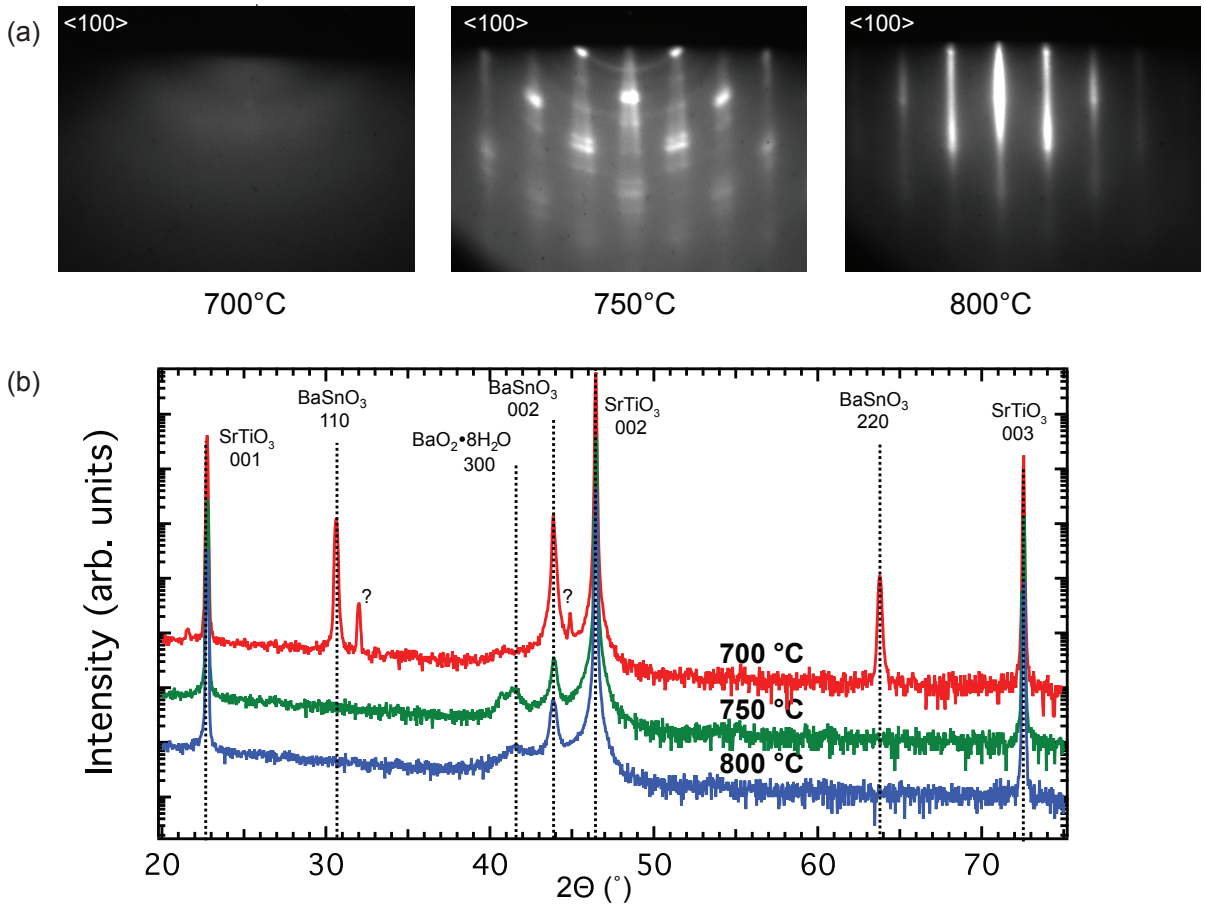

Figure 5.4: (a) Post-growth RHEED patterns, and (b) on-axis XRD scan of $BaSnO_3$ films grown using SnO_2 source at different substrate temperatures.

from a SnO_2 powder source. Not many studies in oxide MBE literature have focused on evaporation of a metal oxide from an effusion cell [162, 163, 164, 165, 166]. Results from vapor pressure experiments and calculations indicate that SnO_2 sublimes in the form of volatile suboxides (SnO_x) with sufficient vapor pressures for reasonable flux rates ($\sim 10^{-5}$ Torr) at practically feasible effusion cell temperatures (1300 °C) [167]. Co-deposition of SnO_2 and Ba at different SnO_2/Ba flux ratios on (001) $SrTiO_3$ substrates was performed at various substrate temperatures (700–800 °C), along with activated oxygen from oxygen plasma (RF power: 300 W, BEP: 1×10^{-5} Torr).

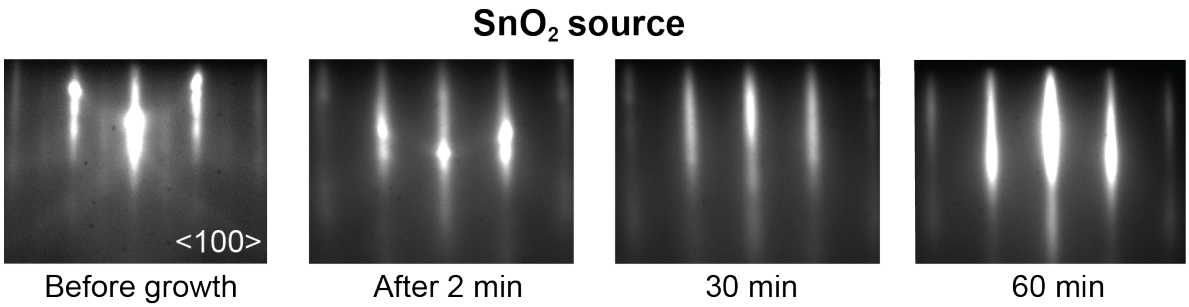

Figure 5.5: (a) Evolution of RHEED pattern of the $BaSnO_3$ film grown using a SnO_2 source at 800 °C substrate temperature, indicating a streaky pattern throughout the growth. [Adapted with permission from [11].]

RHEED patterns (Fig. 5.4(a)) obtained during growth indicated growth of amorphous films (with diffuse RHEED) at substrate temperatures around 700 °C. Films grown at substrate temperatures $\geq$ 750 °C showed streaks and spots indicating formation of crystalline phases. *Ex-situ* XRD data on films grown at 700 °C indicated presence of $BaSnO_3$ phases along multiple orientations (001 and 110), as seen in Fig. 5.4(b). Films grown at higher substrate temperatures of 800 °C showed streaky RHEED patterns throughout the growth, as shown in Fig. 5.5. Streaky RHEED from the start of the growth and no significant decrease in intensity indicates that the resulting $BaSnO_3$ film surface remains smooth. Supplying pre-oxidized Sn in the form of SnO_x in the presence of activated oxygen from a plasma thus allowed sufficient oxidation of Sn to Sn^{+4} and avoided the Sn droplet regime.

Stoichiometry conditions were found using a combination of RHEED and XRD, and shown in Fig. 5.6. Highly Sn-rich $BaSnO_3$ films showed spotty RHEED patterns. How-

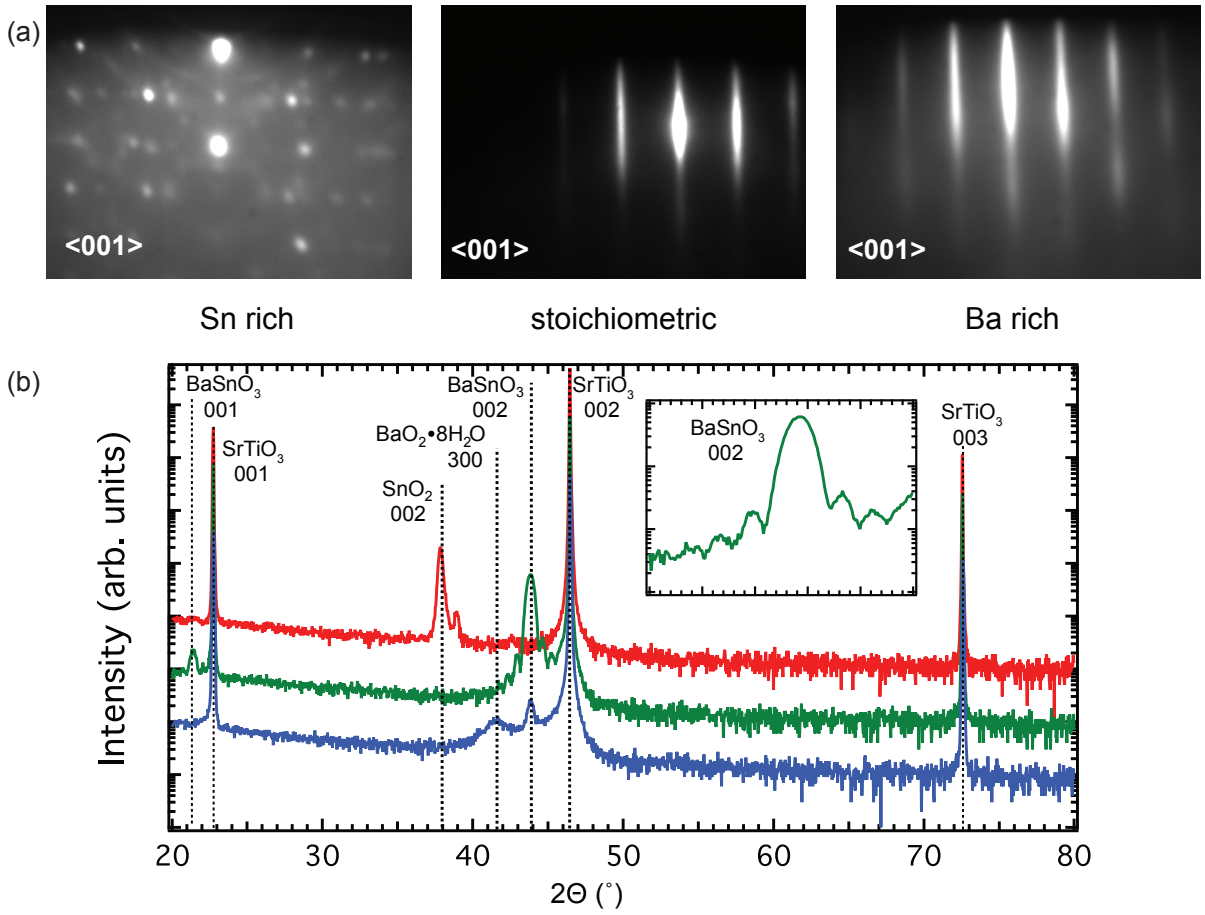

Figure 5.6: (a) Post-growth RHEED patterns, and (b) on-axis XRD scan of $BaSnO_3$ films grown at different SnO_2/Ba flux ratios for stoichiometry calibrations.

ever, both stoichiometric and Ba-rich regimes showed smooth streaks, and were indistinguishable in RHEED as seen in Fig. 5.6(a). Highly Sn-rich and Ba-rich films showed peaks in XRD associated with excess SnO_2 and $BaO.8H_2O$ respectively as seen in Fig. 5.6(b). For Ba-rich films, deposition of excess BaO is expected, which is highly hygroscopic and reacts with water when exposed to the atmosphere. Finally, it should be noted that this modified approach has allowed for perovskite film growth at high substrate temperatures ($\sim$ 800–900 °C) necessary for sufficient ad-atom mobility for improved stoichiometry and smooth high-quality films.

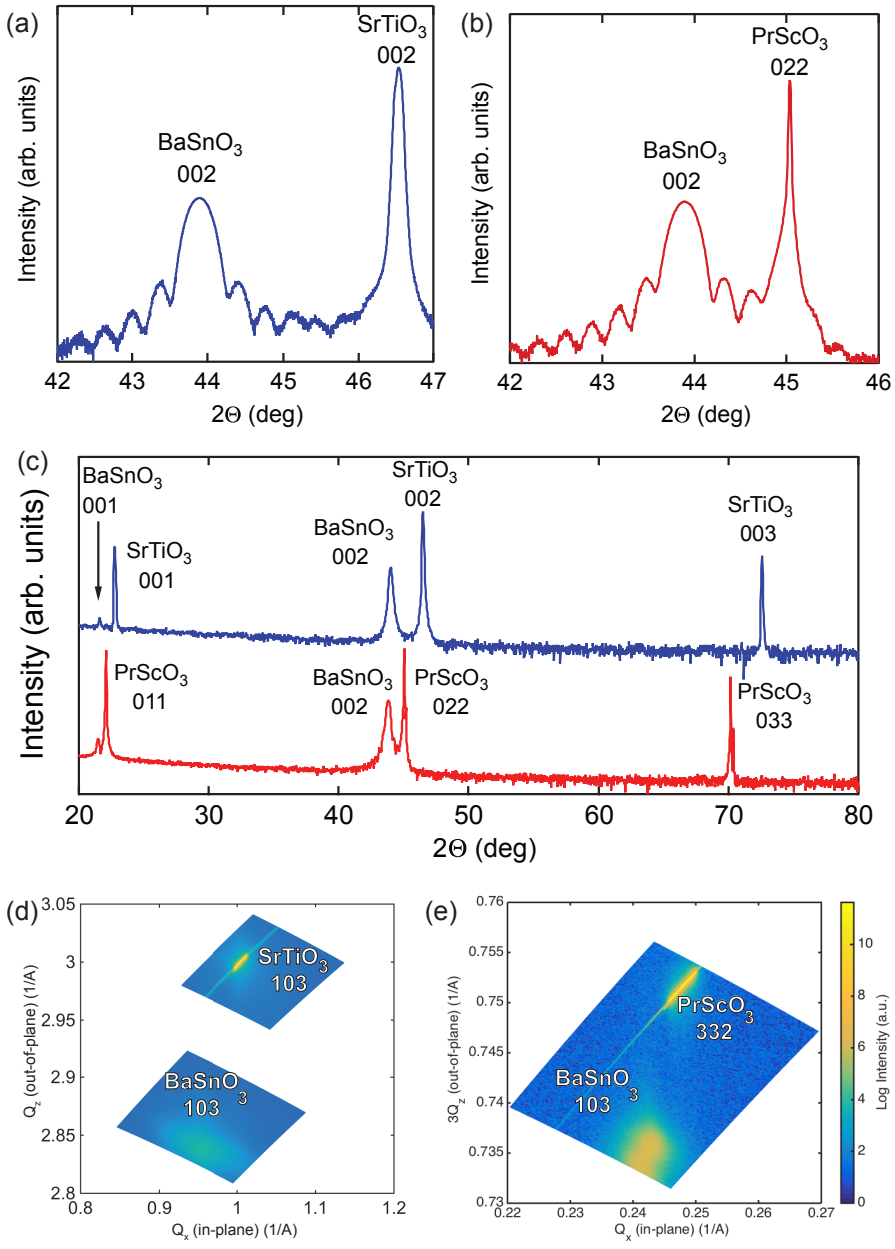

Figure 5.7: High resolution on-axis XRD scan around 002 peak of $BaSnO_3$ films grown on (a) (001) $SrTiO_3$ and (b) (011) $PrScO_3$ substrates. (c) Wide angle XRD scan of films showing growth of single-phase $BaSnO_3$. RSM images around the 103 asymmetric peak of $BaSnO_3$ film grown on (d) $SrTiO_3$ and (e) $PrScO_3$ substrates.[Adapted with permission from [11].]

5.6 Results: Structural Quality of $BaSnO_3$

Fig. 5.7 shows structural data for $BaSnO_3$ films grown on (001) $SrTiO_3$ and (110) $PrScO_3$ substrates, using the SnO_2 source. Fig. 5.7(a-b) shows on-axis XRD spectrum around the 002 peak of a 30 nm $BaSnO_3$ film on (001) $SrTiO_3$ and (110) $PrScO_3$. Wide-range x-ray scans (Fig. 5.7(c)) show only $BaSnO_3$ and substrate peaks under stoichiometric growth conditions. Laue thickness fringes are visible, indicating smooth interfaces and high structural quality. The out-of-plane lattice parameters for films were measured using high-resolution scans. $BaSnO_3$ films showed out-of-plane lattice parameter of 4.118 Å on $SrTiO_3$, and 4.117 Å on $PrScO_3$ substrates, respectively. This value is close to the bulk value of 4.116 Å, and indicating a stoichiometric and fully relaxed film, as expected due to the large lattice mismatch. A reciprocal space map (RSM) around the asymmetric 103 peak of $BaSnO_3$ is shown in Fig. 5.7(d-e). The in-plane lattice parameter of the film on $PrScO_3$ is 4.102 Å, slightly smaller than the bulk value, indicating a small residual in-plane strain (–0.3%) and an almost fully relaxed film. The $BaSnO_3$ film on $SrTiO_3$ had same in-plane and out-of-plane values, indicating a fully relaxed film.

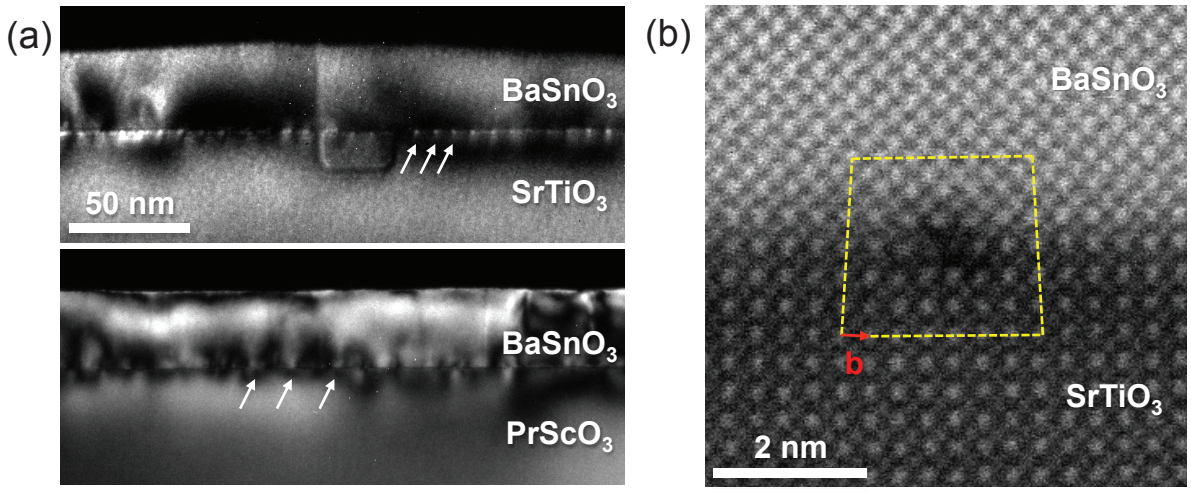

Figure 5.8: (a) Cross section dark-field TEM images of $BaSnO_3$ on $SrTiO_3$ (top) and $PrScO_3$ (bottom), showing misfit dislocations (white arrows). (b) HAADF-STEM image of a misfit dislocation at the $BaSnO_3/SrTiO_3$ interface with a Burgers circuit identifying the Burgers vector as $\vec{a}[100]$. [Adapted with permission from [11].]

Fig. 5.8 shows HAADF-STEM and diffraction contrast dark-field TEM images from cross-section samples (courtesy of Honggyu Kim and Jack Y. Zhang). Periodic misfit dislocations are visible at the interface between film and substrate in both cases (marked with white arrows in Fig. 5.8(a)). The spacing between the misfit dislocations is ~ 8 nm on $SrTiO_3$, which is the expected value for a fully relaxed film. The spacing between dislocations on $PrScO_3$ is between 20 and 30 nm, which is consistent with a partially relaxed film. The Burgers circuit around the misfit dislocation at the $BaSnO_3/SrTiO_3$ interface is shown in Fig. 5.8(b).

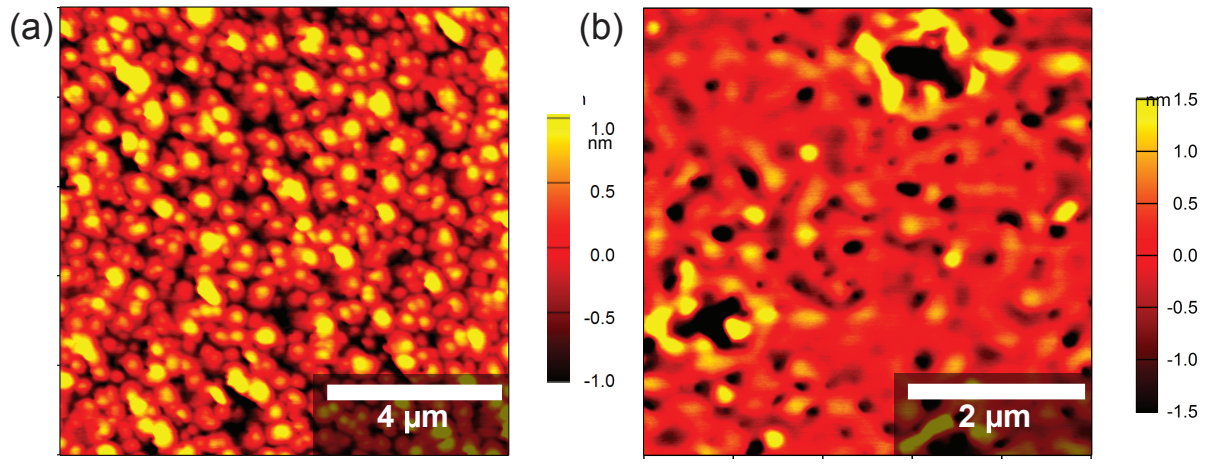

Figure 5.9: AFM images showing surface morphology of $BaSnO_3$ films grown on (a) $SrTiO_3$ and (b) $PrScO_3$ substrates.

Atomic force microscopy was used to study the surface morphology of the $BaSnO_3$ films. Fig. 5.9 shows AFM scans of $BaSnO_3$ films grown on (a) $SrTiO_3$, and (b) $PrScO_3$ substrates, respectively. A rather smooth interface with low roughness is seen. However, no atomically flat steps were observed at these surfaces.

5.7 Results: Structural Quality of $SrSnO_3$ and $Ba_xSr_{1-x}SnO_3$ Thin Films

Unlike $BaSnO_3$, $SrSnO_3$ has commercially available lattice matched substrates (as seen in Fig. 1.4). Here, we utilize $SrTiO_3$ and $PrScO_3$ (with a lattice mismatch of –3.3% and –0.27%) as substrates for $SrSnO_3$ calibration and growth. The MBE growth conditions of $BaSnO_3$ were extended to $SrSnO_3$ by changing SnO_2/Sr flux ratios to find stoichiometric growth conditions. For $Ba_xSr_{1-x}SnO_3$ thin films, the SnO_2 flux was kept constant at $\sim 1.5\times10^{-6}$ Torr, and the (Ba+Sr) flux to $\sim 5\times10^{-8}$ Torr. The SnO_2/(Ba+Sr) ratio was varied to optimize film stoichiometry.

$SrSnO_3$ has an orthorhombic crystal structure, with a pseudocubic lattice parameter a_{pc} of 4.034 Å[168]. $SrSnO_3$ films were grown on (001) $SrTiO_3$ and closely lattice matched (110) $PrScO_3$ substrates. Fig. 5.10(a-b) shows high resolution XRD scans around 002_{pc} reflections. Pronounced thickness fringes are observed for $SrSnO_3$ on $PrScO_3$, compared to $SrTiO_3$, consistent with a coherently strained film with smooth interfaces/surfaces. (S)TEM images (courtesy of Honggyu Kim) are shown in Fig.5.11. Periodic misfit dislocations are observed at the $SrSnO_3$/$SrTiO_3$ interface, as expected. No misfit dislocations were observed at the $SrSnO_3$/$PrScO_3$ interface, consistent with a coherently strained film. RSM images around the 103_{pc} reflection were used to determine the in-plane and out-of-plane lattice parameters for all $Ba_xSr_{1-x}SnO_3$ thin films (courtesy of Timo Schumann). Fig. 5.10(c) shows RSM image of $SrSnO_3$ film peak and $PrScO_3$ substrate peak, where the in-plane reciprocal lattice vectors of film and substrate align, indicating that the film is fully strained. The $SrSnO_3$ film on $SrTiO_3$ substrate is found to be mostly relaxed, with a small residual compressive strain (–0.4%), as seen in Fig. 5.10(d).

Fig. 5.10(b) shows on-axis XRD scans of $Ba_xSr_{1-x}SnO_3$ thin films grown at different alloying compositions. The peak value shifts to lower angles with increasing Ba content (x), which is expected due to larger lattice parameter of $BaSnO_3$ (4.116 Å). RSM of the remaining $Ba_xSr_{1-x}SnO_3$ thin films was used to determine the in-plane (a_{ip}) and out-of-plane (a_{oop}) lattice parameters, and the unstrained lattice parameter was calculated as a function of composition [169]:

$$a_0 = \frac{a_{oop} + 2\frac{c_{12}}{c_{11}}a_{ip}}{1 + 2\frac{c_{12}}{c_{11}}} \tag{5.1}$$

where c_{11} and c_{12} are the film elastic constans and $c_{12}/c_{11} \sim 0.24$ [170, 171]. a_0 is 4.041 ± 0.002 Å on $PrScO_3$ and 4.039 ± 0.006 Å on $SrTiO_3$, in agreement with bulk $SrSnO_3$. Errors in a_0 and composition were estimated from standard deviation of two-dimensional Gaussian curves fitted to the diffraction peaks.

5.8 Conclusions

In summary, in this Chapter, we have demonstrated a modified MBE approach, that uses sublimated SnO_x from a SnO_2 powder source, and enables growth of high quality $Ba_xSr_{1-x}SnO_3$ thin films across the entire composition range. Our method has successfully avoided problems associated with MBE using a Sn metal source. It has also allowed for improved stoichiometry of (Ba,Sr)SnO_3 films, which has been shown to be crucial for growth of high quality perovskite oxides like $SrTiO_3$ with high low-temperature mobilities [47], among others [48]. In addition, we have also demonstrated growth of high-quality films of coherently strained $SrSnO_3$ films on a nearly lattice matched substrate, $PrScO_3$, and completely eliminating any extended defects.

It must be noted that after the publication of results in this Chapter, two other approaches to MBE growth of $BaSnO_3$ thin films have been published. One of them utilizes the traditional Sn metal approach but utilizes ozone to oxidize Sn [17]. Another approach extends the hybrid MBE technique to utilize a non-oxidized metal-organic precursor (Hexamethylditin) and oxygen plasma [172].

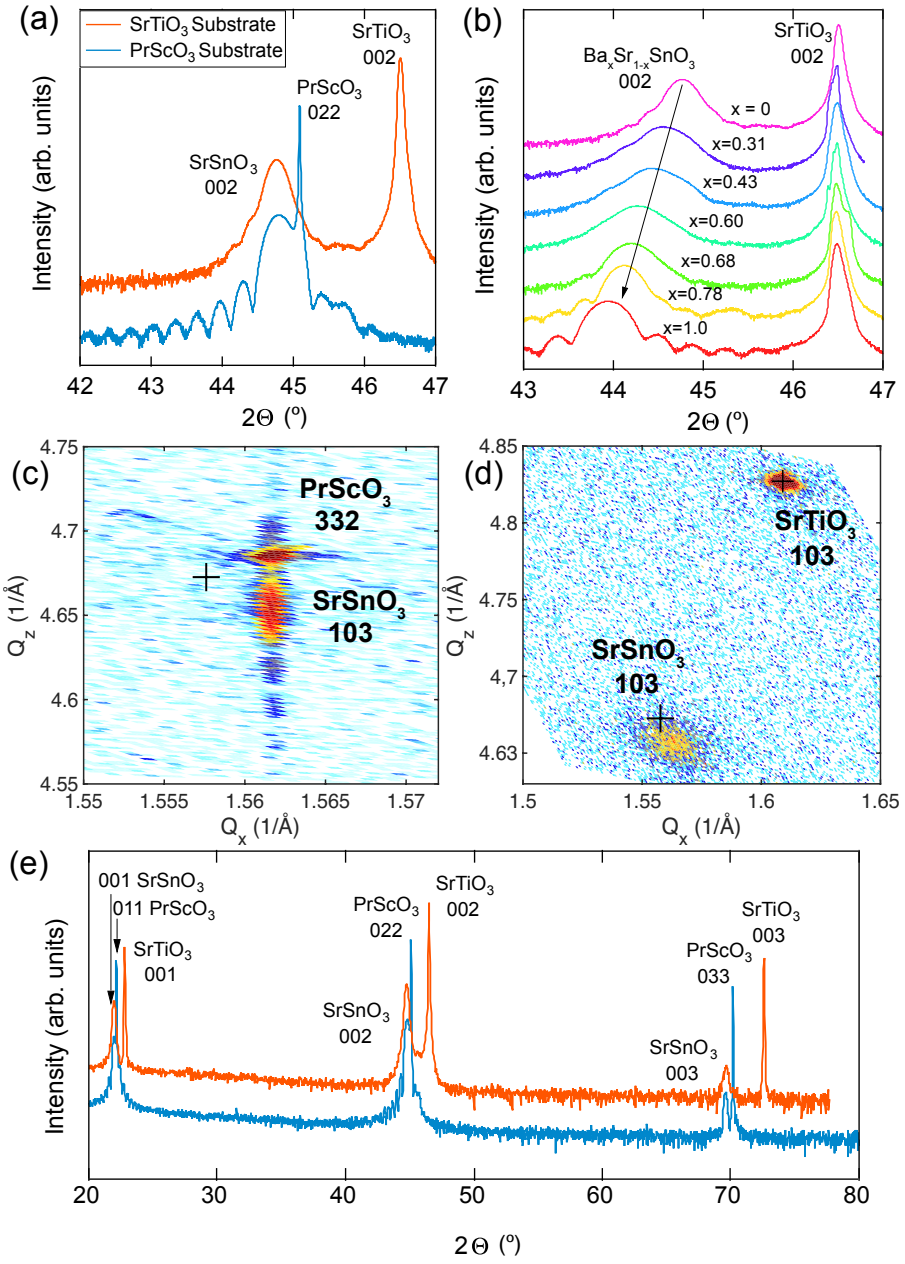

Figure 5.10: (a) On-axis high resolution XRD of $SrSnO_3$ films on $SrTiO_3$ (film thickness 41nm) and $PrScO_3$ (film thickness 31nm), respectively. (b) On-axis XRD of $Ba_xSr_{1-x}O_3$ films. The film thicknesses range between 25 and 41nm. (c) RSM around the 103_{pc} reflection for a $SrSnO_3$ film on $PrScO_3$. (d) Same as (c) except for a film on a $SrTiO_3$ substrate. The axes denote the in-plane (Q_x) and out-of-plane (Q_z) scattering vectors, scaled as $2\pi/a$, where a is the real-space distance of the respective lattice plane. The black crosses indicate the expected values for relaxed, bulk $SrSnO_3$.(e) Wide angle XRD scans showing growth of single-phase $SrSnO_3$ films on $SrTiO_3$ and $PrScO_3$. [Adapted with permission from [12].]

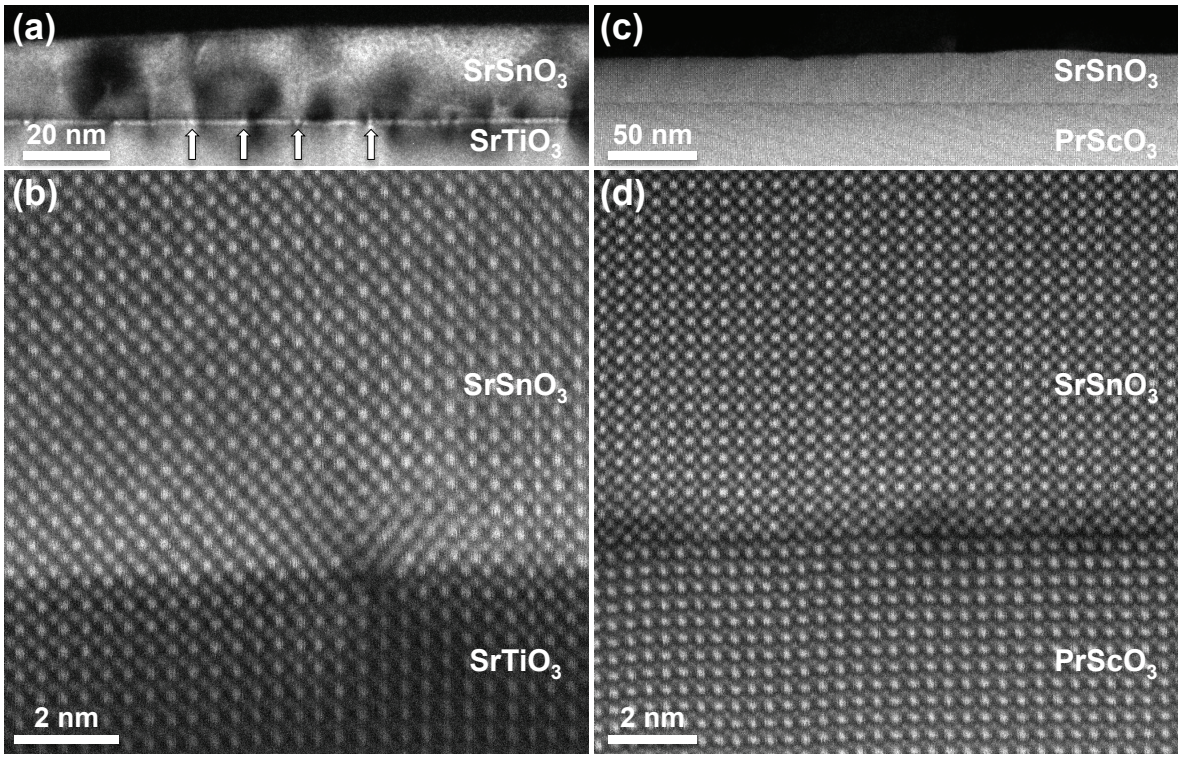

Figure 5.11: (a) and (b) Dark-field TEM image and HAADF-STEM image of a $SrSnO_3$ film grown on $SrTiO_3$. The white arrows in (a) indicate the location of misfit dislocations at the interface. (c) and (d) HAADF-STEM images of $SrSnO_3$ films grown on $PrScO_3$, showing epitaxial growth and no detectable extended defects. [Adapted with permission from [12].]

Chapter 6

Transport Properties and Band-gaps of Perovskite Stannate Thin Films

High-quality films of $BaSnO_3$ with low defect densities are crucial for electronic device applications. Fig. 6.1 summarizes the mobility results of all $BaSnO_3$ films grown in literature using various deposition techniques, like sputtering and pulsed laser deposition (PLD). Most films are degenerately doped to high carrier densities on various substrates. Fig. 6.1 includes data from PLD grown $BaSnO_3$ films on lattice matched $BaSnO_3$ substrates, with maximum mobility of 100 $cm^2/V{\cdot}s$. This value is 3 times lower than mobility in single crystals of La doped $BaSnO_3$, indicating that a huge role of off-stoichiometry from deposition in limiting mobility.

In Chapter 5, we studied the structural properties of perovskite stannates grown using a modified approach to conventional molecular beam epitaxy, where we replace the commonly used Sn metal source with SnO_2. In this Chapter, we present the transport properties of La doped $BaSnO_3$ films grown using this modified approach.

6.1 $BaSnO_3$: Mobility Dependence on Carrier Density

Lack of lattice matched substrates has been identified as a major challenge for growth of high quality $BaSnO_3$ films. Fig. 6.1 shows the Hall carrier mobility (μ) at 300 K as a function of 3D carrier density (n_{3D}) for our MBE grown La doped $BaSnO_3$ films on $SrTiO_3$, $PrScO_3$ and $DyScO_3$ substrates. The best reported values for films from literature as shown in the background for comparison. For films on $SrTiO_3$ substrate, the mobility for 30 nm thick MBE films is $\sim$100 $cm^2/V{\cdot}s$. It increases to $\sim$124 $cm^2/V{\cdot}s$ for 64 nm thick films, likely due to a reduction in scattering from the interface and/or some reduction in the threading dislocation density. This value is 24% higher than that of best films grown by PLD on $BaSnO_3$ substrates [18], and even higher than the recently published $\sim$115 $cm^2/V{\cdot}s$ obtained using hybrid MBE technique on $SrTiO_3$ substrates with $\sim$120 nm thick buffer layers [172, 16]. On $PrScO_3$, mobility of 30 nm thick MBE films reaches 150 $cm^2/V{\cdot}s$, 30% higher than any film reported in literature. On $DyScO_3$ substrates, the highest measured mobility of $\sim$172 $cm^2/V{\cdot}s$ was obtained on 61 nm thick MBE films, for similar carrier densities between 5–7$\times10^{19}$ cm^{-3}.

For all substrates, it has been seen that mobility reduces at lower carrier densities. This trend is similar to what has been observed for most films in literature, except for homoepitaxial $BaSnO_3$ films where such a trend is not observed. This indicates that even in MBE grown films, there exists charge trapping and carrier compensation due to dislocations and/or other defects.

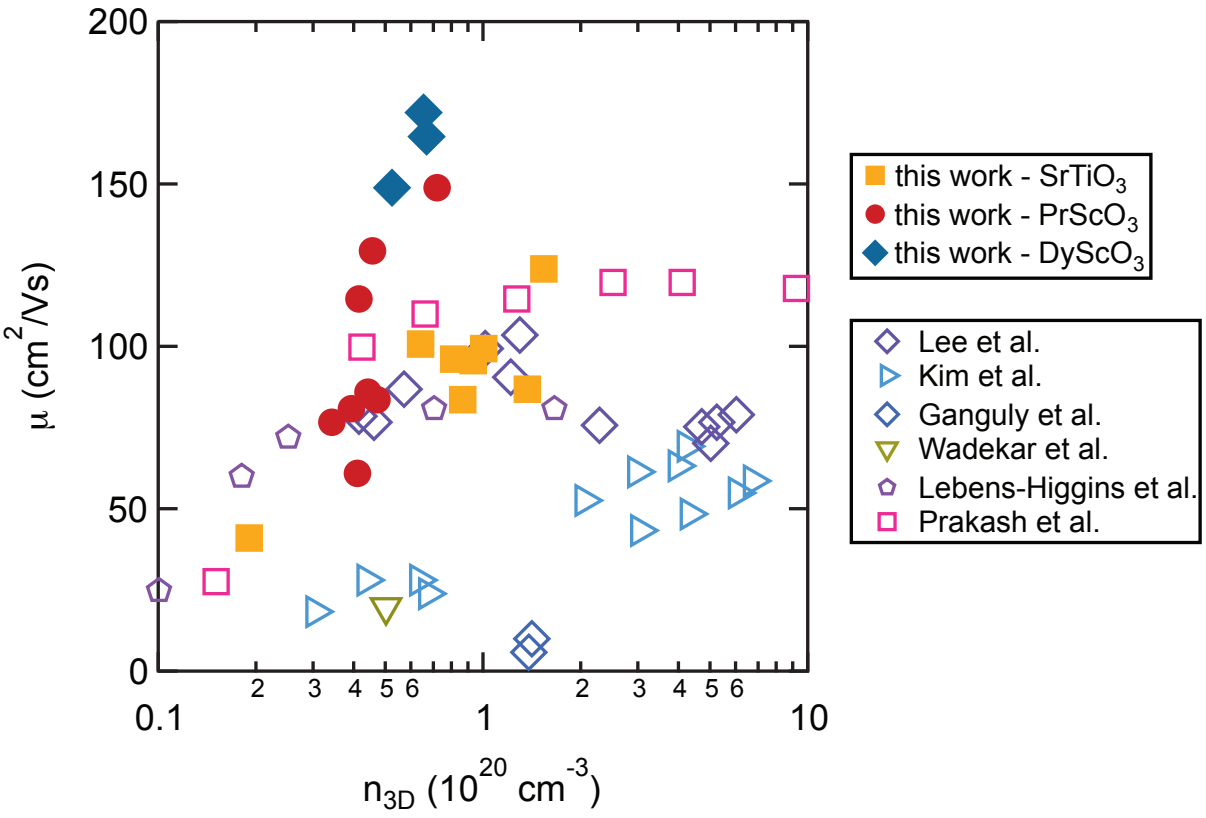

Figure 6.1: Mobility at 300 K as a function of 3D carrier density for $BaSnO_3$ films grown on (001) $SrTiO_3$, (011) $PrScO_3$, and (011) $DyScO_3$ using oxide MBE (this work), and from reports from the literature [13, 14, 15, 16, 17, 18].

6.2 $BaSnO_3$: Temperature Dependence of Mobility

Fig. 6.2 shows the temperature dependence of transport properties on $SrTiO_3$, $PrScO_3$, and $DyScO_3$ respectively. The carrier densities (Fig. 6.2(c)) in the films are similar. There is a slight increase in carrier density with increasing temperature, indicating a small amount of charge trapping at lower temperatures, even at this high doping densities. All films show metallic behavior down to 4 K (Fig. 6.2(b)), indicating that they are degenerately doped, similar to the bulk single crystals. The mobility value (Fig. 6.2(d)) increases with decreasing temperature, as expected for a LO phonon limited scattering at room temperature which has been observed in most perovskite oxides. The μ value

almost doubles between 300 K and 4 K. There is a change in the slope of the curve around 100 K for all films, where mobility starts to saturate as it becomes limited by scattering from disorder and/or defects. Since the low-temperature mobility is expected to indicate the extent of scattering from disorder, it can be used for comparing mobility values of $BaSnO_3$ films on different substrates. There is a clear increase in mobility for films on $PrScO_3$ and $DyScO_3$, when compared to films on $SrTiO_3$ substrates. This could indicate a reduced dislocation density for films grown on $PrScO_3$ and $DyScO_3$ substrates that results in reduced scattering. However, there still exists a large lattice mismatch between films on $PrScO_3$ (–2.18%) and films on $DyScO_3$ (–4.3%), while the mobility values are comparable for films on both $PrScO_3$ and $DyScO_3$ substrates at all temperatures. This indicates that dislocations are likely not the only mobility limiting mechanism in the MBE grown films. Another source of disorder could be related to cation stoichiometry, which can be difficult to distinguish from XRD studies, as shown earlier for $SrTiO_3$ [9]. Thus, further investigation on improving film stoichiometry is required for further increasing the mobility in MBE grown films.

6.3 $Ba_xSr_{1-x}SnO_3$: Ellipsometry and Band-Gap Measurement

In order to analyze the change in band gap as a function of alloy concentration of the $Ba_xSr_{1-x}SnO_3$ thin films, spectroscopy ellipsometry was used to measure the direct band gap (courtesy of Kaveh Ahadi). J. A. Wollam M2000DI ellipsometer was used to obtain ellipsometry data (Ψ and Δ) at incident angles between 60°–75° and photon energies from 0.73 to 6.49 eV. A three-medium optical model was used, consisting of the bulk

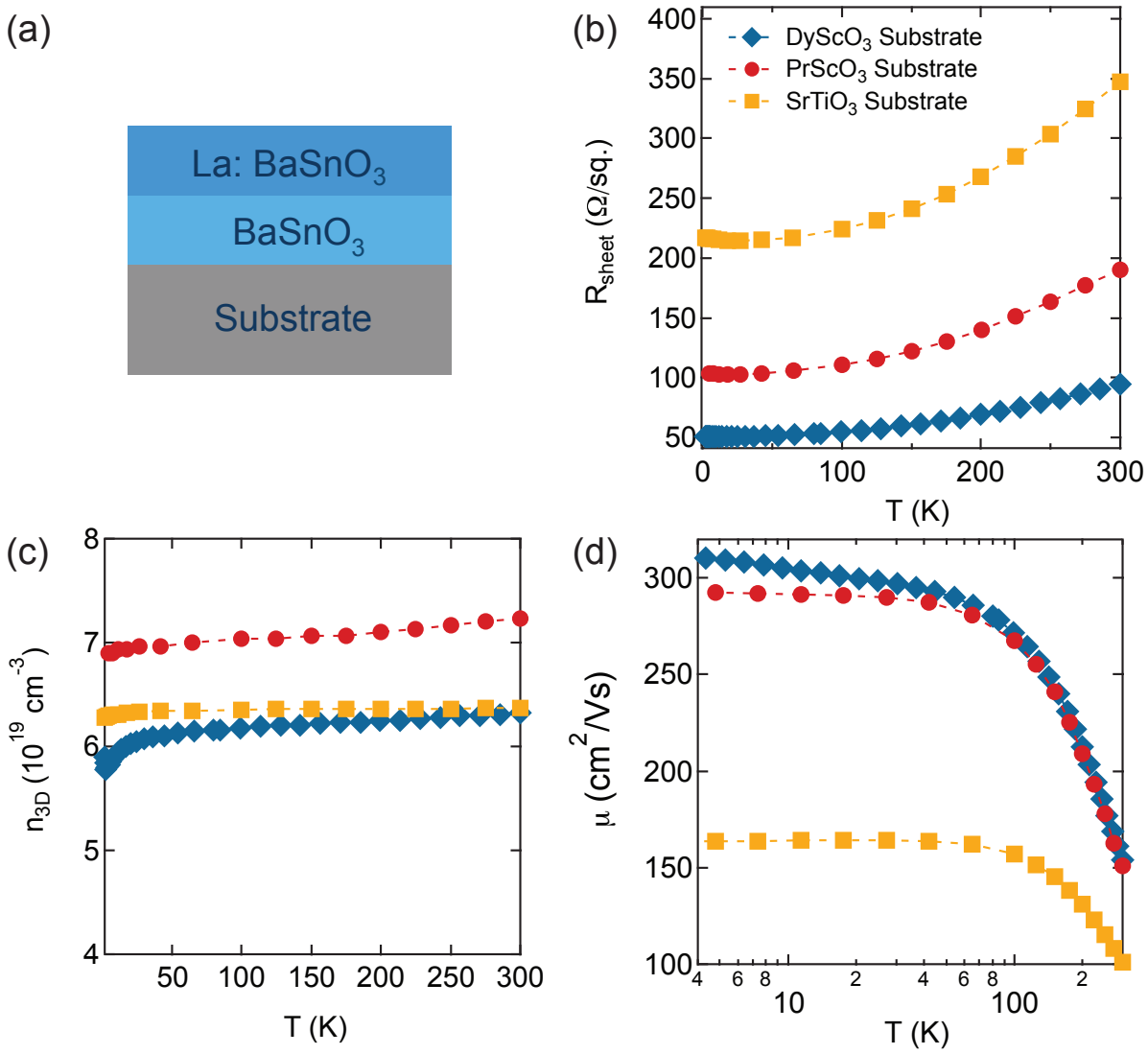

Figure 6.2: (a) Schematic of La doped $BaSnO_3$ films grown with a thin undoped buffer layer on various substrates. (b) Sheet resistance R_{Sheet}, (c) carrier density n_{3D}, and (c) mobility μ as a function of temperature T for $BaSnO_3$ films on $SrTiO_3$, $PrScO_3$ and $DyScO_3$ substrates, respectively.

$SrTiO_3$ substrate, the $Ba_xSr_{1-x}SnO_3$ film, and a surface roughness layer [173, 174]. A Tauc-Lorentz oscillator was used to model the optical response of the film for the energy region around the band gap, and a Lorentz oscillator for energies above the band gap. X-ray reflectometry was used to obtain the thickness of the films, and was fixed in the model. The remaining parameters of the oscillators were fitted by least squares regression

analysis.

The optical band gaps were estimated from Tauc plots using the relation:

$$(\alpha h\nu)^n = A(h\nu - E_g) \tag{6.1}$$

where h is Planck's constant, A is a constant, ν is the frequency, E_g is the band gap, and n is a constant that indicates the nature of the transition (either direct/indirect or allowed/forbidden). In this case, we use n=2, corresponding to a direct allowed band gap. Previous reports have fit measurements on undoped $BaSnO_3$ to an indirect band gap model (n=0.5) [175]. However, the measured absorption for such films is orders of magnitude too high for a typical indirect band gap in a thin film [176]. Therefore, only a direct band gap should be extracted. Fig. 6.3(a) shows Tauc plots for $BaSnO_3$ films with different doping densities, and a $SrSnO_3$ film. The extracted band gaps for the entire range of $Ba_xSr_{1-x}SnO_3$ thin films is shown in Fig. 6.3(b). The band gaps monotonously increases from Ba-rich to Sr-rich films (decreasing x), but does not follow a linear Vegard's law. No large strain effects on band gap are expected since all the films are grown on $SrTiO_3$ substrate and (almost) fully relaxed. Most band gap values reported in literature for stannates are for $BaSnO_3$. The measured gap of 3.36 eV for undoped $BaSnO_3$ is smaller than values reported for single crystals from ellipsometry ($\sim$ 3.5 eV) [177], thin films in ellipsometry and optical absorption [178, 179]. However, our resul is slightly larger than values measured on ceramics [1] and single crystals [3] measured by optical absorption.

For most semiconductors, substantial doping raises the Fermi level (E_F) away from the conduction band minimum, and increases the measured optical band gap. This is

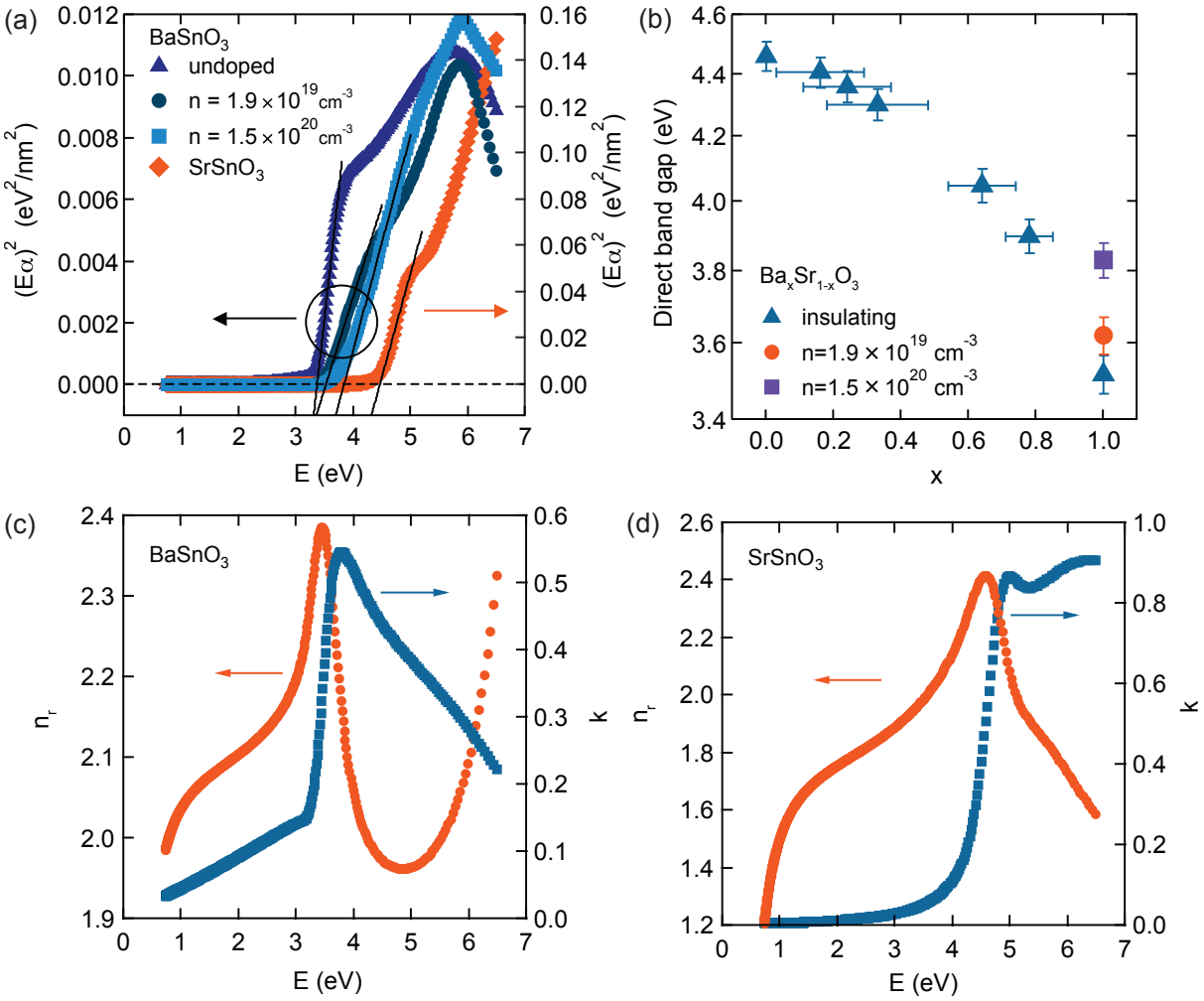

Figure 6.3: (a) Plots of $(E\alpha)^2$ as a function of photon energy E, which were used to determine the band gaps from spectroscopic ellipsometry, shown here for $SrSnO_3$ and $BaSnO_3$ with three different carrier densities: nominally undoped, n_{3D}=2.9×10^{19}cm^{-3} and 1.5×10^{20}cm^{-3}. (b) Extracted band gap values for $Ba_xSr_{1-x}SnO_3$ films, with x determined from the lattice parameter measurements. Refractive index n_r and extinction coefficient k values obtained by ellipsometry from (c) undoped $BaSnO_3$ and (d) $SrSnO_3$ films. [Adapted with permission from [12].]

called the Burnstein–Moss shift. For a single parabolic conduction band minimum, which is a decent approximation for $BaSnO_3$, the position of E_F above the conduction band

minimum (E_{CBM}) is given by:

$$(E_F - E_{CBM}) = \frac{h^2}{8m^*}\left(\frac{3}{\pi}\right)^{2/3} n_{3D}^{2/3} \tag{6.2}$$

where m^* is the effective mass, n_{3D} is the carrier density. For the two doped samples shown in Fig. 6.3(b), the n_{3D} values are 2.9×10^{19} and 1.5×10^{20} cm^{-3}. An effective mass of the conduction band edge of 0.19 ($\pm$ 0.01) m$_e$ in the La doped $BaSnO_3$ films was measured using the plasma frequency by glancing incidence, parallel-polarized resonant reflectivity (courtesy of S. James Allen) [180]. This results in $E_F - E_{CBM}$ of 0.18 and 0.55 eV, respectively, for the two samples. These values are in good agreement with the increase in the optical band gap measured using ellipsometry for the two samples, of 0.15 and 0.47 eV, respectively, relative to the undoped sample (Fig. 6.3(b)). Some recent reports [17] suggest significant band gap renormalization (shrinking of the band gap at high dopant concentration) of $\sim$ 0.4 eV for n_{3D} of $\sim 10^{20}$ cm^{-3}. Such a large renormalization would almost completely eliminate the Burnstein–Moss shift. However, our data does not support a strong band gap renormalization, and is also consistent with predictions from DFT [181].

All $Ba_xSr_{1-x}SnO_3$ thin films in this study were doped with 0.2%–0.3% La. However, only the Ba-rich films (x = 1 and x= 0.8) were electrically conductive when doped with La. The reason for the inability to dope Sr-rich films is unclear and requires further investigation.

6.4 Conclusions

In summary, we have shown that our modified MBE approach enables growth of high-quality $BaSnO_3$ films with room temperature mobilities of 172 $cm^2/V{\cdot}s$, significantly higher than any other reported growth method. Our results on the effect of mobility on lattice mismatch shows that mobilities can be further increased by development of lattice matched substrates and improved stoichiometry. High-quality films of completely strained $SrSnO_3$ films on a nearly lattice matched substrate, $PrScO_3$, as evidenced by XRD and TEM in Chapter 5, highlights the promise of future improvements in mobility for $BaSnO_3$. Ease of availability of more closely lattice matched substrates will allow for similar reductions in extended defect densities. In addition to $BaSnO_3$ itself (only small flux grown needles have so far been reported [154]), several other candidates exist [182, 19] but are not commercially available yet. An alternative approach would be growth of thick relaxed buffer layers, similar to what is used for GaN-based technologies.

We have also shown that the high-quality $Ba_xSr_{1-x}SnO_3$ thin films grown by MBE allow for developing band gap and strain engineered heterostructures with perovskite stannates. A consistent picture of the relationship between composition and optical properties has emerged. The band gap measurements of doped $BaSnO_3$ films show a strong Burnstein–Moss shift, which is consistent with a light conduction band mass, and negligible band gap renormalization. MBE of $Ba_xSr_{1-x}SnO_3$ thin films thus opens up paths for numerous potential applications using oxide electronics with high-mobility channels.

Chapter 7

Summary and Outlook

In this dissertation, it has been demonstrated that perovskite titanates and stannates offer a wide range of interesting properties that can be harnessed for functional oxide electronics. We have utilized hybrid molecular beam epitaxy to explore novel geometries in perovskite titanate heterostructures and studied the intrinsic properties of two-dimensional electron liquids at these interfaces. It has been shown that growth of high-quality films has been crucial for the development of these heterostructures that allow for studying the interplay between structure and resulting properties.

While two-dimensional electron liquids have been studied in oxide interfaces, their low carrier mobility had prevented advancement of the field. In this thesis, we have developed a new MBE technique for growth of high-quality films of perovskite stannates, which possess mobilities that are an order of magnitude higher than that of most other perovskite oxides. We have shown that films with a wide range of band gaps can be obtained using the developed growth technique.

More specifically, the following goals and questions have been addressed in this thesis:

1. Absence of a critical thickness for formation of 2DELs at (001) $R\mathrm{TiO_3}/\mathrm{SrTiO_3}$

interfaces, and demonstration of a 2DEL at the (111) RTiO$_3$/SrTiO$_3$ interface.

2. Measurements of the subband structure of the 2DEL at RTiO$_3$/SrTiO$_3$ interfaces and comparison with theoretical predictions.

3. Interaction between ferroelectricity and metallicity in BaTiO$_3$ and presence of a critical thickness for metal-insulator transition.

4. Development of a MBE technique for perovskite stannates that addresses the challenges of growth with Sn metal.

5. Growth of high-quality perovskite stannate films with high room temperature mobilities and wide range of band gaps for band-engineered heterostructures.

The results from individual chapters are now summarized along with a possible future outlook for the different projects. In Chapter 1, the different material systems of interest to this thesis and their general properties are introduced. Molecular beam epitaxy, the low energy deposition method used to grow thin films of these materials is explained and its main advantages are illustrated. The various mechanisms that scatter charge carriers in complex oxide thin films and limit mobility are also introduced.

In Chapter 2, the polar discontinuity at the interface of RTiO$_3$ (R: rare-earth element) and SrTiO$_3$ is introduced. We study the origin of the two-dimensional electron liquid (2DEL) that results due to the polar discontinuity. We study the absence of a critical thickness of RTiO$_3$ for formation of a 2DEL at the (001) interface. Later, the polar discontinuity concept is extended to the (111) oxide interface. We elucidate the difference in the electronic nature of the (001) and (111) 2DELs by analyzing the temperature dependent mobility of the two 2DELs. The presence of LO phonons in determining transport of carriers in (111) 2DELs is used to differentiate the nature of confinement

of the 2DELs at the two interfaces. The anisotropic nature of $SrTiO_3$ Fermi surface is confirmed using the transport of (111) 2DELs along two different crystallographic directions. However, one of the shortcomings of this study has been the failure to grow high quality RTiO$_3$/SrTiO$_3$/RTiO$_3$ quantum wells along the (111) orientation, for studying the predicted topological behavior [82, 83]. This has been due to the problems associated with roughening of the (111) surface of RTiO$_3$ films grown on (111) LSAT substrates. Recent growth studies on (111) $LaNiO_3$ films indicate that roughening can be avoided by using a polar (111) substrate with a uniform surface termination [183, 184]. Future growth studies of RTiO$_3$ on (111) $DyScO_3$ or $GdScO_3$ substrates, along with different surface miscut, might be a step in the right direction.

In Chapter 3, the subband structure of 2DELs at the (001) RTiO$_3$/SrTiO$_3$ interface is introduced. A qualitative understanding of the different subbands is provided, and the resonant tunneling experiment designed to study these subbands is introduced. The slight asymmetry between the 2DEL at (001) RTiO$_3$/SrTiO$_3$ and SrTiO$_3$/RTiO$_3$ interface is illustrated. The results of the resonant tunneling experiment are described and the subband separation is measured from the I-V measurements. The energy spacing between subbands of the two 2DELs is compared to theoretical predictions made using various computational methods for subbands in $SrTiO_3$ 2DELs. The temperature dependence of the spacing is also described. Future studies can use this technique to study the effect of the epitaxial strain and carrier density on the subband spacing of $SrTiO_3$ 2DELs, and can also be extended to other oxide interfaces.

In Chapter 4, the long-standing debate about co-existence of ferroelectricity and metallicity in $BaTiO_3$ samples is introduced. The debate necessitates the need for discerning between effects of disorder from doping and the resulting effect on structure and

transport of $BaTiO_3$. A novel method of introducing carriers into $BaTiO_3$ without introducing associated dopants is proposed that uses electrostatic doping from polar discontinuity between RTiO$_3$ and $BaTiO_3$. The hybrid MBE technique developed for growth of $SrTiO_3$ is extended for high-quality $BaTiO_3$ films, and ferroelectricity is confirmed using piezo-force microscopy and capacitance-voltage measurements. Layers of varying $BaTiO_3$ thickness are then introduced between RTiO$_3$ and $SrTiO_3$ layers to study the resulting transport properties of the interface. We show that a sharp metal-to-insulator transition is observed at a critical thickness of 3 u.c. (4 BaO) layers. Concomitantly, a change in the tetragonal distortion associated with ferroelectricity is observed across the metal-to-insulator transition. The change in conduction behavior along with a structural transition is used to describe the transport behavior of carriers at the RTiO$_3$/$BaTiO_3$ interface. We see that ferroelectricity and metallicity can not co-exist in $BaTiO_3$ in the traditional sense where there is metallic conduction within the bulk of the ferroelectric. Instead we observe that the ferroelectricity pushes carriers out from the bulk against the interface, resulting in a polaron gas with poor mobilities. Through this study, we have shown that electrostatic doping is a viable technique to introduce large amounts of carriers in oxide films without introducing associated dopant disorder, and can be used for studying metal-insulator transitions in other perovskite oxide systems.

Chapter 5 illustrates the challenges associated with growth of high-quality perovskite stannates using molecular beam epitaxy. The growth challenges and resulting films associated with oxidation of Sn from a conventional Sn metal cell is highlighted. The problems associated with extending the hybrid MBE technique to perovskite stannates is also illustrated. A modified MBE technique is introduced that uses SnO_2 powder as a source of supplying pre-oxidized Sn. The advantages of using the SnO_2 source and resulting high quality of perovskite stannate films are described. Structural characterization

data using XRD, AFM and TEM is used to demonstrate the quality of $BaSnO_3$, $SrSnO_3$ and $Ba_{1-x}Sr_xSnO_3$ thin films grown using the modified MBE technique.

In Chapter 6, we study the transport properties of La doped $BaSnO_3$ films grown using the modified oxide MBE technique. We report films with record high mobilities exceeding 170 $cm^2/V{\cdot}s$ at carrier densities between 5-to-7$\times 10^{19}$ cm^{-3}. We use low temperature transport to highlight the challenges faced in increasing room temperature mobility further – dislocations introduced due to lattice mismatch with substrate and need for improvement in achieving perfect cation stoichiometry in a reliable and reproducible fashion. We also report on ellipsometry measurements on $Ba_xSr_{1-x}SnO_3$ films to obtain optical band gaps as a function of alloy concentration and La doping. A systematic increase of the direct band gap is observed as a function of increasing Sr concentration in the alloys. We also report on increase in the optical band gap as a function of increased La doping in $BaSnO_3$ due to the Burnstein-Moss shift. A very negligible band-gap renormalization is observed in $BaSnO_3$, contrary to some results in literature [17].

Future work on stannate thin films requires further MBE growth studies on the effect of stoichiometry (Sn/Ba flux ratio) and undoped buffer layer thickness on the film mobility. Investigations on influence of substrate growth temperature in addition to methods for improved SnO_2 flux stability are required to achieve an adsorption-controlled MBE growth window for self-regulating stoichiometric $BaSnO_3$ films. Progress has been made in the recent years in tackling the challenge of lattice matched substrates for $BaSnO_3$. The recent development of $SrZrO_3$ (orthorhombic crystal structure with pseudocubic lattice parameter 4.103 Å) and $(LaLuO_3)_x(LaScO_3)_{1-x}$ substrates (orthorhombic crystal structure with pseudocubic lattice parameters ranging from 4.09 Å and 4.18 Å based on x) [19] are promising for growth of dislocation-free high-quality $BaSnO_3$ films with

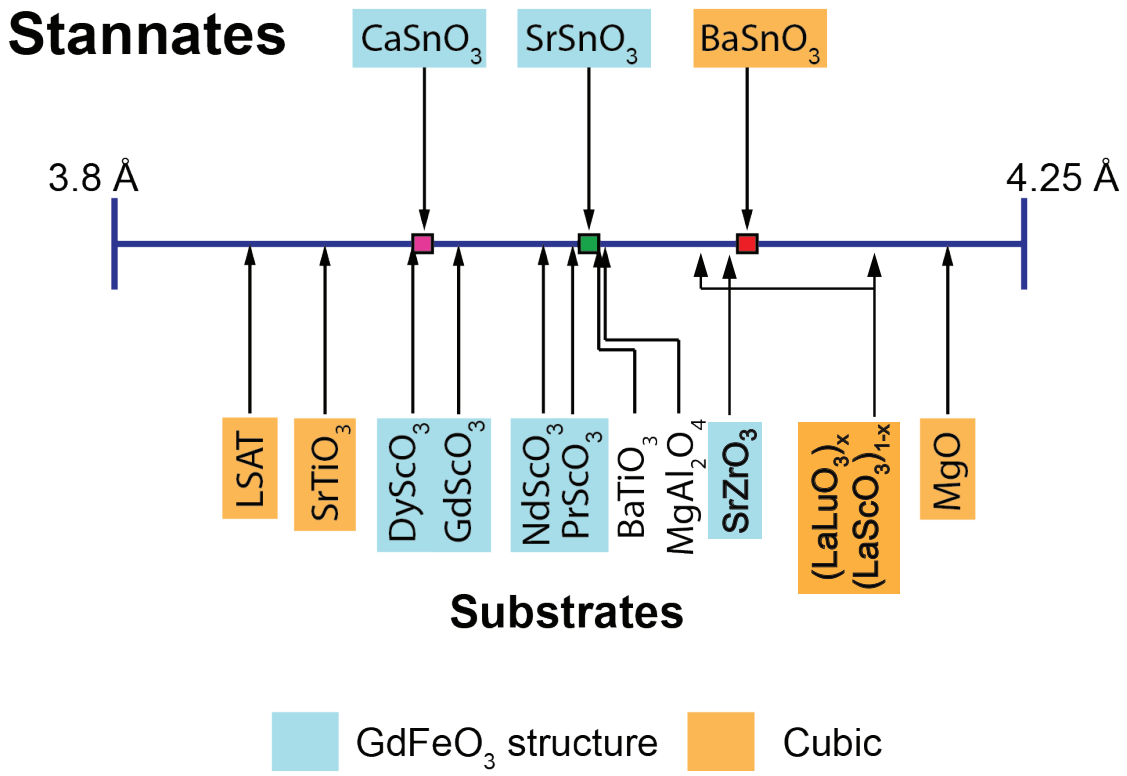

Figure 7.1: Lattice parameters (to-scale) of perovskite stannates and various commercially available substrates, illustrating the lattice parameter mismatch. In addition, the recently available $SrZrO_3$ substrates as well as the $(LaLuO_3)_x$ $(LaScO_3)_{1-x}$ substrates under development are shown [19].

improved mobility, as shown in Fig. 7.1.

Density functional theory calculations predict conduction band offsets ranging from 0.5 to 1 eV between (Sr,Ba)TiO_3 and $BaSnO_3$ [34]. A lower lying conduction band of $BaSnO_3$ allows for transfer for electrons from higher lying $SrTiO_3$ conduction band, as shown in Fig. 7.2 (a-b). Integration of $BaSnO_3$ with $R$$TiO_3$/$SrTiO_3$ interfaces and La-doped $SrTiO_3$ layers can result in electrostatic doping and modulation doping of carriers into the high mobility $BaSnO_3$ layer without introducing dopant disorder. The challenge of obtaining low doping densities in $BaSnO_3$ remains to be addressed and can be

problematic for oxide RF HEMT devices that requires excellent field-effect control of the underlying channel. Methods to overcome this challenge could include growth of thin layers of highly doped $BaSnO_3$ on top of $SrSnO_3$ back barriers for carrier confinement, and integration with high permittivity gate dielectrics (like $SrTiO_3$ and $Ba_xSr_{1-x}TiO_3$) for improved control of the doped oxide channel, as shown in Fig. 7.2(c). Notwithstanding, it can be seen that growth of the aforementioned heterostructures and precise band-engineering are crucial for high-mobility and high-carrier density oxide devices with numerous potential applications in high-power and high-frequency electronics.

In conclusion, the work described in this dissertation has lead to several important findings on the intrinsic nature of 2DELs at perovskite titanate interfaces. We have shown that new geometries using RTiO$_3$ and $SrTiO_3$ layers can be used to study properties like carrier confinement, Fermi surface anisotropy, electronic subband spacings, and metal-insulator transitions in titanates.

In addition, we have successfully developed a new technique for the growth of high quality perovskite stannate films. This has resulted in films with room temperature mobilities exceeding 170 cm^2/V·s at room temperature, and $Ba_{1-x}Sr_xSnO_3$ films with a wide range of band gaps. Although 2DELs in titanates and high mobility stannates have been worked on separately in this thesis, this work has laid the foundation for integrating the two material systems for next generation oxide electronics.

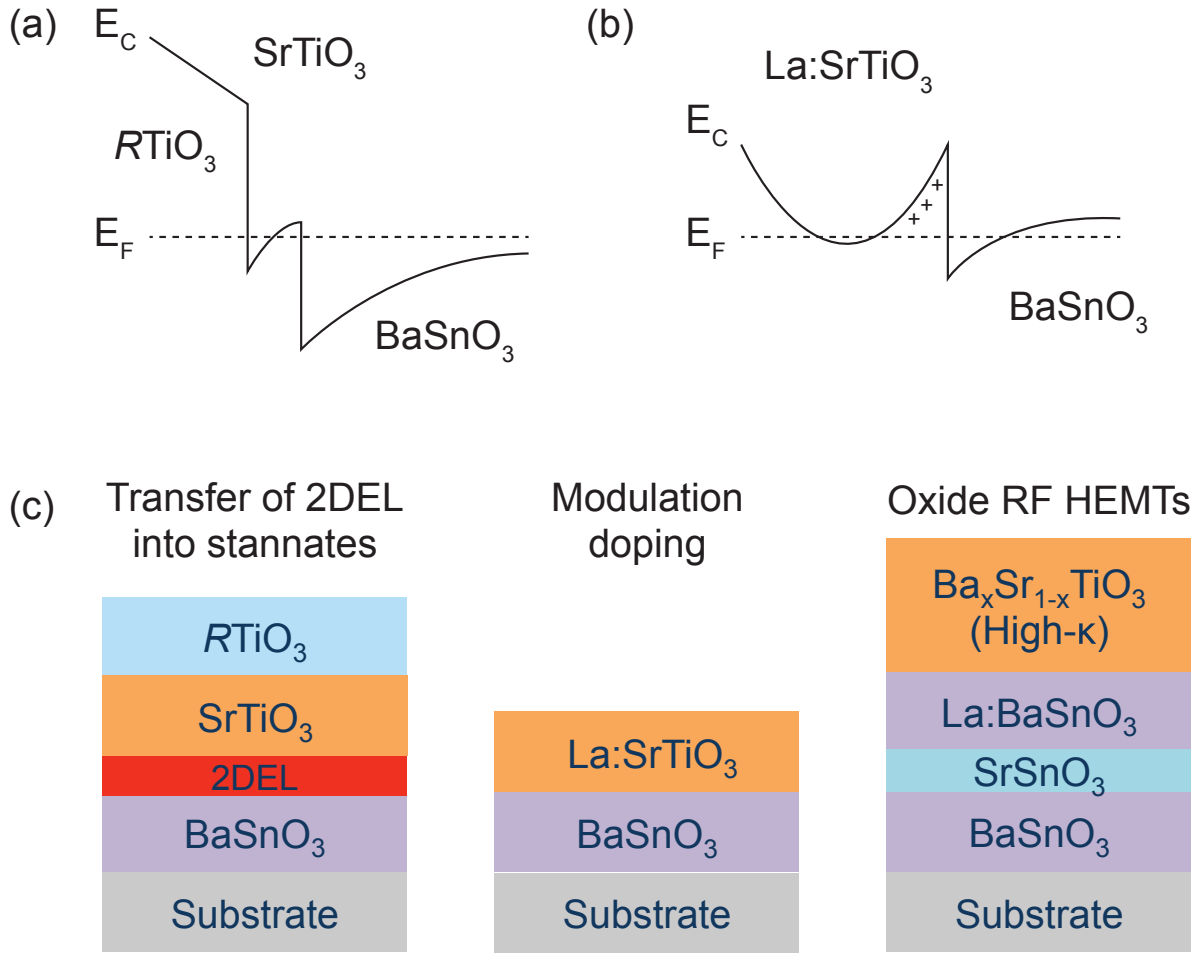

Figure 7.2: Schematic of the predicted (not-to-scale) conduction band alignment for (a) $R\mathrm{TiO_3}/\mathrm{SrTiO_3}/\mathrm{BaSnO_3}$ and (b) La-doped $\mathrm{SrTiO_3}/\mathrm{BaSnO_3}$ modulation-doping heterostructures. (c) Illustrations of various heterostructures with stannate and titanate layers for high-mobility and high-power applications.

Appendix A

Backing metal for oxygen-rich environments

Oxidation of metal backing layers during film deposition using MBE at high substrate temperatures and highly oxidizing environments has been highlighted as a challenge for perovskite stannate growths in Chapter 5. Here we present notes on various metals used for substrate backing to test substrate temperature stability and oxidation resistance. The substrates were backed with Ta, Pt, W, and Mo using e-beam evaporation under UHV conditions. The metal backing layers absorb infrared radiation from a standard Pt-Rh heater under UHV in the MBE chamber as shown in Fig. A.1(a-b). The substrate temperature is controlled using a PID controller that controls the power supplied to the output. The substrate temperature is monitored using a thermocouple as well as an optical pyrometer. Plotted in Fig. A.1(c) is the thermocouple and pyrometer temperature, as well as the output power for the heater as a function of time for a Ta-backed $SrTiO_3$ substrate under oxygen rich environments (oxygen partial pressure $\sim 1{\times}10^{-5}$ Torr). For a fixed thermocouple temperature, the optical pyrometer records an increase of almost 50 °C over 1 hour. Similar trend was observed for W metal backing layers, and indicates there is substantial oxidation of these backing metals during growth at high temperatures. As the metal oxidizes into a wide band-gap oxide (like Ta_2O_5 or WO_3),

the optical pyrometer reads higher temperatures as it receives more radiation from the heater, while the actual substrate temperature drifts away from the measured value and affects film growth. Pt metal is well known to be oxygen resistant and was tested as a backing layer for substrates. However, it was found that substrates were unable to reach high enough temperatures for film growth. Mo metal as found to be the best option, showing satisfactory oxidation resistance and minimal drift in substrate temperature ($\sim$ 5 °C) during film growth.

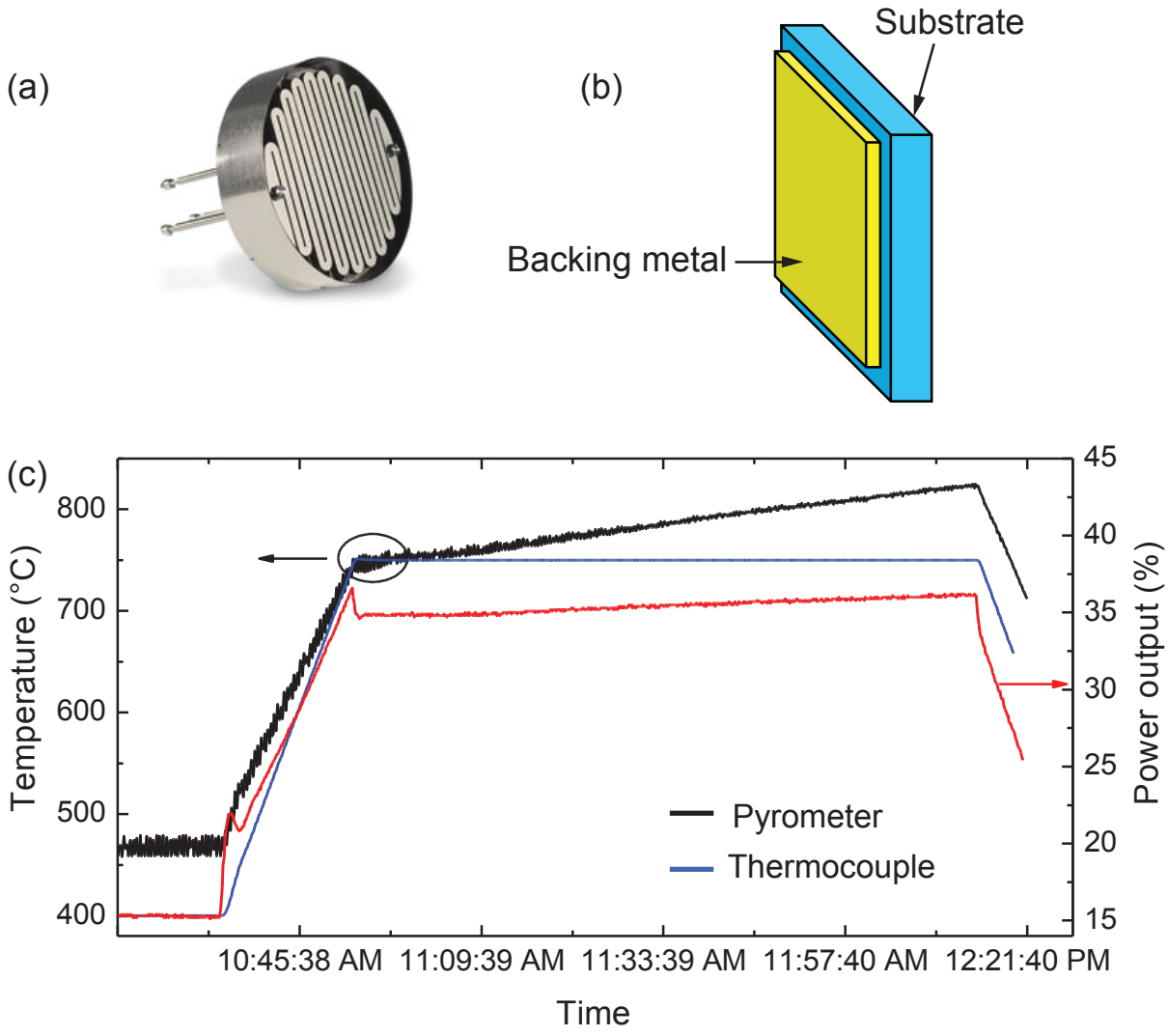

Figure A.1: (a) Schematic of the substrate heater and (b) the metal backing layer on the substrate. (c) Substrate temperature (and output power) as a function of time measured using the heater thermocouple and optical pyrometer for a Ta-backed $SrTiO_3$ substrate.

Appendix B

MBE Growths with Sn metal source

The growth of perovskite stannates using a Sn metal source in MBE is reported here. Solid state sources of Sn (which has a low melting point of 232 ^{o}C) and solid state sources of Sr and Ba were used for stannate growth. Activated oxygen for the stannate was provided using an RF plasma source.

B.1 MBE of Stannic Oxide

As mentioned in Chapter 5, a well known challenge in the MBE growth using Sn as the source material is the volatility of SnO (tin mono-oxide or Stannous oxide). Sn has two valence states, Sn(II) and Sn(IV) and can form SnO and SnO_2 (Stannic Oxide). SnO is a highly volatile oxide that has a high vapour pressure, especially at high temperatures. SnO_2 contrastingly is a stable oxide and it is the preferred oxidation state for stannate growth. Growth of SnO_2 using MBE has been a subject of investigation in the past [157, 185, 158]. The studies primarily predict three distinct regimes for growth of SnO_2. The first is an oxygen-rich regime where the amount of activated O atoms supplied is more than twice the amount of Sn atoms supplied, which allows for SnO_2 formation and the growth rate of SnO_2 increases with increasing Sn supply in this regime. When the rate of Sn atom supply reaches close to rate of activated O atom supply, a small amount

of Sn forms SnO (that desorbs from the sample surface) instead of forming SnO_2, causing a reduction in the growth rate with increasing Sn supply (Sn-rich regime). And at very high rates of Sn atom supply, all the Sn atoms either form SnO and desorb from the surface or form Sn droplets on the sample, leading to no SnO_2 growth. For the growth of perovskite stannates, the oxygen rich regime is desired for stable conditions of SnO_2 formation with Sn in +4 oxidation state.

In order to grow perovskite stannates, the SnO_2 growth regime on perovskite substrates is investigated first. Although growth of SnO_2 has been observed at temperatures as high as 800 ^{o}C for symmetry matched substrates like sapphire and TiO_2, no growth of SnO_2 was observed on perovskite substrates above 500 ^{o}C. For the incident Sn beam equivalent pressures (BEPs) that are relevant for perovskite stannate growths, SnO_2 films were grown on $SrTiO_3$ and $LaAlO_3$ substrates for varying incident Sn fluxes as shown in Fig.B.1. The growth rates of SnO_2 films were measured using a Dektak profilometer. The SnO_2 growth rates were seen to increase with increasing Sn incident fluxes, suggesting SnO_2 growth in the O-rich regime as desired. It must be noted that the growth of SnO_2 required very high oxygen incident fluxes (oxygen beam equivalent pressures $\approx 10^{-5}$ Torr) similar to previous studies [157, 185, 158].

B.2 MBE of Perovskite Stannates

Sr and Sn fluxes from the effusion cells were calibrated using the beam flux gauge, and initial growths of $SrSnO_3$ were performed at Sr/Sn ratios ranging from 5.0 to 0.2. XRD patterns of the films were used to find stoichiometric growth conditions as shown in Fig.B.2. Due to scarce availability of lattice matched $PrScO_3$ substrates, preliminary

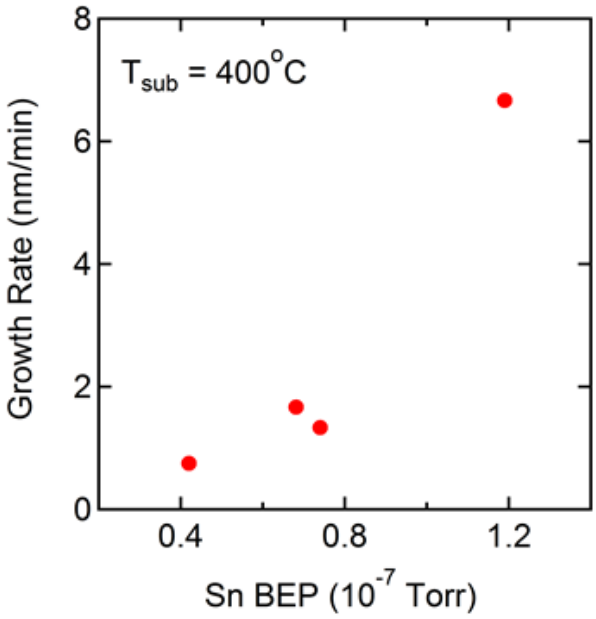

Figure B.1: Growth rate of SnO_2 as a function of incident Sn flux on $SrTiO_3$ substrates indicating SnO_2 growth in the O-rich regime, at Oxygen BEP $\approx 1\times10^{-5}$ Torr

growth calibrations were done initially on $SrTiO_3$ and $LaAlO_3$ substrates. Although, single phase thin films are obtained at the stoichiometric growth conditions at 550 ^{o}C on $SrTiO_3$, the growth of $SrSnO_3$ films monitored using RHEED indicated a rough surface, as shown in Fig. 5.2. During the start of the growth, when the Sr and Sn shutters are opened in the oxygen plasma ambience, the RHEED pattern vanishes. As the growth continues, the RHEED recovers showing a spotty patterns indicating a 3D growth of the perovskite film. The dramatic drop in the RHEED intensity is associated with the formation of Sn metal droplets on the film surface. No RHEED intensity oscillations were observed, which discounts the possibility of tin adlayer formation, similar to Ga-rich growth mode in GaN growths [186]. $SrSnO_3$ growths were attempted at higher temperatures on $SrTiO_3$ substrates to avoid the Sn droplet formation regime, but no perovskite growth was seen at temperatures higher than 600 ^{o}C. AFM indicated a rough surface with an RMS roughness of 10 nm, and TEM images displayed a defective film/substrate

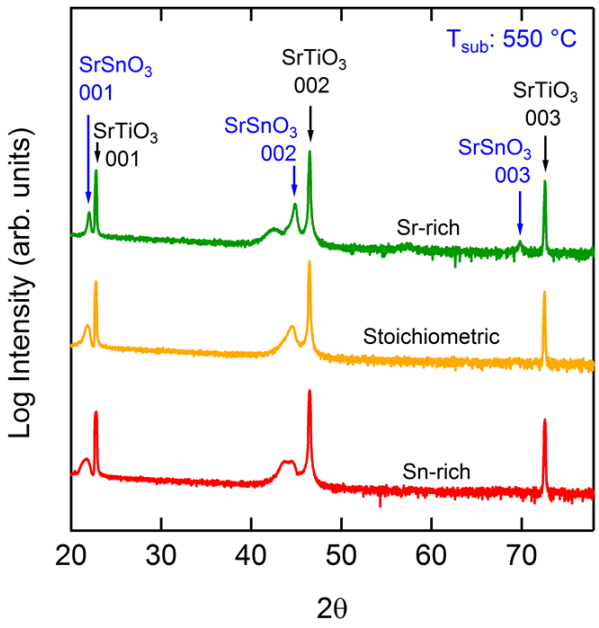

Figure B.2: XRD patterns of $SrSnO_3$ thin films grown at different Sr/Sn ratios on $SrTiO_3$ substrates at 550 ^oC indicating stoichiometric, Sr-rich and Sn-rich films

interface. There also seem to be indications of inter-diffusion between the film and the substrate, which has been reported in SnO_2 growths on TiO_2 substrates earlier [187]. Further growth calibrations were done on $LaAlO_3$ substrates to avoid this issue.

To better understand the origin of the 3D growth mode, ultra thin films of $SrSnO_3$ were grown on $LaAlO_3$ substrates at 600 ^oC for 5 minutes. The evolution of RHEED pattern with time (shown in Fig.B.3(a)) indicated a recovery in specular RHEED intensity at the end of the growth when the Sr and the Sn shutters close, and the film that grows underneath the metallic Sn layer becomes visible. This indicates that the Sn droplets desorb from the surface when Sn flux is no longer supplied. The thin film that grew underneath the Sn metallic layer was studied using XRD, as shown in Fig.B.3(b) and indicated growth of $SrSnO_3$, ruling out formation of alternate phases at the interface. AFM images of the ultra thin films (Fig.B.3(c)) indicate a much smoother surface

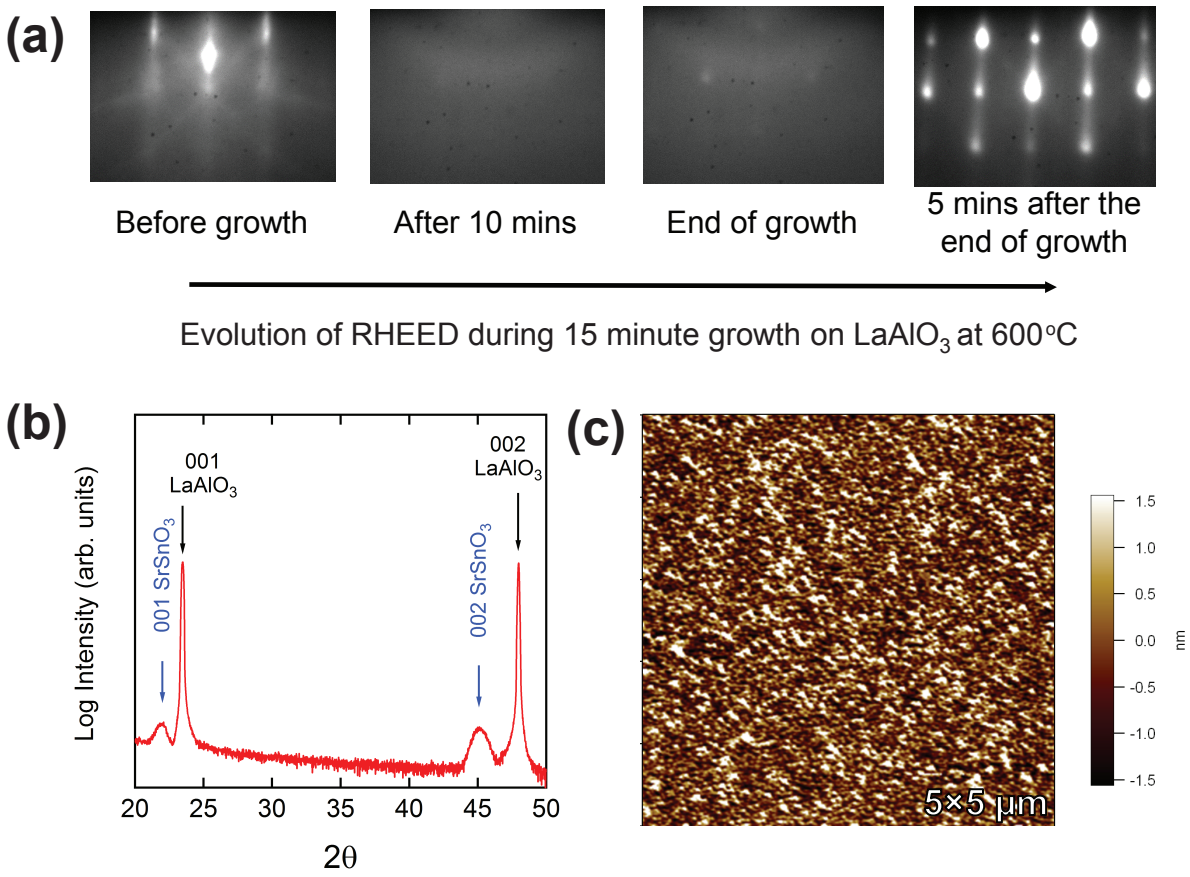

Figure B.3: (a) Evolution of RHEED during growth of ultra thin $SrSnO_3$ films on $LaAlO_3$ substrates at 600 ^oC. (b) XRD pattern indicating growth of single phase $SrSnO_3$. (c) AFM image of the $SrSnO_3$ film grown on $LaAlO_3$ substrate with an RMS roughness of 1 nm.

(RMS roughness of 1 nm) compared to the thicker films seen in Fig. 5.2. This suggests that small 3D islands form at the start of the growth with a smooth surface, and as the growth continues, the islands continue to grow larger and taller, and the film continues to become increasingly rough. At the end of the long growth, the roughness of the film allows for visibility of the RHEED pattern inspite of Sn droplet formation on the surface.

Attempts were made to grow $SrSnO_3$ films at higher substrate temperatures on $LaAlO_3$ substrates. Fig.B.4(b) shows the XRD patterns and the RHEED images along

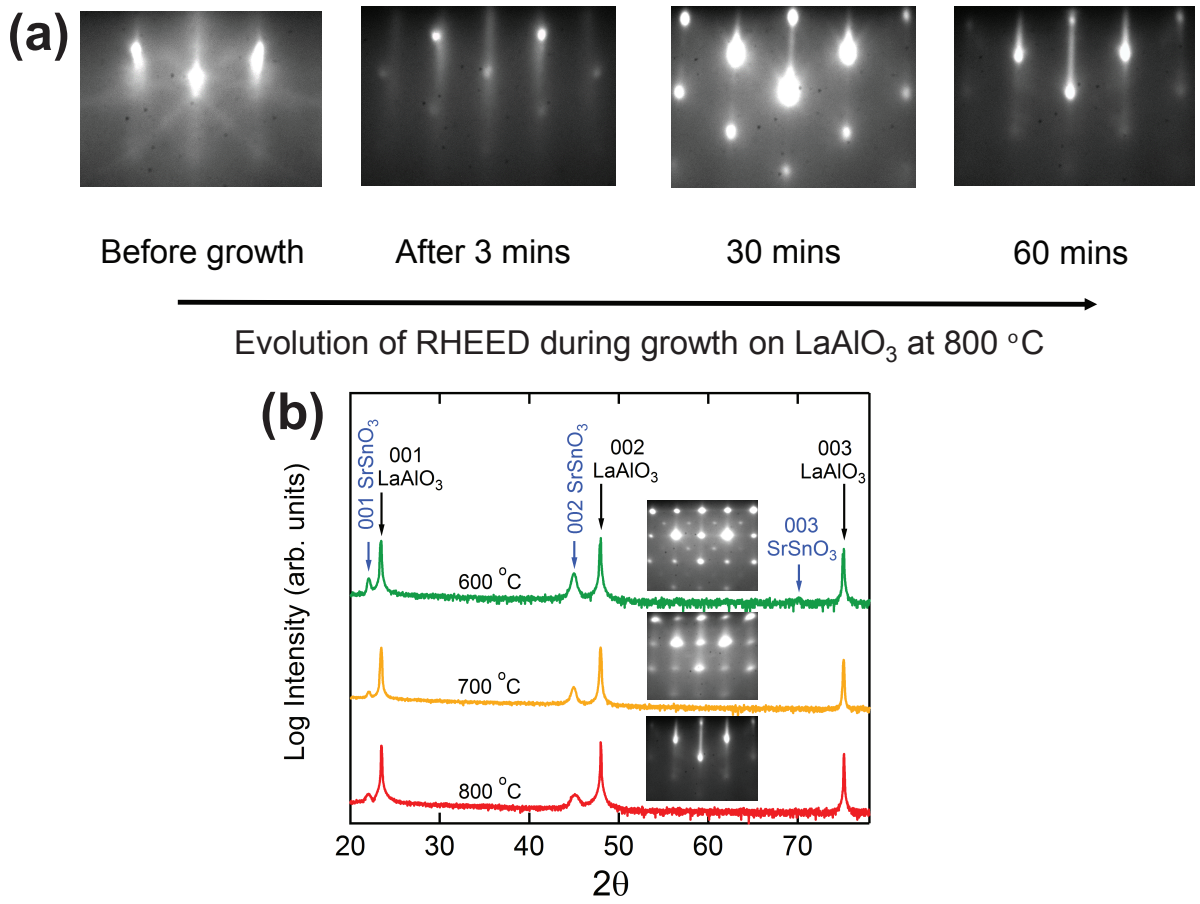

Figure B.4: (a) Evolution of RHEED images during $SrSnO_3$ growth on $LaAlO_3$ substrates at 800 ^{o}C. (b) XRD patterns of the $SrSnO_3$ thin films grown on $LaAlO_3$ at various substrate temperatures along with the RHEED pattern of film captured after growth

the 100 azimuth of the film/substrate at the end of the growth for various substrate temperatures. Growth of single phase $SrSnO_3$ films was observed at temperatures all the way up to 800 ^oC on $LaAlO_3$. As the substrate temperature was increased, the formation of Sn droplets on the substrate surface reduced. Films grown at 800 ^oC showed lower levels of reduction in the RHEED intensity at the start of the growth and the growing film was continuously visible in RHEED as seen in Fig.B.4(a). At higher growth temperatures, excessive desorption of the incident Sn is expected, resulting in lower Sn incorporation in the film. At growth temperatures above 800 ^oC, only SrO related peaks were observed in XRD and no $SrSnO_3$ film peaks were observed, similar to the case of $SrTiO_3$ substrate growths above 600 ^oC. Since desorption rate of Sn from the substrate surface should be exponentially dependant on the substrate temperature, similar to Ga desorption in GaN growths [188], a growth series within a finer temperature window was performed around 800 ^oC. It indicated that the Sr/Sn growth ratio chosen for these high temperatures were off-stoichiometric. This was followed by a series of varying Sr/Sn ratios on $LaAlO_3$ substrates at 750 ^0C to find the stoichiometric growth conditions as shown in Fig.B.5.

Using the stoichiometric growth conditions obtained above, $SrSnO_3$ growths were performed on lattice matched $PrScO_3$ substrates to investigate if the 3D growth was due to lattice mismatch. XRD patterns for these films are shown in Fig.B.6(a) where a broad shoulder is seen on the 002 film peak indicating off-stoichiometric Sr-excess in the films. Since the growth conditions of $SrSnO_3$ are sensitive to substrates chosen and due to wide variability in the actual substrate temperature due to their different band-gaps, further growth calibrations were found to be necessary. However, AFM images of $SrSnO_3$ grown on lattice matched $PrScO_3$ substrates, shown in Fig.B.6(b), demonstrated continuation of 3D island formation as the preferred growth mode when using a Sn metal cell.

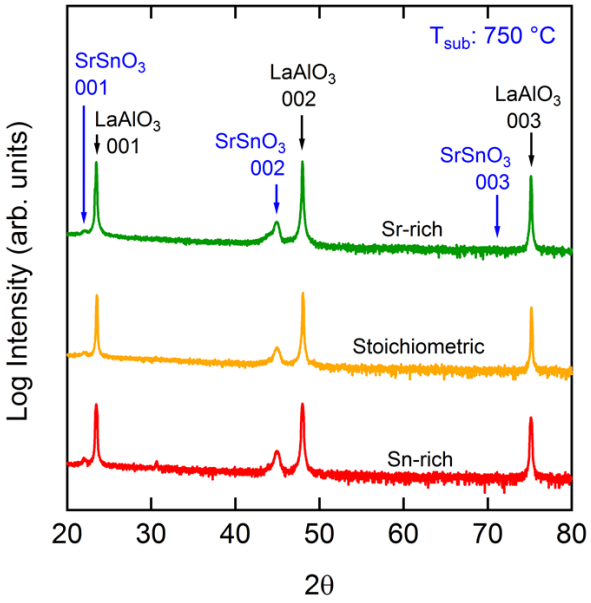

Figure B.5: XRD patterns of $SrSnO_3$ thin films grown at different Sr/Sn ratios on $LaAlO_3$ substrates at 750 ^oC indicating stoichiometric, Sr-rich and Sn-rich films.

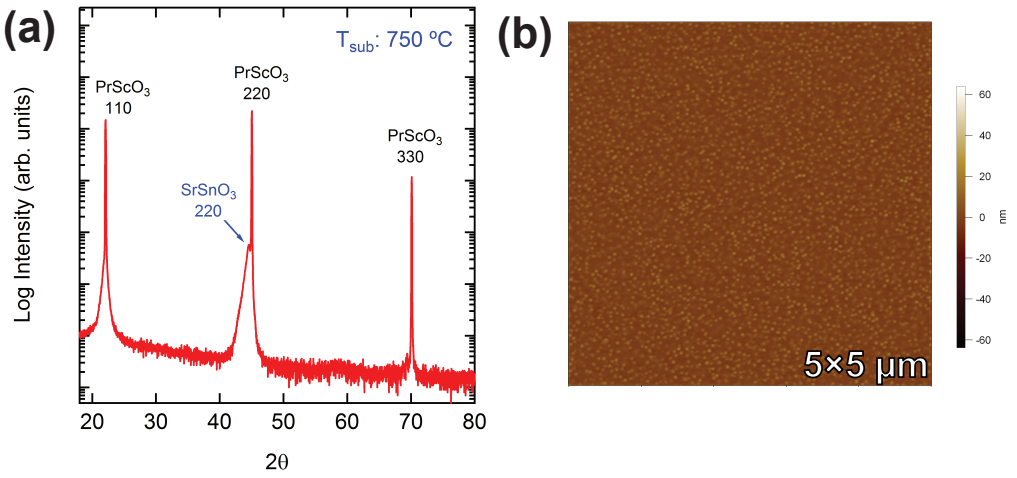

Figure B.6: (a) XRD pattern and an (b) AFM image of the $SrSnO_3$ thin film grown on $PrScO_3$ substrates

Appendix C

Absence of T^2 behavior in $BaSnO_3$

Chapters 2 and 4 discussed the role of T^2 scattering observed in $SrTiO_3$ over a large range of temperatures, including at room temperature for high density 2DELs. As discussed in Chapter 1, the origin of traditional T^2 scattering is from Fermi liquid theory and its applicability in $SrTiO_3$ at high temperatures requires further theoretical work. This precipitated the need to compare low temperature transport in $BaSnO_3$, since both materials share the same cubic crystal structure. Fig. C.1 shows $\partial R_s/\partial T$ as a function of temperature, and R_s as function of T^2, for $BaSnO_3$ films grown on $PrScO_3$ and $DyScO_3$ samples. It is evident from the plots that no linear regimes were found at any temperature that support presence of T^2 scattering behavior in $BaSnO_3$. The most significant difference in the conduction mechanisms between $BaSnO_3$ and $SrTiO_3$ is the s-orbital and d-orbital nature of their conduction bands respectively, indicating that d-bands nature could be responsible for the T^2 behavior in $SrTiO_3$ and requires further investigation.

—— Bibliography ————————-

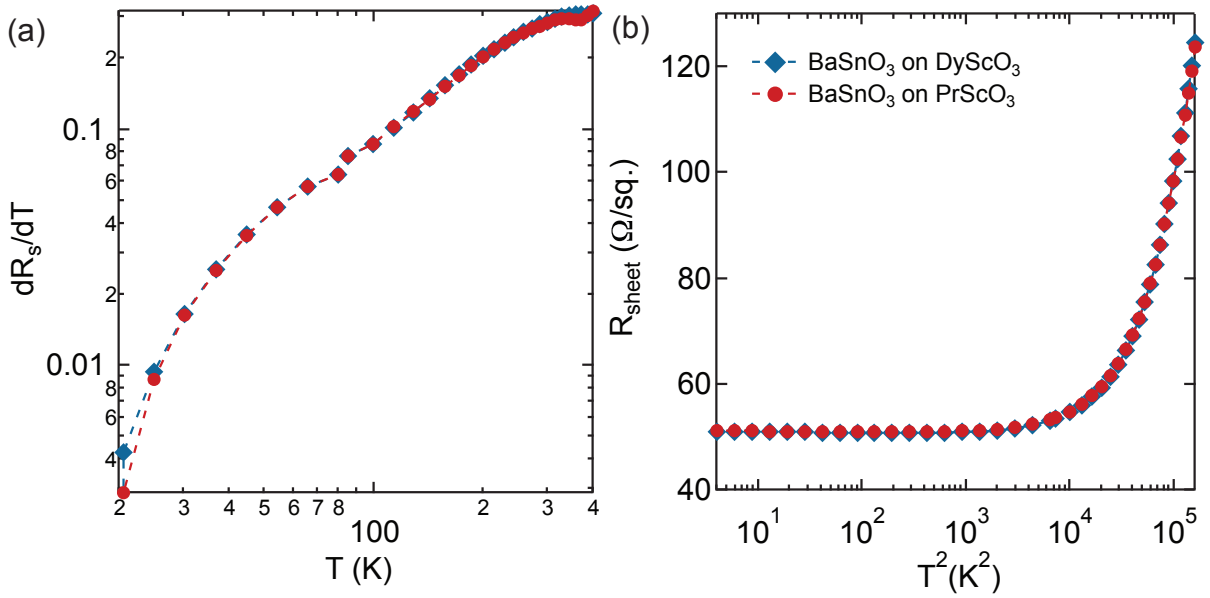

Figure C.1: (a) $\partial R_s/\partial T$ as a function of temperature, and (b) sheet resistance (R_s) as function of T^2 for high mobility $BaSnO_3$ films grown on $PrScO_3$ and $DyScO_3$ substrates.

Bibliography

[1] H. Mizoguchi, H. W. Eng, and P. M. Woodward, *Probing the Electronic Structures of Ternary Perovskite and Pyrochlore Oxides Containing Sn4+ or Sb5+*, *Inorganic Chemistry* **43** (2004), no. 5 1667–1680.

[2] D. J. Singh, D. A. Papaconstantopoulos, J. P. Julien, and F. Cyrot-Lackmann, *Electronic structure of Ba(Sn,Sb)O3 : Absence of superconductivity*, *Physical Review B* **44** (nov, 1991) 9519–9523.

[3] H. J. Kim, U. Kim, T. H. Kim, J. Kim, H. M. Kim, B. G. Jeon, W. J. Lee, H. S. Mun, K. T. Hong, J. Yu, K. Char, and K. H. Kim, *Physical properties of transparent perovskite oxides (Ba,La)SnO3 with high electrical mobility at room temperature*, *Physical Review B - Condensed Matter and Materials Physics* **86** (2012), no. 16 1–9.

[4] S. Thiel, *Tunable Quasi-Two-Dimensional Electron Gases in Oxide Heterostructures*, *Science* **313** (sep, 2006) 1942–1945.

[5] S. Raghavan, J. Y. Zhang, and S. Stemmer, *Two-dimensional electron liquid at the (111) SmTiO3/SrTiO3 interface*, *Applied Physics Letters* **106** (2015), no. 13 1–5.

[6] S. Raghavan, S. James Allen, and S. Stemmer, *Subband structure of two-dimensional electron gases in SrTiO3*, *Applied Physics Letters* **103** (2013) 212103.

[7] G. Snider, "1D Poisson Freeware."

[8] S. Raghavan, J. Y. Zhang, O. F. Shoron, and S. Stemmer, *Probing the Metal-Insulator Transition in BaTiO3 by Electrostatic Doping*, *Physical Review Letters* **117** (2016), no. 3 037602.

[9] A. P. Kajdos and S. Stemmer, *Surface reconstructions in molecular beam epitaxy of SrTiO3*, *Applied Physics Letters* **105** (2014), no. 19 1–5.

[10] P. P. Edwards, A. Porch, M. O. Jones, D. V. Morgan, and R. M. Perks, *Basic materials physics of transparent conducting oxides*, *Dalton Transactions* (2004), no. 19 2995.

[11] S. Raghavan, T. Schumann, H. Kim, J. Y. Zhang, T. A. Cain, and S. Stemmer, *High-mobility BaSnO3 grown by oxide molecular beam epitaxy*, *APL Materials* **4** (2016) 016106.

[12] T. Schumann, S. Raghavan, K. Ahadi, H. Kim, and S. Stemmer, *Structure and optical band gaps of (Ba,Sr)SnO3 films grown by molecular beam epitaxy*, *Journal of Vacuum Science & Technology A: Vacuum, Surfaces, and Films* **34** (2016), no. 5 050601.

[13] H. J. Kim, U. Kim, H. M. Kim, T. H. Kim, H. S. Mun, B. G. Jeon, K. T. Hong, W. J. Lee, C. Ju, K. H. Kimy, and K. Char, *High mobility in a stable transparent perovskite oxide*, *Applied Physics Express* **5** (2012), no. 6 4–6.

[14] K. Ganguly, P. Ambwani, P. Xu, J. S. Jeong, K. A. Mkhoyan, C. Leighton, and B. Jalan, *Structure and transport in high pressure oxygen sputter-deposited BaSnO3δ*, *APL Materials* **3** (2015), no. 6 062509.

[15] P. V. Wadekar, J. Alaria, M. O'Sullivan, N. L. O. Flack, T. D. Manning, L. J. Phillips, K. Durose, O. Lozano, S. Lucas, J. B. Claridge, and M. J. Rosseinsky, *Improved electrical mobility in highly epitaxial La:BaSnO 3 films on SmScO 3 (110) substrates*, *Applied Physics Letters* **105** (aug, 2014) 052104.

[16] A. Prakash, P. Xu, A. Faghaninia, S. Shukla, J. W. Ager, C. S. Lo, and B. Jalan, *Wide bandgap BaSnO3 films with room temperature conductivity exceeding 104 S cm1*, *Nature Communications* **8** (may, 2017) 15167.

[17] Z. Lebens-Higgins, D. O. Scanlon, H. Paik, S. Sallis, Y. Nie, M. Uchida, N. F. Quackenbush, M. J. Wahila, G. E. Sterbinsky, D. A. Arena, J. C. Woicik, D. G. Schlom, and L. F. J. Piper, *Direct Observation of Electrostatically Driven Band Gap Renormalization in a Degenerate Perovskite Transparent Conducting Oxide*, *Physical Review Letters* **116** (jan, 2016) 027602.

[18] W.-J. Lee, H. J. Kim, E. Sohn, T. H. Kim, J.-Y. Park, W. Park, H. Jeong, T. Lee, J. H. Kim, K.-Y. Choi, and K. H. Kim, *Enhanced electron mobility in epitaxial (Ba,La)SnO3 films on BaSnO3(001) substrates*, *Applied Physics Letters* **108** (2016), no. 8 082105.

[19] R. Uecker, R. Bertram, M. Brutzam, Z. Galazka, T. M. Gesing, C. Guguschev, D. Klimm, M. Klupsch, A. Kwasniewski, and D. G. Schlom, *Large-lattice-parameter perovskite single-crystal substrates*, *Journal of Crystal Growth* **457** (2017) 137–142.

[20] P. M. Woodward, *Octahedral Tilting in Perovskites. I. Geometrical Considerations*, *Acta Crystallographica Section B Structural Science* **53** (feb, 1997) 32–43.

[21] A. von Hippel, *Ferroelectricity, Domain Structure, and Phase Transitions of Barium Titanate*, *Reviews of Modern Physics* **22** (jul, 1950) 221–237.

[22] J. Volger, *Further experimental investigations on some ferromagnetic oxidic compounds of manganese with perovskite structure*, *Physica* **20** (jan, 1954) 49–66.

[23] A. Sleight, J. Gillson, and P. Bierstedt, *High-temperature superconductivity in the BaPb1-xBixO3 systems*, *Solid State Communications* **17** (jul, 1975) 27–28.

[24] J. H. Barrett, *Dielectric Constant in Perovskite Type Crystals*, *Physical Review* **86** (apr, 1952) 118–120.

[25] J. Torrance, P. Lacorre, A. Nazzal, E. Ansaldo, and C. Niedermayer, *Systematic study of insulator-metal transitions in perovskites RNiO3 (R=Pr,Nd,Sm,Eu) due to closing of charge-transfer gap*, *Physical Review B* **45** (apr, 1992) 8209–8212.

[26] Y. Tokura, Y. Taguchi, Y. Okada, Y. Fujishima, T. Arima, K. Kumagai, and Y. Iye, *Filling dependence of electronic properties on the verge of metalMott-insulator transition in Sr1-xLaxTiO3*, *Physical Review Letters* **70** (apr, 1993) 2126–2129.

[27] M. Schmidbauer, A. Kwasniewski, and J. Schwarzkopf, *High-precision absolute lattice parameter determination of SrTiO 3 , DyScO 3 and NdGaO 3 single crystals*, *Acta Crystallographica Section B Structural Science* **68** (feb, 2012) 8–14.

[28] K. van Benthem, C. Elsässer, and R. H. French, *Bulk electronic structure of SrTiO3: Experiment and theory*, *Journal of Applied Physics* **90** (dec, 2001) 6156–6164.

[29] H. P. R. Frederikse and W. R. Hosler, *Hall Mobility in SrTiO3*, *Physical Review* **161** (sep, 1967) 822–827.

[30] O. N. Tufte and P. W. Chapman, *Electron Mobility in Semiconducting Strontium Titanate*, *Physical Review* **155** (mar, 1967) 796–802.

[31] H. Yamada and G. Miller, *Point defects in reduced strontium titanate*, *Journal of Solid State Chemistry* **6** (jan, 1973) 169–177.

[32] A. Ohtomo and H. Y. Hwang, *A high-mobility electron gas at the LaAlO3/SrTiO3 heterointerface*, *Nature* **427** (jan, 2004) 423–426.

[33] P. Moetakef, T. A. Cain, D. G. Ouellette, J. Y. Zhang, D. O. Klenov, A. Janotti, C. G. Van De Walle, S. Rajan, S. J. Allen, and S. Stemmer, *Electrostatic carrier doping of GdTiO3/SrTiO3 interfaces*, *Applied Physics Letters* **99** (2011), no. 23 1–4.

[34] L. Bjaalie, B. Himmetoglu, L. Weston, A. Janotti, and C. G. Van De Walle, *Oxide interfaces for novel electronic applications*, *New Journal of Physics* **16** (2014).

[35] R. Comès, M. Lambert, and A. Guinier, *Desordre lineaire dans les cristaux (cas du silicium, du quartz, et des perovskites ferroelectriques)*, *Acta Crystallographica Section A* **26** (1970), no. 2 244–254.

[36] B. Ravel, E. a. Stern, R. I. Vedrinskii, and V. Kraizman, *Local structure and the phase transitions of BaTiO 3*, *Ferroelectrics* **206** (1998), no. 1 407–430.

[37] H. R. Liu, J. H. Yang, H. J. Xiang, X. G. Gong, and S. H. Wei, *Origin of the superior conductivity of perovskite Ba(Sr)SnO3*, *Applied Physics Letters* **102** (2013), no. 11.

[38] B. G. Kim, J. Y. Jo, and S. W. Cheong, *Hybrid functional calculation of electronic and phonon structure of BaSnO 3*, *Journal of Solid State Chemistry* **197** (2013) 134–138.

[39] S. Dabaghmanesh, R. Saniz, M. N. Amini, D. Lamoen, and B. Partoens, *Perovskite transparent conducting oxides: an ab-initio study*, *Journal of Physics: Condensed Matter* **25** (2013), no. 41 415503.

[40] X. Luo, Y. S. Oh, A. Sirenko, P. Gao, T. A. Tyson, K. Char, and S. W. Cheong, *High carrier mobility in transparent Ba 1-xLa xSnO 3 crystals with a wide band gap*, *Applied Physics Letters* **100** (2012), no. 17.

[41] H. M. Ng, D. Doppalapudi, T. D. Moustakas, N. G. Weimann, and L. F. Eastman, *The role of dislocation scattering in n -type GaN films*, *Applied Physics Letters* **73** (aug, 1998) 821–823.

[42] H. Mun, U. Kim, H. Min Kim, C. Park, T. Hoon Kim, H. Joon Kim, K. Hoon Kim, and K. Char, *Large effects of dislocations on high mobility of epitaxial perovskite Ba0.96La0.04SnO3 films*, *Applied Physics Letters* **102** (2013), no. 25 1–4.

[43] H. M. Ng, D. Doppalapudi, T. D. Moustakas, N. G. Weimann, and L. F. Eastman, *The role of dislocation scattering in n-type GaN films*, *Applied Physics Letters* **73** (1998), no. 6 821–823.

[44] H. Wang, X. Jiao, Q. Liu, X. Xuan, F. Chen, and W. Wu, *Transparent and conductive oxide films of the perovskite La x Sr 1 x SnO 3 (x 0.15): epitaxial growth and application for transparent heterostructures*, *Journal of Physics D: Applied Physics* **43** (2010), no. 3 035403.

[45] D. O. Scanlon, *Defect engineering of BaSnO3 for high-performance transparent conducting oxide applications*, *Physical Review B - Condensed Matter and Materials Physics* **87** (2013), no. 16 1–5.

[46] L. Pfeiffer and K. West, *The role of MBE in recent quantum Hall effect physics discoveries*, *Physica E: Low-dimensional Systems and Nanostructures* **20** (dec, 2003) 57–64.

[47] T. a. Cain, A. P. Kajdos, and S. Stemmer, *La-doped SrTiO3 films with large cryogenic thermoelectric power factors La-doped SrTiO 3 films with large cryogenic thermoelectric power factors*, .

[48] D. G. Schlom, *Perspective: Oxide molecular-beam epitaxy rocks!*, *APL Materials* **3** (jun, 2015) 062403.

[49] J. Tsao, *Materials Fundamentals of Molecular Beam Epitaxy*. Academic Press, 1993.

[50] C. D. Theis, J. Yeh, D. G. Schlom, M. E. Hawley, and G. W. & Brown, *Adsorption-controlled growth of PbTiO3 by reactive molecular beam epitaxy*, *Thin Film Solids* **325** (1998) 107–114.

[51] D. Schlom, J. Haeni, J. Lettieri, C. Theis, W. Tian, J. Jiang, and X. Pan, *Oxide nano-engineering using MBE*, *Materials Science and Engineering: B* **87** (dec, 2001) 282–291.

[52] E. S. Hellman, *Adsorption controlled molecular beam epitaxy of rubidium barium bismuth oxide*, *Journal of Vacuum Science & Technology B: Microelectronics and Nanometer Structures* **8** (mar, 1990) 332.

[53] C. M. Brooks, L. F. Kourkoutis, T. Heeg, J. Schubert, D. A. Muller, and D. G. Schlom, *Growth of homoepitaxial SrTiO3 thin films by molecular-beam epitaxy*, *Applied Physics Letters* **94** (apr, 2009) 162905.

[54] B. Jalan, P. Moetakef, and S. Stemmer, *Molecular beam epitaxy of SrTiO3 with a growth window*, *Applied Physics Letters* **95** (jul, 2009) 032906.

[55] P. Moetakef, J. Y. Zhang, S. Raghavan, A. P. Kajdos, and S. Stemmer, *Growth window and effect of substrate symmetry in hybrid molecular beam epitaxy of a Mott insulating rare earth titanate*, *Journal of Vacuum Science & Technology A: Vacuum, Surfaces, and Films* **31** (2013), no. 2013 041503.

[56] A. P. Kajdos, D. G. Ouellette, T. A. Cain, and S. Stemmer, *Two-dimensional electron gas in a modulation-doped SrTiO 3 /Sr(Ti, Zr)O 3 heterostructure*, *Applied Physics Letters* **103** (aug, 2013) 082120.

[57] M. Brahlek, L. Zhang, C. Eaton, H.-T. Zhang, and R. Engel-Herbert, *Accessing a growth window for SrVO 3 thin films*, *Applied Physics Letters* **107** (oct, 2015) 143108.

[58] K. Krishnaswamy, B. Himmetoglu, Y. Kang, A. Janotti, and C. G. Van de Walle, *First-principles analysis of electron transport in BaSnO3*, *Physical Review B* **95** (may, 2017) 205202.

[59] H. Ibach and H. Luth, *Solid State Physics*. Springer, 2010.

[60] L. J. Van der Pauw, *A method of measuring specific resistivity and Hall effect of discs of arbitrary shape*, *Philips Research Reports* **13** (1958) 1–9.

[61] W. Zhong, R. D. King-Smith, and D. Vanderbilt, *Giant LO-TO splittings in perovskite ferroelectrics*, *Physical Review Letters* **72** (1994), no. 22 3618–3621.

[62] *Polarization induced electron populations in III-V nitride semiconductors Transport, growth, and device applications*. PhD thesis, University of California, 2003.

[63] C. Hamaguchi, *Basic Semiconductor Physics*. Springer, 2010.

[64] F. E. Low and D. Pines, *Mobility of Slow Electrons in Polar Crystals*, *Physical Review* **98** (apr, 1955) 414–418.

[65] A. Verma, A. P. Kajdos, T. A. Cain, S. Stemmer, and D. Jena, *Intrinsic mobility limiting mechanisms in lanthanum-doped strontium titanate*, *Physical Review Letters* **112** (2014), no. 21 1–5.

[66] E. Mikheev, B. Himmetoglu, A. P. Kajdos, P. Moetakef, T. A. Cain, C. G. Van De Walle, and S. Stemmer, *Limitations to the room temperature mobility of two- and three-dimensional electron liquids in SrTiO3*, *Applied Physics Letters* **106** (2015), no. 6 19–23.

[67] W. G. Baber, *The Contribution to the Electrical Resistance of Metals from Collisions between Electrons*, *Proceedings of the Royal Society A: Mathematical, Physical and Engineering Sciences* **158** (jan, 1937) 383–396.

[68] W. E. Lawrence and J. W. Wilkins, *Electron-Electron Scattering in the Transport Coefficients of Simple Metals*, *Physical Review B* **7** (mar, 1973) 2317–2332.

[69] N. W. Ashcroft and N. D. Mermin, *Solid State Physics*. Saunders College Publishing, 1976.

[70] D. van der Marel, J. L. M. van Mechelen, and I. I. Mazin, *Common Fermi-liquid origin of T2 resistivity and superconductivity in n-type SrTiO3*, *Physical Review B* **84** (nov, 2011) 205111.

[71] E. Mikheev, S. Raghavan, J. Y. Zhang, P. B. Marshall, A. P. Kajdos, L. Balents, and S. Stemmer, *Carrier density independent scattering rate in SrTiO3-based electron liquids*, *Scientific Reports* **6** (2016), no. October 2015 20865.

[72] E. Mikheev, A. J. Hauser, B. Himmetoglu, N. E. Moreno, A. Janotti, C. G. Van de Walle, and S. Stemmer, *Tuning bad metal and non-Fermi liquid behavior in a Mott material: Rare-earth nickelate thin films*, *Science Advances* **1** (nov, 2015) e1500797–e1500797.

[73] Y. Ando, Y. Kurita, S. Komiya, S. Ono, and K. Segawa, *Evolution of the Hall Coefficient and the Peculiar Electronic Structure of the Cuprate Superconductors*, *Physical Review Letters* **92** (may, 2004) 197001.

[74] S. N. Klimin, J. Tempere, D. Van Der Marel, and J. T. Devreese, *Microscopic mechanisms for the Fermi-liquid behavior of Nb-doped strontium titanate*, *Physical Review B - Condensed Matter and Materials Physics* **86** (2012), no. 4 1–22.

[75] M. Swift and C. G. Van de Walle, *Conditions for T^2 resistivity from electron-electron scattering*, arXiv:1701.0474.

[76] D. Chattopadhyay and H. J. Queisser, *Electron scattering by ionized impurities in semiconductors*, *Reviews of Modern Physics* **53** (1981), no. 4 745–768.

[77] A. Ohtomo and H. Y. Hwang, *Surface depletion in doped SrTiO3 thin films*, *Applied Physics Letters* **84** (2004), no. 10 1716.

[78] P. Moetakef, C. A. Jackson, J. Hwang, L. Balents, S. J. Allen, and S. Stemmer, *Toward an artificial Mott insulator: Correlations in confined high-density electron liquids in SrTiO 3*, *Physical Review B - Condensed Matter and Materials Physics* **86** (2012), no. 20 1–4.

[79] P. Moetakef, J. R. Williams, D. G. Ouellette, A. P. Kajdos, D. Goldhaber-Gordon, S. J. Allen, and S. Stemmer, *Carrier-controlled ferromagnetism in SrTiO3*, *Physical Review X* **2** (2012), no. 2 2–6.

[80] N. E. Hussey , K. Takenaka, and H. Takagi, *Universality of the Mott-Ioffe-Regel limit in metals*, *Philosophical Magazine* **84** (sep, 2004) 2847–2864.

[81] K. Krishnaswamy, C. E. Dreyer, A. Janotti, and C. G. Van de Walle, *First-principles study of surface charging in LaAlO3/SrTiO3 heterostructures*, *Physical Review B* **92** (aug, 2015) 085420.

[82] A. Rüegg and G. A. Fiete, *Topological insulators from complex orbital order in transition-metal oxides heterostructures*, *Physical Review B - Condensed Matter and Materials Physics* **84** (2011), no. 20 1–5.

[83] A. Rüegg, C. Mitra, A. A. Demkov, and G. A. Fiete, *Lattice distortion effects on topological phases in (LaNiO3)2/(LaAlO3)N heterostructures grown along the [111] direction*, *Physical Review B* **88** (2013), no. 11 115146.

[84] D. Xiao, W. Zhu, Y. Ran, N. Nagaosa, and S. Okamoto, *Interface engineering of quantum Hall effects in digital transition metal oxide heterostructures.*, *Nature communications* **2** (2011) 596.

[85] D. Doennig, W. E. Pickett, and R. Pentcheva, *Massive symmetry breaking in LaAlO3/SrTiO3(111) quantum wells: A three-orbital strongly correlated generalization of graphene*, *Physical Review Letters* **111** (2013), no. 12 1–5.

[86] K. Y. Yang, W. Zhu, D. Xiao, S. Okamoto, Z. Wang, and Y. Ran, *Possible interaction-driven topological phases in (111) bilayers of LaNiO3*, *Physical Review B - Condensed Matter and Materials Physics* **84** (2011), no. 20 2–5.

[87] G. Khalsa and A. H. MacDonald, *Theory of the SrTiO3 surface state two-dimensional electron gas*, *Physical Review B* **86** (2012), no. 12 125121.

[88] S. Y. Park and A. J. Millis, *Charge density distribution and optical response of the LaAlO 3/SrTiO 3 interface*, *Physical Review B* **87** (2013), no. 20 205145.

[89] S. Stemmer and S. James Allen, *Two-Dimensional Electron Gases at Complex Oxide Interfaces*, *Annual Review of Materials Research* **44** (jul, 2014) 151–171.

[90] T. C. Rödel, C. Bareille, F. Fortuna, C. Baumier, F. Bertran, P. Le Fèvre, M. Gabay, O. Hijano Cubelos, M. J. Rozenberg, T. Maroutian, P. Lecoeur, and A. F. Santander-Syro, *Orientational Tuning of the Fermi Sea of Confined Electrons at the SrTiO3 (110) and (111) Surfaces*, *Physical Review Applied* **1** (2014), no. 5 1–5.

[91] S. McKeown Walker, A. De La Torre, F. Y. Bruno, A. Tamai, T. K. Kim, M. Hoesch, M. Shi, M. S. Bahramy, P. D. C. King, and F. Baumberger, *Control of a Two-Dimensional Electron Gas on SrTiO3 (111) by Atomic Oxygen*, *Physical Review Letters* **113** (2014), no. 17 1–5.

[92] A. Ohtomo, D. A. Muller, J. L. Grazul, and H. Y. Hwang, *Epitaxial growth and electronic structure of LaTiOx films*, *Applied Physics Letters* **80** (may, 2002) 3922–3924.

[93] A. Baratoff and G. Binnig, *Mechanism of superconductivity in SrTiO3*, *Physica B+C* **108** (aug, 1981) 1335–1336.

[94] T. M. Rice and W. F. Brinkman, *Effects of impurities on the metal-insulator transition*, *Physical Review B* **5** (1972), no. 11 4350–4357.

[95] K. Ahadi, O. F. Shoron, P. B. Marshall, E. Mikheev, and S. Stemmer, *Electric field effect near the metal-insulator transition of a two-dimensional electron system in SrTiO 3*, *Applied Physics Letters* **110** (feb, 2017) 062104.

[96] P. Delugas, A. Filippetti, V. Fiorentini, D. I. Bilc, D. Fontaine, and P. Ghosez, *Spontaneous 2-Dimensional Carrier Confinement at the n-type SrTiO3/LaAlO3 Interface*, *Physical Review Letters* **106** (apr, 2011) 166807.

[97] W.-J. Son, E. Cho, B. Lee, J. Lee, and S. Han, *Density and spatial distribution of charge carriers in the intrinsic n-type LaAlO3/SrTiO3 interface*, *Physical Review B* **79** (jun, 2009) 245411.

[98] M. Stengel, *First-Principles Modeling of Electrostatically Doped Perovskite Systems*, *Physical Review Letters* **106** (mar, 2011) 136803.

[99] Z. Zhong, A. Tóth, and K. Held, *Theory of spin-orbit coupling at LaAlO3/SrTiO3 interfaces and SrTiO3 surfaces*, *Physical Review B - Condensed Matter and Materials Physics* **87** (2013), no. 16 1–5.

[100] Y. Kim, R. M. Lutchyn, and C. Nayak, *Origin and transport signatures of spin-orbit interactions in one- and two-dimensional SrTiO3 -based heterostructures*, *Physical Review B* **87** (jun, 2013) 245121.

[101] Z. S. Popović, S. Satpathy, and R. M. Martin, *Origin of the Two-Dimensional Electron Gas Carrier Density at the LaAlO3/SrTiO3 Interface*, *Physical Review Letters* **101** (dec, 2008) 256801.

[102] Z. Zhong, Q. Zhang, and K. Held, *Quantum confinement in perovskite oxide heterostructures: Tight binding instead of a nearly free electron picture*, *Physical Review B* **88** (sep, 2013) 125401.

[103] F. Lechermann, L. Boehnke, and D. Grieger, *Formation of orbital-selective electron states in LaTiO3/SrTiO3 superlattices*, *Physical Review B* **87** (jun, 2013) 241101.

[104] P. Delugas, A. Filippetti, A. Gadaleta, I. Pallecchi, D. Marré, and V. Fiorentini, *Large band offset as driving force of two-dimensional electron confinement: The case of SrTiO3/SrZrO3 interface*, *Physical Review B* **88** (sep, 2013) 115304.

[105] A. Janotti, L. Bjaalie, L. Gordon, and C. G. Van de Walle, *Controlling the density of the two-dimensional electron gas at the SrTiO3 /LaAlO3 interface*, *Physical Review B* **86** (dec, 2012) 241108.

[106] R. Chen, S. Lee, and L. Balents, *Dimer Mott insulator in an oxide heterostructure*, *Physical Review B* **87** (apr, 2013) 161119.

[107] G. Chen and L. Balents, *Ferromagnetism in Itinerant Two-Dimensional t2g Systems*, *Physical Review Letters* **110** (may, 2013) 206401.

[108] A. Joshua, J. Ruhman, S. Pecker, E. Altman, and S. Ilani, *Gate-tunable polarized phase of two-dimensional electrons at the LaAlO3/SrTiO3 interface*, *Proceedings of the National Academy of Sciences* **110** (jun, 2013) 9633–9638.

[109] S. Banerjee, O. Erten, and M. Randeria, *Ferromagnetic exchange, spinorbit coupling and spiral magnetism at the LaAlO3/SrTiO3 interface*, *Nature Physics* **9** (aug, 2013) 626–630.

[110] A. Fête, S. Gariglio, A. D. Caviglia, J.-M. Triscone, and M. Gabay, *Rashba induced magnetoconductance oscillations in the LaAlO3/SrTiO3 heterostructure*, *Physical Review B* **86** (nov, 2012) 201105.

[111] S. M. Walker, F. Y. Bruno, Z. Wang, A. de la Torre, S. Riccó, A. Tamai, T. K. Kim, M. Hoesch, M. Shi, M. S. Bahramy, P. D. C. King, and F. Baumberger, *Carrier-Density Control of the SrTiO 3 (001) Surface 2D Electron Gas studied by ARPES*, *Advanced Materials* **27** (jul, 2015) 3894–3899.

[112] A. D. Caviglia, S. Gariglio, C. Cancellieri, B. Sacépé, A. Fête, N. Reyren, M. Gabay, A. F. Morpurgo, and J.-M. Triscone, *Two-Dimensional Quantum Oscillations of the Conductance at LaAlO3/SrTiO3 Interfaces*, *Physical Review Letters* **105** (2010), no. 23 236802.

[113] P. Moetakef, D. G. Ouellette, J. R. Williams, S. James Allen, L. Balents, D. Goldhaber-Gordon, and S. Stemmer, *Quantum oscillations from a two-dimensional electron gas at a Mott/band insulator interface*, *Applied Physics Letters* **101** (oct, 2012) 151604.

[114] B. Jalan, S. Stemmer, S. Mack, and S. J. Allen, *Two-dimensional electron gas in delta doped SrTiO3*, *Physical Review B* **82** (aug, 2010) 081103.

[115] Y. Kozuka, M. Kim, C. Bell, B. G. Kim, Y. Hikita, and H. Y. Hwang, *Two-dimensional normal-state quantum oscillations in a superconducting heterostructure*, *Nature* **462** (nov, 2009) 487–490.

[116] J. Smoliner, W. Demmerle, G. Berthold, E. Gornik, G. Weimann, and W. Schlapp, *Momentum conservation in tunneling processes between barrier-separated 2D-electron-gas systems*, *Physical Review Letters* **63** (nov, 1989) 2116–2119.

[117] A. Y. Lew, S. L. Zuo, E. T. Yu, and R. H. Miles, *Anisotropy and growth-sequence dependence of atomic-scale interface structure in InAs/Ga1-xInxSb superlattices*, *Applied Physics Letters* **70** (jan, 1997) 75–77.

[118] B. Mazumder, M. H. Wong, C. A. Hurni, J. Y. Zhang, U. K. Mishra, and J. S. Speck, *Asymmetric interfacial abruptness in N-polar and Ga-polar GaN/AlN/GaN heterostructures*, *Applied Physics Letters* **101** (aug, 2012) 091601.

[119] J. Y. Zhang, J. Hwang, S. Raghavan, and S. Stemmer, *Symmetry lowering in extreme-electron-density perovskite quantum wells*, *Physical Review Letters* **110** (2013), no. 25 1–5.

[120] J. D. Burton, J. P. Velev, and E. Y. Tsymbal, *Oxide tunnel junctions supporting a two-dimensional electron gas*, *Physical Review B - Condensed Matter and Materials Physics* **80** (2009), no. 11 1–8.

[121] K. Page, T. Kolodiazhnyi, T. Proffen, A. K. Cheetham, and R. Seshadri, *Local structural origins of the distinct electronic properties of Nb-substituted SrTiO3 and BaTiO3*, *Physical Review Letters* **101** (2008), no. 20 1–4.

[122] T. Kolodiazhnyi, *Insulator-metal transition and anomalous sign reversal of the dominant charge carriers in perovskite BaTiO3-delta*, *Physical Review B - Condensed Matter and Materials Physics* **78** (2008), no. 4 6–10.

[123] T. Kolodiazhnyi, M. Tachibana, H. Kawaji, J. Hwang, and E. Takayama-Muromachi, *Persistence of ferroelectricity in BaTiO3 through the insulator-metal transition*, *Physical Review Letters* **104** (2010), no. 14 1–4.

[124] J. A. Bock, S. Lee, S. Trolier-McKinstry, and C. A. Randall, *Metallic-like to nonmetallic transitions in a variety of heavily oxygen deficient ferroelectrics*, *Applied Physics Letters* **107** (2015), no. 9 1–5.

[125] A. Spinelli, M. A. Torija, C. Liu, C. Jan, and C. Leighton, *Electronic transport in doped SrTiO3 : Conduction mechanisms and potential applications*, *Physical Review B* **81** (2010), no. 15 155110.

[126] P. W. Anderson and E. I. Blount, *Symmetry Considerations on Martensitic Transformations: "Ferroelectric" Metals?*, *Physical Review Letters* **14** (feb, 1965) 217–219.

[127] E. Steigmeier and G. Harbeke, *Soft phonon mode and ferroelectricity in GeTe*, *Solid State Communications* **8** (aug, 1970) 1275–1279.

[128] Y. Wang, X. Liu, J. D. Burton, S. S. Jaswal, and E. Y. Tsymbal, *Ferroelectric Instability Under Screened Coulomb Interactions*, *Physical Review Letters* **109** (dec, 2012) 247601.

[129] Y. Shi, Y. Guo, X. Wang, A. J. Princep, D. Khalyavin, P. Manuel, Y. Michiue, A. Sato, K. Tsuda, S. Yu, M. Arai, Y. Shirako, M. Akaogi, N. Wang, K. Yamaura, and A. T. Boothroyd, *A ferroelectric-like structural transition in a metal*, *Nature Materials* **12** (sep, 2013) 1024–1027.

[130] D. Puggioni and J. M. Rondinelli, *Designing a robustly metallic noncenstrosymmetric ruthenate oxide with large thermopower anisotropy*, *Nature Communications* **5** (mar, 2014).

[131] P. Ghosez, X. Gonze, and J.-P. Michenaud, *Coulomb interaction and ferroelectric instability of BaTiO 3*, *Europhysics Letters (EPL)* **33** (mar, 1996) 713–718.

[132] P. Ghosez, X. Gonze, and J.-P. Michenaud, *Lattice dynamics and ferroelectric instability of barium titanate*, *Ferroelectrics* **194** (apr, 1997) 39–54.

[133] A. Mooradian and G. B. Wright, *Observation of the Interaction of Plasmons with Longitudinal Optical Phonons in GaAs*, *Physical Review Letters* **16** (may, 1966) 999–1001.

[134] Y. Iwazaki, T. Suzuki, Y. Mizuno, and S. Tsuneyuki, *Doping-induced phase transitions in ferroelectric BaTiO3 from first-principles calculations*, *Physical Review B - Condensed Matter and Materials Physics* **86** (2012), no. 21 1–6.

[135] I. K. Jeong, S. Lee, S. Y. Jeong, C. J. Won, N. Hur, and A. Llobet, *Structural evolution across the insulator-metal transition in oxygen-deficient BaTiO3-delta studied using neutron total scattering and Rietveld analysis*, *Physical Review B - Condensed Matter and Materials Physics* **84** (2011), no. 6 2–6.

[136] J. S. Kim, S. S. A. Seo, M. F. Chisholm, R. K. Kremer, H. U. Habermeier, B. Keimer, and H. N. Lee, *Nonlinear Hall effect and multichannel conduction in LaTiO 3/SrTiO3 superlattices*, *Physical Review B - Condensed Matter and Materials Physics* **82** (2010), no. 20 2–5.

[137] F. Lechermann and M. Obermeyer, *Towards Mott design by delta-doping of strongly correlated titanates*, *New Journal of Physics* **17** (2015), no. 4 43026.

[138] R. Pentcheva and W. E. Pickett, *Correlation-Driven Charge Order at the Interface between a Mott and a Band Insulator*, *Physical Review Letters* **99** (jul, 2007) 016802.

[139] L. Bjaalie, A. Janotti, B. Himmetoglu, and C. G. Van de Walle, *Turning SrTiO3 into a Mott insulator*, *Physical Review B* **90** (nov, 2014) 195117.

[140] M. Cardona, *Optical Properties and Band Structure of SrTiO3 and BaTiO3*, *Physical Review* **140** (oct, 1965) A651–A655.

[141] L. Bjaalie, A. Verma, B. Himmetoglu, A. Janotti, S. Raghavan, V. Protasenko, E. H. Steenbergen, D. Jena, S. Stemmer, and C. G. Van De Walle, *Determination of the Mott-Hubbard gap in GdTiO3*, *Physical Review B - Condensed Matter and Materials Physics* **92** (2015), no. 8 2–6.

[142] P. Moetakef, J. Y. Zhang, A. Kozhanov, B. Jalan, R. Seshadri, S. J. Allen, and S. Stemmer, *Transport in ferromagnetic GdTiO3 / SrTiO3 heterostructures*, *Applied Physics Letters* **98** (2011), no. 11 2–4.

[143] K. J. Choi, *Enhancement of Ferroelectricity in Strained BaTiO3 Thin Films*, *Science* **306** (nov, 2004) 1005–1009.

[144] C. A. Jackson, J. Y. Zhang, C. R. Freeze, and S. Stemmer, *Quantum critical behaviour in confined SrTiO3 quantum wells embedded in antiferromagnetic SmTiO3*, *Nature Communications* **5** (jul, 2014).

[145] D. Emin, *On the existence of free and self-trapped carriers in insulators: an abrupt temperature-dependent conductivity transition*, *Advances in Physics* **22** (jan, 1973) 57–116.

[146] Y. S. Kim, D. H. Kim, J. D. Kim, Y. J. Chang, T. W. Noh, J. H. Kong, K. Char, Y. D. Park, S. D. Bu, J.-G. Yoon, and J.-S. Chung, *Critical thickness of ultrathin ferroelectric BaTiO3 films*, *Applied Physics Letters* **86** (mar, 2005) 102907.

[147] D. D. Fong, *Ferroelectricity in Ultrathin Perovskite Films*, *Science* **304** (jun, 2004) 1650–1653.

[148] D. Emin, *Polarons*. Cambridge University Press, Cambridge, England, 2013.

[149] N. F. Mott, *Conduction in non-crystalline systems IX. the minimum metallic conductivity*, *Philosophical Magazine* **26** (oct, 1972) 1015–1026.

[150] T. Kolodiazhnyi, A. Petric, M. Niewczas, C. Bridges, A. Safa-Sefat, and J. E. Greedan, *Thermoelectric power, Hall effect, and mobility of n-type BaTiO3*, *Physical Review B* **68** (2003), no. 8 085205.

[151] S. Fratini and S. Ciuchi, *Dynamical Mean-Field Theory of Transport of Small Polarons*, *Physical Review Letters* **91** (dec, 2003) 256403.

[152] S. Salahuddin and S. Datta, *Use of Negative Capacitance to Provide Voltage Amplification for Low Power Nanoscale Devices*, *Nano Letters* **8** (feb, 2008) 405–410.

[153] J. Son, S. Rajan, S. Stemmer, and S. James Allen, *A heterojunction modulation-doped Mott transistor*, *Journal of Applied Physics* **110** (oct, 2011) 084503.

[154] S. Ismail-Beigi, F. J. Walker, S.-W. Cheong, K. M. Rabe, and C. H. Ahn, *Alkaline earth stannates: The next silicon?*, *APL Materials* **3** (2015), no. 6 062510.

[155] S. Sallis, D. O. Scanlon, S. C. Chae, N. F. Quackenbush, D. A. Fischer, J. C. Woicik, J.-H. Guo, S. W. Cheong, and L. F. J. Piper, *La-doped BaSnO 3 Degenerate perovskite transparent conducting oxide: Evidence from synchrotron x-ray spectroscopy*, *Applied Physics Letters* **103** (jul, 2013) 042105.

[156] P. Vanysek, *CRC Handbook of Chemistry and Physics*. 2015.

[157] M. E. White, M. Y. Tsai, F. Wu, and J. S. Speck, *Plasma-assisted molecular beam epitaxy and characterization of SnO2(101) on r-plane sapphire*, *Journal of Vacuum Science & Technology A: Vacuum, Surfaces, and Films* **26** (2008), no. 5 1300.

[158] M. Y. Tsai, M. E. White, and J. S. Speck, *Investigation of (110) SnO[sub 2] growth mechanisms on TiO[sub 2] substrates by plasma-assisted molecular beam epitaxy*, *Journal of Applied Physics* **106** (2009), no. 2 024911.

[159] R. Muller, F. Hernandez-Ramirez, H. Shen, H. Du, W. Mader, and S. Mathur, *Influence of precursor chemistry on morphology and composition of CVD-grown SnO 2 nanowires*, *Chemistry of Materials* **24** (2012), no. 21 4028–4035.

[160] D. J. Houlton, A. C. Jones, P. W. Haycock, E. W. Williams, J. Bull, and G. W. Critchlow, *The deposition of platinum-containing tin oxide thin films by metal-organic CVD*, *Chemical Vapor Deposition* **1** (1995), no. 1 26–28.

[161] M. J. Hampden-Smith, T. A. Wark, A. L. Rheingold, and J. C. Huffman, *Solid state and solution structural investigation of homoleptic tin(IV) alkoxide compounds. Part I. Sn(0-t-Bu)4 and [Sn(O-i-Pr)4. H0-i-Pr]2*, *Can. J. Chem.* **69** (1990), no. 4.

[162] O. Bierwagen, A. Proessdorf, M. Niehle, F. Grosse, A. Trampert, and M. Klingsporn, *Oxygen-deficient oxide growth by subliming the oxide source material: The cause of silicide formation in rare earth oxides on silicon*, *Crystal Growth and Design* **13** (2013), no. 8 3645–3650.

[163] T. Watahiki, W. Braun, and H. Riechert, *Structure dependence of epitaxial Pr2O3Si(001) on oxygen pressure during growth*, *Journal of Vacuum Science & Technology B: Microelectronics and Nanometer Structures* **27** (2009), no. 1 262.

[164] K. Sasaki, A. Kuramata, T. Masui, E. G. Víllora, K. Shimamura, and S. Yamakoshi, *Device-Quality beta-Ga2O3 Epitaxial Films Fabricated by Ozone Molecular Beam Epitaxy*, *Applied Physics Express* **5** (feb, 2012) 035502.

[165] Z. Galazka, R. Uecker, D. Klimm, K. Irmscher, M. Pietsch, R. Schewski, M. Albrecht, A. Kwasniewski, S. Ganschow, D. Schulz, C. Guguschev, R. Bertram, M. Bickermann, and R. Fornari, *Growth, characterization, and properties of bulk SnO 2 single crystals*, *physica status solidi (a)* **211** (jan, 2014) 66–73.

[166] P. Vogt and O. Bierwagen, *The competing oxide and sub-oxide formation in metal-oxide molecular beam epitaxy*, *Applied Physics Letters* **106** (feb, 2015) 081910.

[167] R. H. Lamoreaux, D. L. Hildenbrand, and L. Brewer, *HighTemperature Vaporization Behavior of Oxides II. Oxides of Be, Mg, Ca, Sr, Ba, B, Al, Ga, In, Tl, Si, Ge, Sn, Pb, Zn, Cd, and Hg*, *Journal of Physical and Chemical Reference Data* **16** (jul, 1987) 419–443.

[168] A. Vegas, M. Vallet-Regí, J. M. González-Calbet, and M. A. Alario-Franco, *The A SnO 3 (A =Ca,Sr) perovskites*, *Acta Crystallographica Section B Structural Science* **42** (apr, 1986) 167–172.

[169] B. Bauer and R. Richter, *Optical Characterization of Epitaxial Semiconductor Layers*, Springer, Berlin, 1996.

[170] I. Shein, V. Kozhevnikov, and A. Ivanovskii, *First-principles calculations of the elastic and electronic properties of the cubic perovskites SrMO3 (M=Ti, V, Zr and Nb) in comparison with SrSnO3*, *Solid State Sciences* **10** (feb, 2008) 217–225.

[171] B. Ghebouli, M. Ghebouli, T. Chihi, M. Fatmi, S. Boucetta, and M. Reffas, *First-principles study of structural, elastic, electronic and optical properties of SrMO3 (M=Ti and Sn)*, *Solid State Communications* **149** (dec, 2009) 2244–2249.

[172] A. Prakash, P. Xu, X. Wu, G. Haugstad, X. Wang, and B. Jalan, *Adsorption-controlled growth and the influence of stoichiometry on electronic transport in hybrid molecular beam epitaxy-grown BaSnO3 films*, *J. Mater. Chem. C* (2017).

[173] H. Fujiwara, J. Koh, P. I. Rovira, and R. W. Collins, *Assessment of effective-medium theories in the analysis of nucleation and microscopic surface roughness evolution for semiconductor thin films*, *Physical Review B* **61** (apr, 2000) 10832–10844.

[174] H. Fujiwara, *Spectroscopic Ellipsometry*. John Wiley & Sons, Chichester, 2007.

[175] S. A. Chambers, T. C. Kaspar, A. Prakash, G. Haugstad, and B. Jalan, *Band alignment at epitaxial BaSnO 3 /SrTiO 3 (001) and BaSnO 3 /LaAlO 3 (001) heterojunctions*, *Applied Physics Letters* **108** (apr, 2016) 152104.

[176] A. Ghosh, C. M. Nelson, L. S. Abdallah, and S. Zollner, *Optical constants and band structure of trigonal NiO*, *Journal of Vacuum Science & Technology A: Vacuum, Surfaces, and Films* **33** (nov, 2015) 061203.

[177] T. N. Stanislavchuk, A. A. Sirenko, A. P. Litvinchuk, X. Luo, and S.-W. Cheong, *Electronic band structure and optical phonons of BaSnO 3 and Ba 0.97 La 0.03 SnO 3 single crystals: Theory and experiment*, *Journal of Applied Physics* **112** (aug, 2012) 044108.

[178] Q. Liu, B. Li, J. Liu, H. Li, Z. Liu, K. Dai, G. Zhu, P. Zhang, F. Chen, and J. Dai, *Structure and band gap tuning of transparent (Ba 1x Sr x)SnO 3 thin films epitaxially grown on MgO substrates*, *EPL (Europhysics Letters)* **98** (may, 2012) 47010.

[179] S. A. Chambers, T. C. Kaspar, A. Prakash, G. Haugstad, and B. Jalan, *Band alignment at epitaxial BaSnO 3 /SrTiO 3 (001) and BaSnO 3 /LaAlO 3 (001) heterojunctions*, *Applied Physics Letters* **108** (apr, 2016) 152104.

[180] S. James Allen, S. Raghavan, T. Schumann, K.-M. Law, and S. Stemmer, *Conduction band edge effective mass of La-doped BaSnO 3*, *Applied Physics Letters* **108** (jun, 2016) 252107.

[181] Y. Li, L. Zhang, Y. Ma, and D. J. Singh, *Tuning optical properties of transparent conducting barium stannate by dimensional reduction*, *APL Materials* **3** (jan, 2015) 011102.

[182] F. Galasso, *Perovskites and High Tc Superconductors*. Gordon and Breach Science Publishers, New York, 1990.

[183] J. L. Blok, X. Wan, G. Koster, D. H. A. Blank, and G. Rijnders, *Epitaxial oxide growth on polar (111) surfaces*, *Applied Physics Letters* **99** (oct, 2011) 151917.

[184] I. Hallsteinsen, M. Nord, T. Bolstad, P.-E. Vullum, J. E. Boschker, P. Longo, R. Takahashi, R. Holmestad, M. Lippmaa, and T. Tybell, *Effect of Polar (111)-Oriented SrTiO 3 on Initial Perovskite Growth*, *Crystal Growth & Design* **16** (apr, 2016) 2357–2362.

[185] M. Y. Tsai, M. E. White, and J. S. Speck, *Plasma-assisted molecular beam epitaxy of SnO2 on TiO2*, *Journal of Crystal Growth* **310** (2008), no. 18 4256–4261.

[186] E. C. H. Kyle, S. W. Kaun, P. G. Burke, F. Wu, Y. R. Wu, and J. S. Speck, *High-electron-mobility GaN grown on free-standing GaN templates by ammonia-based molecular beam epitaxy*, *Journal of Applied Physics* **115** (2014), no. 19.

[187] R. G. Palgrave, A. Bourlange, D. J. Payne, J. S. Foord, and R. G. Egdell, *Interfacial Diffusion during Growth of SnO 2 (110) on TiO 2 (110) by Oxygen Plasma Assisted Molecular Beam Epitaxy*, *Crystal Growth & Design* **9** (apr, 2009) 1793–1797.

[188] C. Adelmann, J. Brault, E. Martinez-Guerrero, G. Mula, H. Mariette, L. Si Dang, and B. Daudin, *Molecular-Beam Epitaxy of GaN: A Phase Diagram*, *physica status solidi (a)* **188** (dec, 2001) 575–578.